The Appearance of Platelet-Polymer Composite Coatings: Microstructural Characterization, Hybrid Modeling, and Predictive Design

by

Christopher M. Seubert

A dissertation submitted in partial fulfillment
of the requirements for the degree of
Doctor of Philosophy
(Materials Science and Engineering)
in the University of Michigan
2016

Doctoral Committee:

Professor Michael D. Thouless, Co-Chair
Associate Professor Max Shtein, Co-Chair
Professor L. Jay Guo
Associate Professor Gary Meyer, University of Minnesota

To Margaret, Joshua, and Charlotte, my supportive and loving family, who always ask “How was your day?”.

ACKNOWLEDGEMENTS

Mark Nichols and Kevin Ellwood, my colleagues, supervisors, and friends, for their encouragement and support at the Ford Motor Company.

Professor Michael Thouless and Professor Max Shtein for their willingness and patience to help me improve my writing and research skills. Some may argue their work was in vain.

-S for not warning me.

Charlotte and Joshua Seubert for being the greatest kids around. There is nothing that makes a father happier than getting a great big hug every day when you get home. And last, but far from least, my wife Maggie who was able to put up with not only this endeavor, but each and every little “project” that I come up with when I think I have a free minute.

TABLE OF CONTENTS

CHAPTER

List of Tables

List of Figures

CHAPTER I

Introduction

Motivation

Global retail sales across all product categories reached $22.5 trillion in 2014 and is estimated to reach $28.3 trillion in 2018 [1]. For many of these purchases, aesthetics, in addition to function, brand, and cost, played a crucial role in the purchasing decision of the customer. Fierce competition exists for product differentiation in industries such as consumer electronics, aerospace, and automotive. Customers can even personalize and differentiate themselves with unique cosmetics, an industry that will reach $390 billion globally by 2020 [2]. All of these industries use paints and coatings to create a unique color and appearance for their product.

In the automotive market, estimated to be worth $2 trillion dollars annually, 40% of buyers make purchasing decisions based primarily on the color of the vehicle [3]. This behavior occurs because color generates an emotional response in consumers, and emotions play a large role in life decisions [4]. In fact, color can even affect a customer’s willingness to pay in auctions and negotiations [5]. All of this indicates that with all other attributes being equal, a customer, deprived of their first color choice, may purchase a different brand of vehicle. For this reason, teams of designers and engineers spend multiple years developing, testing, and manufacturing new colors for the automotive industry.

Currently, most color development takes place in the physical domain. This multi-year process, where designers adjust the color and appearance of a paint, plastic, or textile, is used to achieve a desired look for a material or product. Typically, adjustments in color are made through a trial-and-error process where pigments or platelets are added/removed and a new physical sample is generated for evaluation. It is clear that the length and cost of this process could be reduced by moving some of the color development into the digital domain.

Increasingly, computer display technology can render and display colors extremely accurately with respect to CIE color coordinates. However, digitally created and displayed colors still can differ in appearance from reflected colors in physical specimen, being largely phenomenologically derived, without adequately accounting effects of paint microstructure. To more accurately portray a physical color in a digital medium the optics and physics used in the simulations must improve, particularly in how they incorporate actual 3D microstructures, and how they account for small-scale scattering of individual pigments and platelets [6–11]. For practitioners to use digital simulations to make engineering decisions, accurate descriptions of microstructures and scattering physics must be incorporated.

Digital models and simulations that utilize accurate descriptions of microstructures and optical physics will open up new avenues of color and product design. In the near future, new manufacturing processes, such as 3D-printing [12,13] and the magnetic alignment of particles [14,15] will allow designers to create precise 3D microstructures that produce novel and unique optical effects, perhaps even some based on biomimetic structures [16,17]. A digital tool that could simulate these new microstructures would allow researchers to conduct some of their work digitally, and eliminate some of the monetary and time costs associated with physical sample preparation. This digital tool would help researchers identify systems that produce completely new and novel optical effects but, would also need to accurately simulate real, physical materials. The method could not guide this new manufacturing work if it produced inaccurate or unrealistic results.

Background

Scattering of Electromagnetic Waves and Light

Scholars and industrial engineers have great interest in the scattering of electromagnetic (EM) waves by structure at different length scales [18–27],from the scattering of waves by celestial bodies such as the earth, to radar scattering from oceanic waves or forest vegetation, to defect detection using light scattering, to metamaterials. Often, EM waves and the resulting scattering patterns are used to characterize the structure of an object or material. An example of such a technique is one of the fundamental materials science analysis methods—x-ray diffraction [28,29]. One can also manipulate the scattering behavior of a material to achieve a particular need, as is done with meta-materials [30–34]. For example, stealth aircraft attempt to absorb radar waves to prevent detection. This can be accomplished through aircraft geometry or the use of electromagnetic meta-materials.

Shi has created a coating, with near perfect absorption of optical wavelengths, which consists of a forest of carbon nanotubes [30]. Black silicon is another example of surface microstructure modification that improves visible light absorption [35]. It is possible that such microstructures could be modified to expand that perfect absorption to other wavelength regimes, such as those used by radar. A tool that could simulate such behaviors and microstructures would help direct additional research in this area.

Pigments and platelets can be added to a material to modify its scattering behavior and create different colors and effects. The physical properties and microstructure of these additives within a coating or bulk material generate a specific, often wavelength dependent, scattering pattern. The material possesses a specific color and appearance based on the perception of the scattering pattern by a human observer. The microstructural contribution to color and appearance is the focus of the work presented in this thesis.

Color and Appearance

The appearance of a material is governed by the way a material scatters, absorbs, and transmits visible light and encompasses a range of properties including, but not limited to, color, texture, lightness, and gloss. All appearance information related to the reflected light is contained within a quantity known as the bidirectional reflectance distribution function (BRDF), which describes how the intensity of reflected light at a given angle of observation depends on the direction from which the surface is illuminated. In general, there are two extreme types of reflection. Specular reflection occurs from an optically smooth surface, where the angle of reflection equals the angle of incidence. Diffuse scattering occurs when light is reflected from a perfect matte surface, and the intensity of the reflected light is equal in all directions. Generally, reflecting surfaces (including paint systems) exhibit a mixture of specular and diffuse reflections

(**Figure I-1**), which lead to complicated forms of the BRDF [36,37] that depend on the details and microstructure of the reflecting surface.

Materials that contain spherical pigments that reflect light uniformly in all directions will possess a BRDF similar to the "diffuse" lobe shown in **Figure I-1**. Materials that utilize high aspect ratio scatters such as aluminum platelets will exhibit a BRDF that is a mixture of the "directionally diffuse" and "specular" lobes shown in **Figure I-1**. These platelet scatterers give rise to gonioapparent color. Gonioapparent color changes over a range of illumination and observation angles [38]. An example of two colors, one with gonioapparent behavior and one without, is shown in **Figure I-2**.

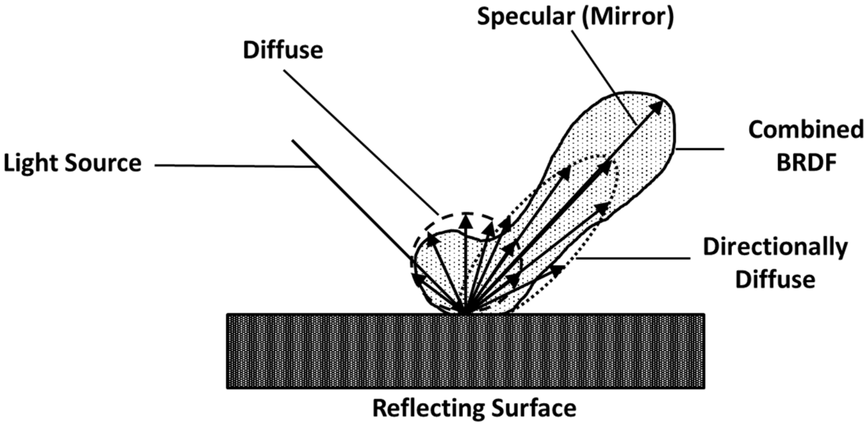

Figure I-1: Schematic of different BRDFs that result from perfectly specular, directionally diffuse, and diffuse surfaces. Also illustrated is a combined BRDF for a surface that consists of all three types of reflections.

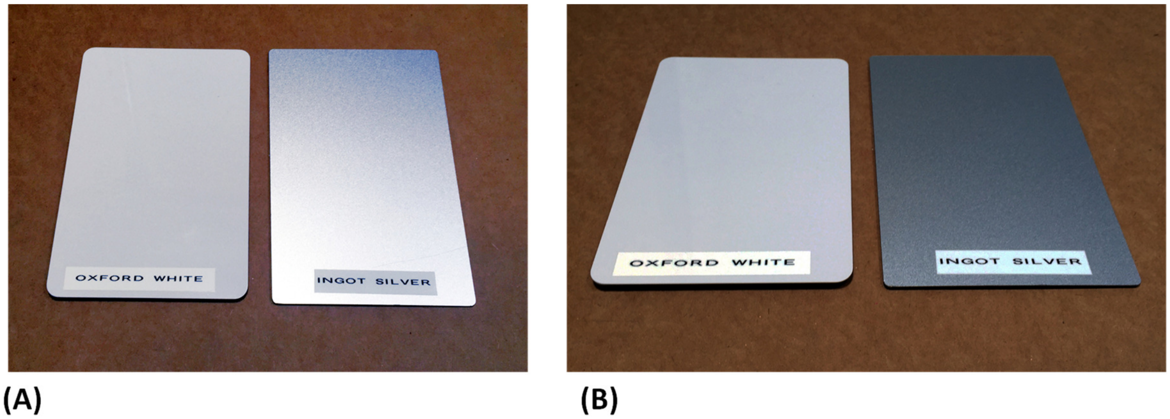

Figure I-2: Example of two standard automotive paint colors. Oxford White utilizes a nearly spherical titanium dioxide as the primary pigment and exhibits minimal gonioapparent behavior. Ingot Silver utilizes aluminum platelets as the primary pigment and exhibits significant gonioapparent behavior. Panel (A) shows the colors at a near specular reflection angle. Panel (B) shows the colors at an observation angle away from the specular reflection angle. The Oxford White does not exhibit a change in lightness between the two observation angles while the Ingot Silver darkens considerably away from specular.

The definition of color involves more than a simple measure of the wavelength or intensity of reflected light; there is a subjective aspect to color as well. Since it is useful to describe color in terms of quantifiable measurement specifications, the International Commission on Illumination (CIE) has developed standards to define color [39]. A color is described by three experimentally measured parameters mapped onto an orthogonal coordinate system. The coordinate system takes into account the features that induce physiological and psychological responses of the human eye and brain. The most commonly used system for paints is the "CIE1976 (LAB) color space" introduced in 1974 [38, 40–42], which uses components of color described as the lightness (*L**), the green-red component (*a**) and the yellow-blue component (*b**). The development of new products in the paint industry typically focuses on how changes in the composition or processing parameters affect the observed appearance through the use of CIE *L**, *a**, or *b** coordinates. Other coordinate systems are used in other industries, but because of limitations of many of the coordinate systems, no single governing set of equations is used across all industries [38]. The limitations usually manifest themselves when the question of “perceivable color difference” is discussed. For example, CIE1976 color space is defined as the difference between two colors as ΔE, where:

$$\Delta E = \sqrt{(\Delta L^*)^2 + (\Delta a^*)^2 + (\Delta b^*)^2} \quad , \qquad (1)$$

A ΔE of magnitude 1.0 should be perceived similarly regardless of the two colors being compared. Unfortunately, this is not the case, especially for metallic and interference colors. Work continues to create new and more accurate color difference formula (CIE94, CIEDE2000, CMC, DIN99) as new color technologies are developed and brought to market [38].

The microstructure and components of silver metallic paints typically cause changes in just lightness. As those paints are the focus of this work, *a** or *b** will remain constant across all samples and not be analyzed. As a result, only lightness value, *L**, will be discussed. It can be calculated from the equation [43]

$$L^* = 116\,(Y/Y_n)^{1/3} - 16, \qquad (2)$$

where Y is the measured intensity of the light reflected from the sample, and Y_n is the intensity of light that would be reflected at the same angle from a perfectly diffuse white reflector, while the constants, 116 and 16, and the exponent, 1/3, have been empirically determined [44]. The quantities Y and Y_n are one of the tristimulus values for both the sample and a diffuse white standard [45,46]. Tristimulus values—X, Y, and Z—are primary weighting functions created by CIE to match human color perception, from which any color can be created [38]. The governing equations for each of the tristimulus values are as follows:

$$X = k \sum_{i=1}^{N} S(\lambda_i) R(\lambda_i) \bar{x}(\lambda_i) \Delta\lambda \tag{3}$$

$$Y = k \sum_{i=1}^{N} S(\lambda_i) R(\lambda_i) \bar{y}(\lambda_i) \Delta\lambda \tag{4}$$

$$Z = k \sum_{i=1}^{N} S(\lambda_i) R(\lambda_i) \bar{z}(\lambda_i) \Delta\lambda \tag{5}$$

$$k = \frac{100}{\sum_{i=1}^{N} S(\lambda_i) \bar{y}(\lambda_i) \Delta\lambda} \tag{6}$$

The relative spectral power distribution of the illumination source is defined as $S(\lambda_i)$, the spectral reflectance spectrum of the object is defined as $R(\lambda_i)$, and $\bar{x}$, $\bar{y}$, $\bar{z}$ are the CIE color matching functions [44]. The final measured or perceived color of an object is based on each of these factors. CIE designed X and Z to describe the basic chroma and hue of a color, while Y is proportional to the lightness of the color. These equations are designed to quantify the physiological component of color perception, while color difference equations are designed to quantify both the psychological and physiological component of color perception.

Pigments and Paint

A coating or paint applied to an engineered structure or consumer product can provide a number of functions including corrosion protection, a specific gloss level, and a particular color. Many paints are multi-layered systems and possess a color layer called the basecoat, whose main purpose is to provide color to an object. Pigments, platelets, and other scatterers are added to the basecoat layer to impart a specific color [47–49]. A table listing the type of pigments used in decorative finishes and coatings, their material makeup, and their effects is shown in **Table I-1**.

Table I-1: Different pigment types used in decorative finish and coatings industry. Classifications and information within this table was detailed by Klein in *Industrial Color Physics* [44].

Pigment name/type	**Structure and layering**	**Optical/Appearance Effects**
Inorganic and organic absorption pigments	Organic or inorganic crystallites.	Diffuse scattering with absorptive color.
Uncoated metallic pigments	Metal or alloy platelet.	Gonioapparent lightness observed due to near-specular reflection from platelet surfaces.
Pearlescent pigments	Mica or metal/metal oxide substrate typically coated with a single, high index of refraction layer	Gonioapparent color observed due to single or multiple reflections from layer boundaries followed by interference of light waves.
Interference pigments	Metal or metal oxide substrate coated with multiple, high index of refraction layers. Different layer thicknesses and refraction indices used to enhance interference effects.	Behave similarly to pearlescent pigments with brighter interference colors. Color will change significantly due to angle of illumination and observation. Utilizes light wave interference.
Diffraction pigments	Metallic substrate with embossing, inorganic additives, or other surface treatment to create reflection grating.	Spacing of the grating can cause different platelet colors at specific angles of reflection. Very specialized.

A schematic of a typical automotive paint system is shown in **Figure I-3**. The pigment particles range in size from 0.01 μm to 80 μm in diameter, and have a variety of shapes and crystal structures [44]. Metallic platelets with diameters between 1 and 80 μm, and thicknesses between 0.3 and 1.33 μm, have been added to paint systems since 1935. Aluminum platelets are typically manufactured using the ball mill process detailed in **Figure I-4** [50]. These platelets produce variations in color and lightness as illumination and observation angles change [51,52]. By 2013, about 75% of all automotive original-equipment-manufacturer colors sold worldwide contained platelets [53], with aluminum platelets being particularly important [51,54,55]. In addition, silver metallic coatings are making inroads into the major home appliance [56] and the consumer electronics industry.

Physical attributes such as the absorption spectra and the refractive indices of the platelets contribute to the appearance of a painted surface [57–59]. However, the arrangement of the platelets within the paint also has a significant effect on the appearance. The microstructural parameter thought to have the most significant effect on the appearance of metallic paints is the distribution of the orientation angles of the platelets [51]. This distribution, in addition to other microstructural properties, is determined by the paint formulation, processing conditions, and the curing process [57]. While many platelets are oriented nearly parallel to the substrate, many are oriented at greater than 5° [60]. A schematic illustration of

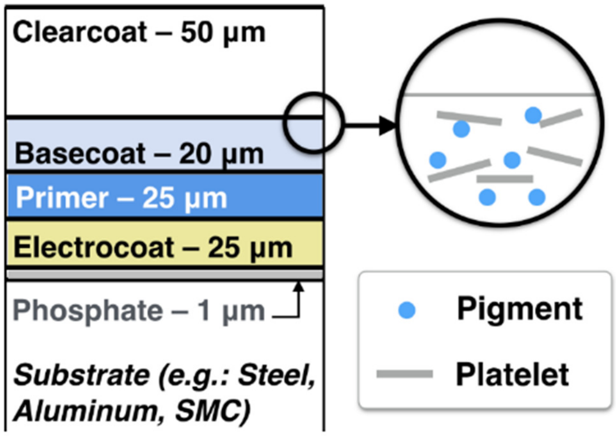

Figure I-3: Schematic of a typical exterior automotive paint system. Contained within the basecoat layer can be pigments and/or platelets. These scatterers provide the desired color and look to the overall paint system.

the spray droplet deposition process is shown in **Figure I-5**, with the effect of curing and shrinkage on the platelet orientation shown in **Figure I-6**. During spraying, the impact of droplets at the substrate will cause the liquid paint to splatter and the platelets to start to align parallel to the surface. The majority of platelet orientation occurs during solvent flash off where film shrinkage through solvent evaporation further aligns the platelets parallel to the substrate surface. An example of the final platelet arrangement is illustrated in a 2-D, cross-sectional view of a standard automotive silver-paint system in **Figure I-7**.

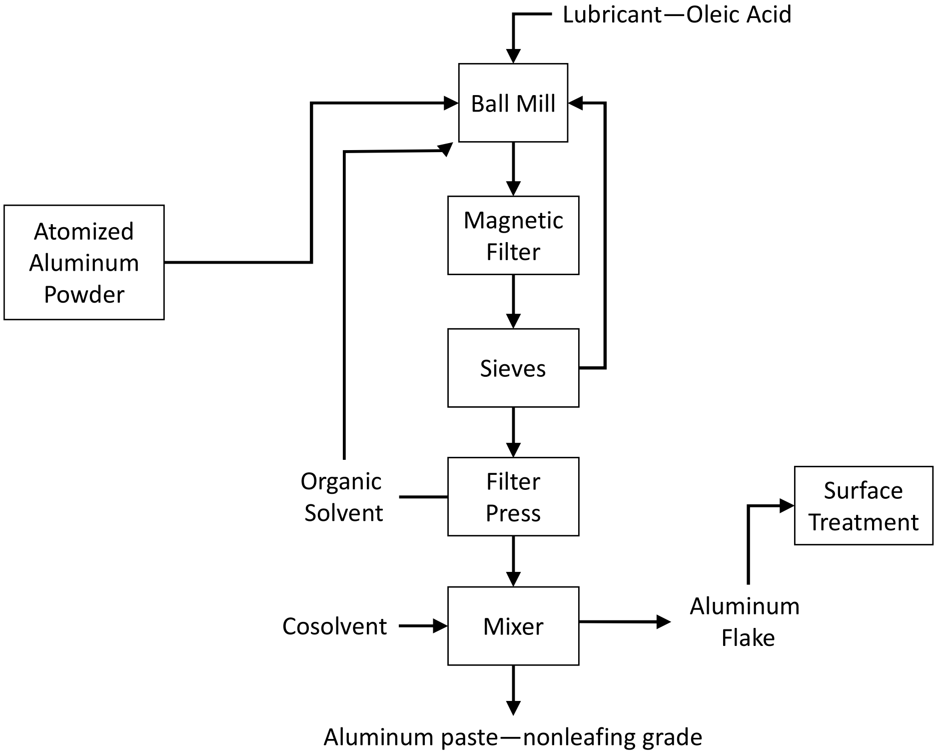

Figure I-4: Aluminum platelet manufacturing process [50].

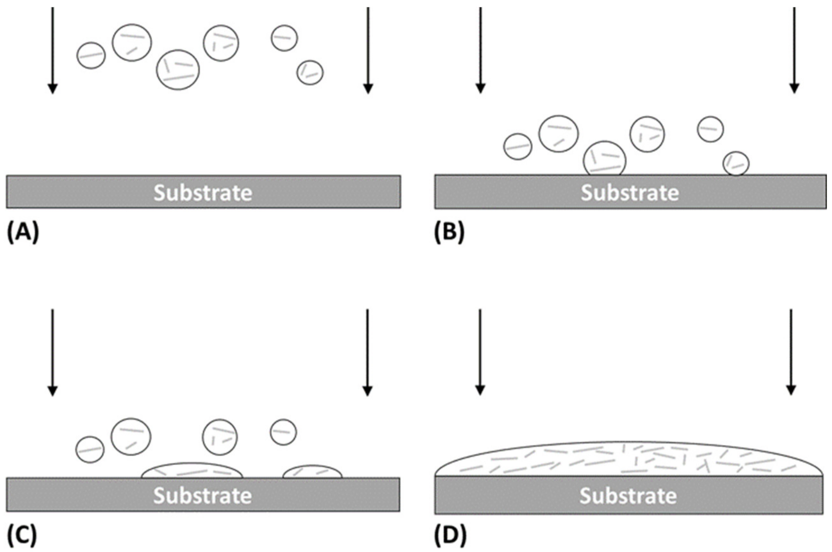

Figure I-5: Schematic of a typical spray process for a metallic paint system. Droplets contain a number of flakes depending on their size (A), they approach the surface and splatter (B). Upon impact, they spread out (C) which is the first physical process of platelet orientation. As more droplets impact, a complete paint film coalesces and the platelets flow together (D).

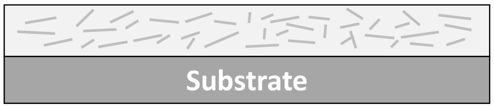

Prior to flash-off of solvent

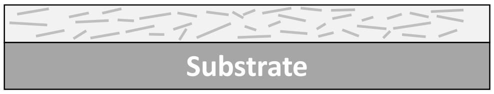

Post solvent flash, prior to cure

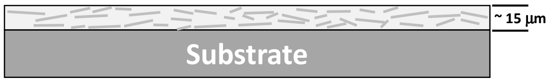

Post cure

Figure I-6: Platelet orientation progression during solvent flash and curing. The shrinkage of the film causes the flakes to align themselves parallel to the surface of the substrate. More shrinkage, and as a result, platelet orientation will occur in basecoats with higher solvent content.

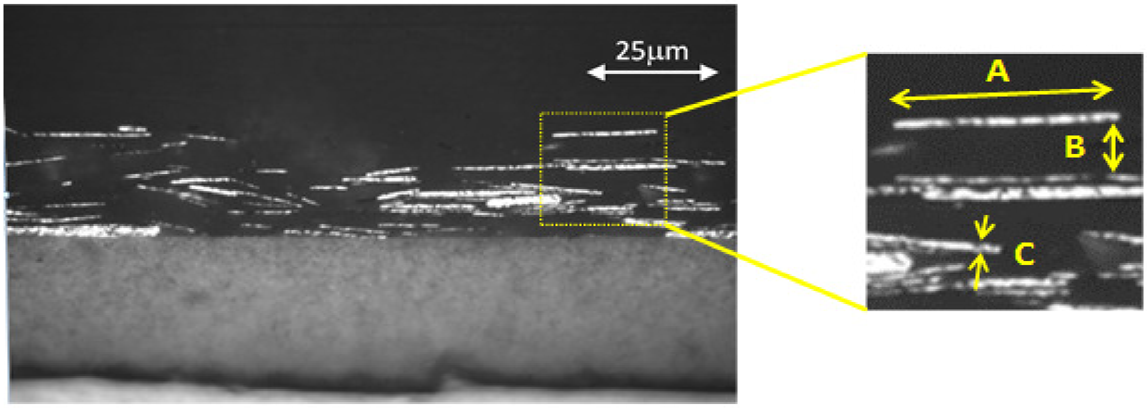

Figure I-7: Cross-sectional view of typical silver basecoat system (Silver #1). The magnified view (25µm x 25µm) shows the platelet diameter (A), the gap size (B), and the platelet thickness (C).

Predictive Modeling

Two methods have been employed by designers and formulators to predict how a paint system is affected by its constituents: (1) historical, empirical correlations between formulation changes and appearance, and (2) the incorporation of formulation and microstructural changes into a digital model. Each of these methods have advantages and deficiencies, discussed briefly below.

Empirical Modeling of Hypothetical Paint Systems

The use of empirical observations to predict the appearance of future paint systems is challenging for a variety of reasons. The appearance of the coating varies as platelet width, thickness, and volume concentration is changed [61–65]. However, the link between changes in these properties and the scattering behavior of the paint is not well understood due to the strong effect of application parameters on the microstructure. Changes to the bell speed, fluid flow, and spray pattern affect the atomization of the liquid paint, especially the size and momentum of the paint droplets arriving at the substrate surface. Ellwood showed the mean droplet diameter depends on the bell speed to the -2/3 power and the fluid flow to the 1/3 power, where the mean droplet diameter varies between 20-90 μm over the typical range of processing conditions [66]. Fan showed via simulation that the droplet velocity can range between 2-8 m/s across the spray pattern, giving rise to a range of splatter conditions upon impact with the substrate [67]. As a result, it is nearly impossible to predict how a new paint system will look based on a formulation change alone unless that paint system has already been physically produced and applied. Empirical correlations between formulation and appearance are only useful for incremental, minor changes to the paint formulation.

Digital Modeling of Hypothetical Paint Systems

Improved digital simulations of paint systems can, in principle, be employed to predict the appearance of new paint formulations. The simulations can additionally be used to explore the relationships between the size of the platelets, the microstructure—orientation, spacing, and pigment volume concentration (*PVC*) —and the optical scattering of the complete coating. In addition, digital simulations can, in principle, eliminate the effect of application conditions on the final platelet microstructure and be used to identify how specific microstructural changes affect the appearance of the finished system.

It is more difficult to simulate and render metallic colors than solid colors due to their gonioapparent nature. One method of rendering these colors accurately is to measure small sub-regions of the BRDF and interpolate the full scattering profile. Simple diffuse color systems were the first to be modeled, by Kubelka and Munk [68], and Saunderson [69]. These BRDF models have been incorporated into graphical rendering systems to render objects with a realistic color or “look” [70–73]. For gonioapparent colors, previous work has shown that as little as three angles of observation can be used to estimate the full BRDF [74,75]. However, this estimation can lead to angle specific color errors in cases where color or lightness changes quickly and/or interference effects exist. Currently, state-of-the-art color rendering can produce gonioapparent color behavior, but is not accurate enough to make engineering or design-based color decisions without additional physical sample analysis [76,77]. It is our goal to eliminate the majority of physical samples due to amount of time and money required to produce them during the color development process.

While significant progress has been made to model and render colors accurately, based on complete or partial BRDF scans, predictive modeling of colors from material and microstructural data is still lacking. No current model incorporates all microstructural aspects of paint system. As a result, existing models do not accurately predict the lightness of silver metallic paint systems with varying microstructures. Many models make compromises to achieve a realistic, if not accurate, representation of a silver metallic paint system. But, these models do not attempt to simulate the paint's complete 3D microstructure [78,79]. The following chapters will detail our work to quantify the microstructural properties of these paint systems and generate a model that cannot only predict the lightness and appearance of a silver metallic paint system, but can also be extended to accurately predict the scattering effects of any 3D scattering microstructure.

In this thesis, a detailed color model for paint systems containing aluminum platelets is created. The chapters presented are meant to stand alone and discuss the steps taken to create a model that captures the optical effects of different microstructural properties of the paint. Chapter II presents our efforts to measure and quantify the effects of the orientation and density of aluminum platelets on light scattering behavior of physical metallic paints. In addition, we attempted to use lightness observations to deduce the microstructure of the platelets and come up with the experimentally determined microstructures. From these attempts, a new microstructural property, based on the size of the gaps between the platelets, termed "*gap factor*", was introduced.

In Chapter III, we use the microstructures measured in Chapter II along with a second, smaller scale microstructural property—platelet roughness—to create a hybrid ray-wave based model to predict the color and appearance of a silver metallic paint system. The scattering of light from a metallic surface is incorporated into the model to improve the accuracy of the digital-physical match. We use this high-fidelity, 3D model to quantify the effect of surface roughness on the lightness of the complete paint system. From these results, color and pigment designers can understand how smooth a platelet surface must be to achieve a particular metallic paint system appearance.

Chapter IV utilizes the model presented in Chapter III to quantify how specific formulation and microstructural changes affect the gonioapparent lightness of the complete paint system. Recall these microstructure-scattering property relationships cannot be identified using physical samples due to the numerous changes in microstructure that can occur as a result of formulation and processing changes. However, the use of accurate digital simulations eliminates these confounding effects. In addition, we attempt to correlate the newly quantified “gap factor” to lightness changes in specific microstructures.

In Chapter V, we utilize the predictive model to simulate the appearance of precisely tailored aluminum platelet microstructures not currently achievable using today’s paint manufacturing technologies. The use of the model to predict the appearance of microstructures that contain other particles such as interference and structural color pigments and platelets will also be discussed. It is the goal for this work to be used as either a stand-alone development methodology or to be incorporated into a graphical rendering software package to accurately predict and visualize new color materials.

References

1. "Retail Sales Worldwide Will Top $22 Trillion This Year." EMarketer, 23 Dec. 2014. <www.emarketer.com/Article/Retail-Sales-Worldwide-Will-Top-22-Trillion-This -Year/1011765>.
2. "Cosmetics Market is Expected to Reach $390.07 Billion, Globally, by 2020." Allied Market Research, 27 May 2015. <www.prnewswire.com/news-releases/cosmetics-market-is-expected-to-reach-39007-billion-globally-by-2020---allied-market-research-505160571.html>
3. Nichols ME (2012) The Modeling and Rendering of Complex Automotive Paint. American Coatings Association Transportation Conference.
4. Valdez P and Mehrabian A (1994) Effects of Color on Emotions. Journal of Experimental Psychology: General, 123(4):394-409.
5. Bagchi R and Cheema A (2013) The Effect of Red Background Color on Willingness-to-Pay: The Moderating role of Selling Mechanism. Journal of Consumer Research 39(5):947-960.
6. Ershov S, Kolchin K, Myszkowski K (2001) Rendering Pearlescent Appearance Based On Paint‐Composition Modelling. EUROGRAPHICS 2001 20:227-238.
7. Germer TA, Nadal ME (2001) Modeling the appearance of special effect pigment coatings. International Symposium on Optical Science and Technology 1:77-86.
8. Cook RL, Torrance KE (1982) A reflectance model for computer graphics. ACM Transactions on Graphics (TOG) 1:7-24.
9. Weidlich A, Wilkie A (2007) Arbitrarily layered micro-facet surfaces. Proceedings of the 5th international conference on Computer graphics and interactive techniques in Australia and Southeast Asia. ACM 1:171-178.
10. Rump M, Müller G, Sarlette R, Koch D, Klein R (2008) Photo-realistic Rendering of Metallic Car Paint from Image Based Measurements. Computer Graphics Forum 27:527-536.
11. Germer TA, Marx E (2004) Ray model of light scattering by flake pigments or rough surfaces with smooth transparent coatings. Appl Opt 43:1266-1274.
12. Schubert C, van Langeveld MC, and Donoso LA (2013) Innovations in 3D printing: a 3D overview from optics to organs. British Journal of Ophthalmology bjophthalmol-2013.
13. Berman B (2012) 3-D printing: The new industrial revolution. Business horizons 55.2:155-162.
14. Martin JE, Hill KM, and Tigges CP (1999) Magnetic-field-induced optical transmittance in colloidal suspensions. Physical Review E 59.5:5676.
15. Jin S, Tiefel TH, and Wolfe R (1992) Directionally-conductive, optically-transparent composites by magnetic alignment. Magnetics, IEEE Transactions on 28.5:2211-2213.
16. Hanlon R (2007) Cephalopod dynamic camouflage. Current Biology 17.11: R400-R404.
17. Barbosa A, Litman L, and Hanlon RT (2008) Changeable cuttlefish camouflage is influenced by horizontal and vertical aspects of the visual background. Journal of Comparative Physiology A 194.4:405-413.

18. Beckmann P, Spizzichino A (1987) The scattering of electromagnetic waves from rough surfaces. Artech House, Inc., Norwood.
19. Aden AL and Kerker M (1951) Scattering of electromagnetic waves from two concentric spheres. Journal of Applied Physics. 22(10):1242-1246.
20. Barber PW and Yeh C (1975) Scattering of electromagnetic waves by arbitrarily shaped dielectric bodies. Applied Optics. 14(12):2864-2872.
21. Stefanou N, Karathanos V, and Modinos A (1992) Scattering of electromagnetic waves by periodic structures. Journal of Physics: Condensed Matter. 4(36):7389.
22. Hansen JE and Travis LD (1974) Light scattering in planetary atmospheres. Space Science Reviews. 16(4):527-610.
23. Snieder R (1986) The influence of topography on the propagation and scattering of surface waves. Physics of the earth and planetary interiors. 44(3):226-241.
24. Ward KD, Baker CJ, and Watts S (1990) Maritime surveillance radar. I. Radar scattering from the ocean surface. In Radar and Signal Processing, IEE Proceedings F. 137(2):51-62.
25. Jones WL and Schroeder LC (1978) Radar backscatter from the ocean: dependence on surface friction velocity. Boundary-Layer Meteorology. 13(1-4):133-149.
26. Stover JC (1995) Optical scattering: measurement and analysis (Vol. 2). Bellingham, WA: SPIE optical engineering press.
27. Theodorakopoulos N and Jäckle J (1976) Low-frequency Raman scattering by defects in glasses. Physical Review B. 14(6):2637.
28. Warren BE (1969) X-ray Diffraction. Reading, MA: Addison-Wesley
29. Guinier A (1994) X-ray diffraction in crystals, imperfect crystals, and amorphous bodies. New York, NY: Dover Publications, Inc.
30. Shi H, Ok JG, Baac HW, and Guo LJ (2011) Low density carbon nanotube forest as an index-matched and near perfect absorption coating. Applied Physics Letters. 99(21):211103.
31. Zikidis K, Skondras A, and Tokas C (2014) Low Observable Principles, Stealth Aircraft and Anti-Stealth Technologies. Journal of Computations & Modelling. 4(1):129-165.
32. Huang Y, Feng Y, and Jiang T (2007) Electromagnetic cloaking by layered structure of homogeneous isotropic materials. Optics express. 15(18):11133-11141.
33. Schurig D, Mock JJ, Justice BJ, Cummer SA, Pendry JB, Starr AF, and Smith DR (2006) Metamaterial electromagnetic cloak at microwave frequencies. Science. 314(5801):977-980.
34. Alù A and Engheta N (2008) Multifrequency optical invisibility cloak with layered plasmonic shells. Physical review letters. 100(11):113901.
35. Jansen H, Boer M de, Legtenberg R, and Elwenspoek M (1995) The black silicon method: a universal method for determining the parameter setting of a fluorine-based reactive ion etcher in deep silicon trench etching with profile control. Journal of Micromechanics and Microengineering 5(2):115–120.
36. Nicodemus FE (1965) Directional reflectance and emissivity of an opaque surface. Appl Opt 4:767-773.
37. Ashikhmin M, Premoze S (2007) Distribution-based brdfs. Unpublished Technical Report, University of Utah 2.
38. Wyszecki G, Stiles WS (1982) Color science. Wiley, New York.

39. CIE 1931 (1931) “Proceedings of the Eighth Session.”, Cambridge, England 1931; CIE, Bureau Central de la CIE, Paris, France.
40. Schanda J (2007) Colorimetry: Understanding the CIE system. John Wiley & Sons, Hoboken.
41. McLaren K (1976) XIII–The development of the CIE 1976 (*L** *a** *b**) uniform colour space and colour ‐ difference formula. Journal of the Society of Dyers and Colourists 92:338-341.
42. Robertson AR (1990) Historical development of CIE recommended color difference equations. Color Research & Application 15:167-170.
43. Pauli H (1976) Proposed extension of the CIE recommendation on “Uniform color spaces, color difference equations, and metric color terms”. JOSA 66:866-867.
44. Klein GA, Meyrath T (2010) Industrial color physics. Springer, New York.
45. Wright WD (1929) A re-determination of the trichromatic coefficients of the spectral colours. Transactions of the Optical Society 30:141-164.
46. Guild J (1932) The colorimetric properties of the spectrum. Philosophical Transactions of the Royal Society of London.Series A, Containing Papers of a Mathematical or Physical Character 1:149-187.
47. Lambourne R, Strivens T (1999) Paint and surface coatings: theory and practice. Elsevier, West Sussex.
48. Levinson R, Berdahl P, Akbari H (2005) Solar spectral optical properties of pigments—Part I: model for deriving scattering and absorption coefficients from transmittance and reflectance measurements. Solar Energy Mater Solar Cells 89:319-349.
49. Gunde MK and Orel ZC (2000) Absorption and scattering of light by pigment particles in solar-absorbing paints. Appl Opt. 39:622-628.
50. Streitberger HJ and Dossel KF (2008) Automotive Paints and Coatings. Wiley-VCH Verlag GmbH & Co. Weinheim.
51. McCamy C (1996) Observation and measurement of the appearance of metallic materials. Part I. Macro appearance. Color Research & Application 21:292-304.
52. Maile FJ, Pfaff G, Reynders P (2005) Effect pigments—past, present and future. Progress in Organic Coatings 54:150-163.
53. Dunlop A (2013) Internal Ford Motor Company metrics.
54. Rodrigues A (2004) Color technology and paint. Color and Paints Interim Meeting of the International Color Association Proceedings 1:103-108.
55. Pfaff, G. (2001) Special Effect Pigments. High Performance Pigments (ed H. M. Smith), Wiley-VCH Verlag GmbH & Co. KGaA, Weinheim, FRG.
56. Moe J (2015) Prepainted Technology Continues to Advance. Appliance Design <www.appliancedesign.com/articles/94510-prepainted-technology-continues-to-advance>
57. Lambourne R, Strivens T (1999) Paint and surface coatings: theory and practice. Elsevier, West Sussex.
58. Levinson R, Berdahl P, Akbari H (2005) Solar spectral optical properties of pigments—Part I: model for deriving scattering and absorption coefficients from transmittance and reflectance measurements. Solar Energy Mater Solar Cells 89:319-349.
59. Gunde MK, Orel ZC (2000) Absorption and scattering of light by pigment particles in solar-absorbing paints. Appl Opt 39:622-628.
60. Kirchner E and Houweling J (2009) Measuring flake orientation for metallic coatings. Progress in organic coatings 64.2:287-293.

61. McCamy C (1996) Observation and measurement of the appearance of metallic materials. Part I. Macro appearance. Color Research & Application 21:292-304.
62. Kirchner E, van den Kieboom GJ, Njo L, Super R, Gottenbos R (2007). Observation of visual texture of metallic and pearlescent materials. Color Research & Application 32:256-266.
63. Klein GA, Meyrath T (2010) Industrial color physics. Springer, New York.
64. Maile FJ, Pfaff G, Reynders P (2005) Effect pigments—past, present and future. Progress in Organic Coatings 54:150-163.
65. Pfaff, G. (2001) Special Effect Pigments. High Performance Pigments (ed H. M. Smith), Wiley-VCH Verlag GmbH & Co. KGaA, Weinheim, FRG.
66. Ellwood KRJ, Tardiff JL, and Alaie SM (2014) A simplified analysis method for correlating rotary atomizer performance on droplet size and coating appearance. Journal of Coatings Technology and Research 11.3:303-309.
67. Fan HT, Kuo H, and Simmer J (2011) Measuring Paint Droplet Size, Velocity, and Charge-to-Mass Ratio Distribution for Electrostatic Rotary Bell Spray Simulation. ASME 2011 International Mechanical Engineering Congress and Exposition 703-709.
68. Kubelka P, Munk F (1931) An article on optics of paint layers. Z. Tech. Phys 12:593-601.
69. Saunderson JL (1942) Calculation of the color of pigmented plastics. JOSA 32:727-729.
70. Abdul-Rahman A, Chen M (2005) Spectral Volume Rendering based on the Kubelka-Munk Theory. Computer Graphics Forum 24:413-422.
71. Lei SIE, Chang CF (2005) Real-time rendering of watercolor effects for virtual environments. Advances in Multimedia Information Processing-PCM 2004, Springer, Berlin, 474-481.
72. Huang CG, Huang TS, Lin WC, Chuang JH (2013). Physically based cosmetic rendering. Computer Animation and Virtual Worlds 24: 275-283.
73. D'Eon E, Luebke D, Enderton E (2007) Efficient rendering of human skin. Proceedings of the 18th Eurographics conference on Rendering Techniques Eurographics Association, 147-157.
74. Alman DH (1987) Directional color measurement of metallic flake finishes. Proceedings of the ISCC Williamsburg Conference on Appearance
75. Rodrigues ABJ (1990) Measurement of metallic and pearlescent finishes. Die Farbe 37:65-78.
76. Bärz J, Henrich N, Müller S (2010) Validating Photometric and Colorimetric Consistency of Physically-Based Image Synthesis. Conference on Colour in Graphics, Imaging, and Vision, Society for Imaging Science and Technology 148-154.
77. Takagi, A., Takaoka, H., Oshima, T., & Ogata, Y. (1990). Accurate rendering technique based on colorimetric conception. ACM SIGGRAPH Computer Graphics, 24(4), 263-272.
78. Ashikmin M, Premoze S, Shirley P (2000) A microfacet-based BRDF generator. Proceedings of the 27th annual conference on Computer graphics and interactive techniques. ACM Press/Addison-Wesley Publishing Co. 65-74.

79. Jakob W, Hasan M, Yan LQ, Lawrence J, Ramamoorth R, Marschner S (2014) Discrete stochastic microfacet models. ACM Transactions on Graphics (TOG), 33*:*115.

Chapter II

The characterization and effects of microstructure on the appearance of platelet-polymer composite coatings

Introduction

Although color and appearance have a psychological component, they are material properties that can be of considerable significance and economic importance to designers and engineers alike. Paint systems are materials that have a primary role of modifying the appearance of an engineered structure. Very little work, however, has been performed to determine the necessary structure-property relationships necessary to create the desired predictive model. In the computer-graphics community, coatings are simulated by incorporating the BRDF (or a simplified model of it) into the rendering. These can be obtained by direct measurement of paint systems [1,2]. Other approaches involve deriving a BRDF from models of primary ray scattering of the platelets [3–8]. However, experimental evidence to link these models to actual physical systems is lacking. The only work linking experimental observations of the platelets in an automotive paint to the resultant appearance is that presented by Sung [9] and Kettler [10], who explored the role of platelet orientation.

In the present chapter, we build on this earlier work by developing a more systematic investigation into how the platelet size, *PVC*, and spray conditions affect the paint's appearance.

This allows us to identify other microstructural properties beyond orientation that may play a role in the appearance of a metallic paint system. This work is a critical first step towards the creation of a direct link between formulation (processing), microstructure, and appearance (properties) in platelet-containing paint systems. The chapter is organized as follows. First, we review the main relevant advances in the science of color. Second, we present a model for the structure of the paint system under consideration, where metallic micro-platelet density and orientation affect light reflection. Third, we use this model to relate light scattering properties to the platelets' orientation, allowing for reverse-engineering of predicted microstructure from appearance. Finally, we compare the results of these predictions to the experimentally determined microstructures.

Microstructure of paint system

Modern automotive paints are composite systems, containing pigments and metal platelets. The pigment particles range in size from 0.01 μm to 80 μm in diameter, and have a variety of shapes and crystal structures [11]. Metallic platelets with diameters between 1 and 80 μm, and thicknesses between 0.3 and 1.33 μm, were added to paint systems as early as 1935. At these thicknesses, no visible light is transmitted through the platelets that either absorb or reflect the light. Therefore, the surface platelets shadow the deeper ones. The high aspect ratio of the platelets and the 3D microstructure give rise to interesting and unique visual affects not achievable with spherical pigments.

Historically, the orientation of platelets within a polymer matrix has been measured using 2-D cross sections [12,13]. This technique is time consuming, and extracting a 3-D description of the distribution of the platelets requires extensive stereographic analysis [14]. Other techniques, such as X-ray [15,16] and ion-microbeam analyses [17,18], are even more time consuming. Recently, researchers have begun to use laser-scanning confocal microscopy to create full 3-D representations of aluminum platelets, and to quantify orientation changes associated with different formulation and spray conditions [9,19]. This technique will be used to characterize the microstructure of the paints examined in this study.

While LSCM provides a technique to obtain the 3-D distributions of platelets, a limited amount of work has been done to determine if an accurate description of the platelet orientation distribution can be extracted from scattering data for a complete system [9]. In that previous work, differences between the predicted and measured scattering profile were attributed to the platelet's surface roughness, which led to a wider specular reflection lobe from the platelet's surface. If it could be shown that the orientation distribution and the scattering profile are closely linked, then the orientation of the platelets could be determined by scattering measurements, rather than by the more-involved microscopy studies. Simpler micro-facet models for these systems could also be employed if this were the case.

Model for color

The relationship between scattering and microstructure in these paint systems can be modeled assuming the majority of scattering events occur as the result of single-reflection events (no multiple reflections). If the incident light comes from a single angle, the intensity of scattered light at a given angle of observation, θ_{OUT}, is directly related to the surface area of platelets at different orientations. A schematic illustration of such a single-reflection event is shown in **Figure II-1**.

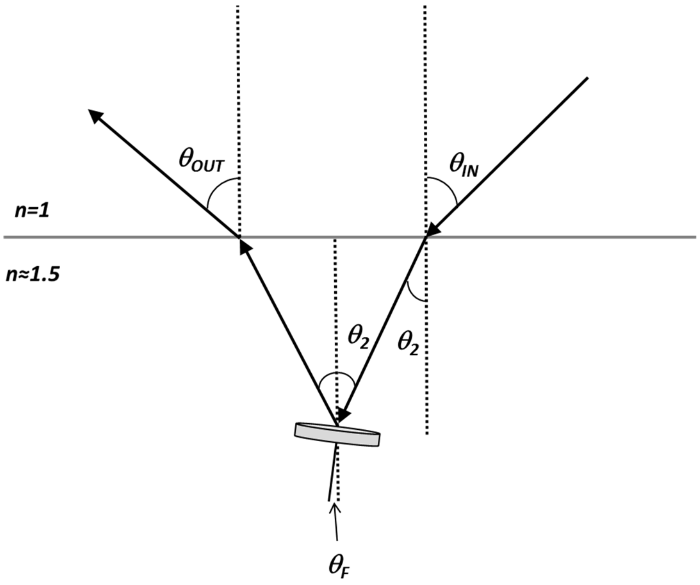

Figure II-1: A schematic figure illustrating a single reflection from a metallic platelet in a paint system. Incident light enters the system at an angle of θ_{IN}. The light is then refracted by the air-clearcoat interface to a new angle (θ_2). The light progresses through the clearcoat layer until it reflects off of a platelet—in this case, the platelet face. The angle from normal of the platelet (θ_F) will determine the angle that the light intersects the air-clearcoat interface. This refraction will lead to the ray's exit angle of θ_{OUT}. This ray propagation is only true for single reflection, face reflections. If the ray strikes more than one platelet, a platelet edge, or the primer layer below, the ray will follow a different propagation path.

To relate the incident and exit angles for a given platelet correctly, refraction at the clearcoat/air interface must be accounted for. As the index of refraction of the polymer matrix (typically ~1.5) [20] is greater than that of air, the angle of incidence of any light that interacts with the system will change at the polymer/air interface (in this case, the top of the clearcoat layer). From Snell's law, the incident angle for a given platelet can be expressed as

$$\theta_2 = \sin^{-1}\left({}^{1}/_{1.5} \sin \theta_{IN}\right) , \tag{1}$$

where θ_2 is the incident angle after refraction, θ_{IN} is the initial angle of incidence with respect to the clearcoat surface, with the refractive indices for air and the clearcoat being 1 and 1.5, respectively. For the experiments that are described later, the angle of incidence is $\theta_{IN} = 45°$ and, therefore, $\theta_2 = 28°$. After the incident light is reflected from the platelets, it is refracted again at the surface of the clearcoat. The exit angle for the reflected light, θ_{OUT}, is then given by

$$\theta_{OUT} = \sin^{-1}(1.5 \sin(\sin^{-1}({}^{1}/_{1.5} \sin \theta_{IN}) - 2\theta_F) , \tag{2}$$

where θ_F is the angle of orientation for the platelet orientation angle. If it is assumed that the platelets all have the same size, the predicted intensity of light in a particular direction depends on the distribution of orientation angles for the platelets. From this, the lightness, L^*, can be computed using the following equation [21]:

$$L^* = 116 \, (Y/Y_n)^{1/3} - 16, \tag{3}$$

where Y is the measured intensity of the light reflected from the sample, and Y_n is the intensity of light that would be reflected at the same angle from a perfectly diffuse white reflector, while the constants, 116 and 16, and the exponent, 1/3, have been empirically determined.

Experiments & Results

Materials

A set of automotive basecoat/clearcoat acrylic paint systems with varying platelet sizes, *PVCs*, and application conditions was studied. Thus, a comparison between scattering and morphology could be made across a larger scope of samples than has previously been done [9]. Samples were prepared using standard automotive coating techniques**.** The target thickness of the cured basecoat layer was 20 μm. The basecoat layer was flash dried at ambient conditions to allow for solvent evaporation, before the acrylic clearcoat layer, with a target thickness of 50 μm, was applied. The samples were cured in a convection oven for 20 minutes at 130^{o}C.

Images of the finished samples were taken at 15^{o} off-specular (OS) under daylight illumination provided by a MacBeth light booth (X-Rite Inc., Grand Rapids, MI USA). These images are shown in **Figure II-2.**

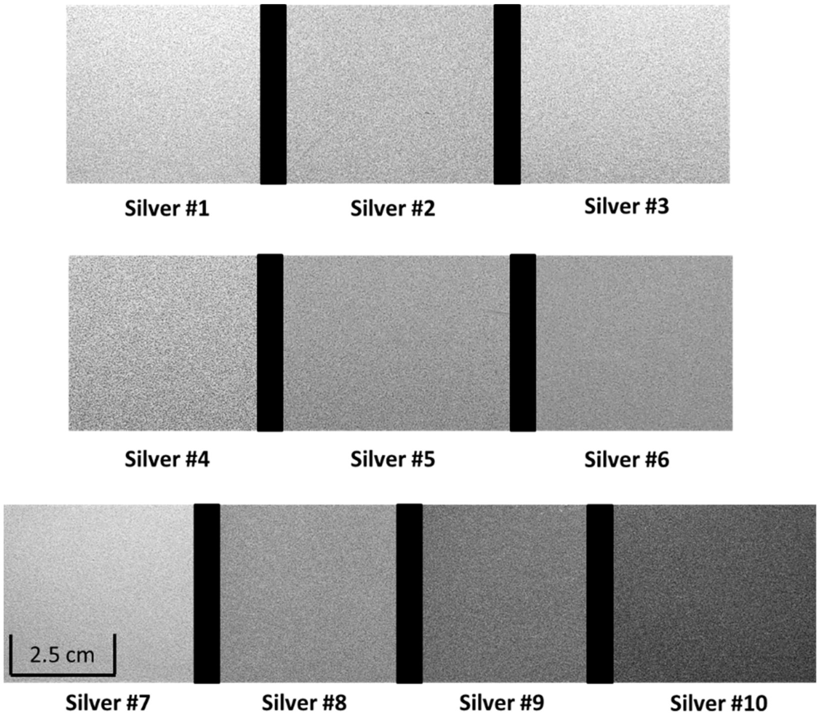

Figure II-2: Digital images taken of each silver sample under study. Samples were imaged at 15^o OS under daylight illumination from a MacBeth light booth. Silver #1-Silver #3 were applied under different process conditions. Silver #4-Silver #6 were formulated with different platelet sizes. Silver #7-Silver #10 were formulated with different *PVCs* of like platelets. Measured lightness values for each sample are listed in **Table II-1.**

Table II-1: Formulation (as provided by supplier, where appropriate), application, and measurement details for the ten prepared silver samples. The target for the clearcoat and basecoat thicknesses for all samples was 50 μm and 20 μm, respectively.

Sample Name	Pigment: Binder Mass Ratio	Approx. Platelet *PVC*	Median Platelet Diameter (μm)	Average Platelet Thickness (μm)	*L** @ 15° OS (*θ_{OUT}=30°*)	Median Orientation Angle from microscopy (degrees)	RMS_{Error} (CDF%)	Gap Factor (gap size per unit sample length)	Application Method[22]
Silver #1	0.18	7.6%	17 ± 0.5	0.55 ± 0.02	143.3 ± 0.3	4.1 ± 0.4	0.02 ± 0.01	0.26 ± 0.01	Electrostatic Bell, Low Fluid Flow (90 cc/min)
Silver #2	0.18	7.6%	17 ± 0.5	0.55 ± 0.02	129.0 ± 0.3	5.3 ± 0.3	0.05 ± 0.02	0.32 ± 0.01	Electrostatic Bell, High Fluid Flow (210 cc/min)
Silver #3	0.18	7.6%	17 ± 0.5	0.55 ± 0.02	137.2 ± 0.3	4.0 ± 0.3	0.04 ± 0.02	0.33 ± 0.01	Electrostatic Bell, Nominal Fluid Flow (150 cc/min)
Silver #4	0.32	12.1%	25 ± 0.75	0.66 ± 0.03	130.2 ± 0.3	4.2 ± 0.3	0.03 ± 0.01	0.26 ± 0.01	Electrostatic Bell
Silver #5	0.11	4.4%	18.5 ± 0.56	0.58 ± 0.03	114.6 ± 0.3	5.3± 0.4	0.06 ± 0.01	0.31 ± 0.01	Electrostatic Bell
Silver #6	0.10	4.0%	11.5 ± 0.35	0.63 ± 0.03	108.3 ± 0.3	4.9 ± 0.3	0.10 ± 0.01	0.35 ± 0.01	Electrostatic Bell
Silver #7	0.19	7.6%	17 ± 0.5	0.61 ± 0.03	144.8 ± 0.3	3.1 ± 0.2	0.08 ± 0.02	0.16 ± 0.01	Spray gun
Silver #8	0.09	4.0%	17 ± 0.5	0.61 ± 0.03	119.2 ± 0.3	5.1 ± 0.4	0.06 ± 0.02	0.36 ± 0.01	Spray gun
Silver #9	0.05	2.0%	17 ± 0.5	0.61 ± 0.03	101.3 ± 0.3	6.4 ± 0.3	0.05 ± 0.02	0.30 ± 0.01	Spray gun
Silver #10	0.02	1.0%	17 ± 0.5	0.61 ± 0.09	87.5 ± 0.3	7.0 ± 0.4	0.0540 ± 0.017	0.30 ± 0.01	Spray gun

The systems identified as "Silver #1" through "Silver #3" were silver formulations, sprayed to hiding (minimal transmission) with a rotary bell applicator onto steel panels that had been previously coated with a grey automotive primer. The same basecoat and clearcoat formulations were applied to all three samples, but they were sprayed at different flow rates. The droplet size becomes more variable as the flow rate is increased, resulting in less control over the deposition of the droplets, which is thought to result in more disoriented platelets before curing [23,24].

The systems identified as Silver #4 through Silver #6 were also formulated to prevent light transmission through basecoat layer. Each was formulated with a different size platelet, ranging in diameter from 11.5-25 μm. All three basecoats and the clearcoats were applied to steel panels that had been previously coated with a grey automotive primer.

The systems identified as "Silver #7" through "Silver #10" were formulated from the same initial composition (Silver #7), but the platelet concentration was progressively reduced by diluting Silver #8 through Silver #10 with unpigmented resin. The coatings were manually applied with a high-volume low-pressure (HVLP) spray gun to primed steel panels. The clearcoat layer was applied with a drawdown bar (a device used to manually draw a wet film over a substrate at a constant thickness) after the basecoat was cured. These systems were deposited on a black automotive primer (to eliminate reflection off of the primer layer in the non-hiding formulations), but had the same target thickness of 20 μm for the basecoat and 50 μm for the clearcoat.

Characterization of Microstructure

Direct measurements of the platelet/polymer composite microstructures were accomplished using Laser Scanning Confocal Microscopy (LSCM). This technique allowed for the creation of platelet orientation distributions for each of the analyzed systems. LSCM images were acquired using a Zeiss LSM 5 Pascal LSCM (Thornwood, NY) configured on a Zeiss Axioskop 2 upright microscope. LSCM uses a laser light source and collects the reflected light within the focal plane of the measurement. Light outside the focal plane is rejected. The focal plane is moved step-wise through the sample thickness to collect a series of images, which can later be combined into a 3D image of the entire sample. The series of confocal reflected-light images were acquired using the 488 nm Argon gas laser line, viewing through the top thickness of about 20 µm of the basecoat in 0.25 µm steps, with a 40x Plan-Neofluar oil objective (NA 1.3). Topographic analyses were performed on the confocal image series using the Zeiss LSM 5 Pascal Topography software. MountainsMap surface-analysis software from Digital Surf (Besançon, France) was used to calculate the area, normal, and azimuthal angle of each visible platelet. The normal angle is the planer angle between the vector perpendicular to the clearcoat surface and the vector perpendicular to the platelet's face ($0^o – 90^o$). The azimuthal angle is the spherical angle of the vector perpendicular to the platelet's face ($0^o – 360^o$). Typically, 5 to 6 distinct regions were measured to collect data from a statistically significant number of platelets (400-500), so that the orientation distribution across from each system was reliably obtained.

LSCM images were obtained for each of the ten samples at multiple locations on each panel. An example of a height map for Silver #1 is shown in **Figure II-3.** One specific advantage of LSCM measurements, as opposed to 2D cross-sectional measurements, is that the LSCM only images the platelets (partial and full) that are immediately observable by incident light. These particular platelets are the ones that directly affect the appearance that is the primary focus of this study. Platelets deeper within the system that are completely covered by surface platelets do not contribute as directly to the appearance. Data for the normal and azimuthal angles were measured for each visible platelet using the height maps. The absence of any obvious azimuthal orientation of the platelets confirmed a random distribution in that direction. This is shown for the Silver #1 data in **Figure II-4A**.

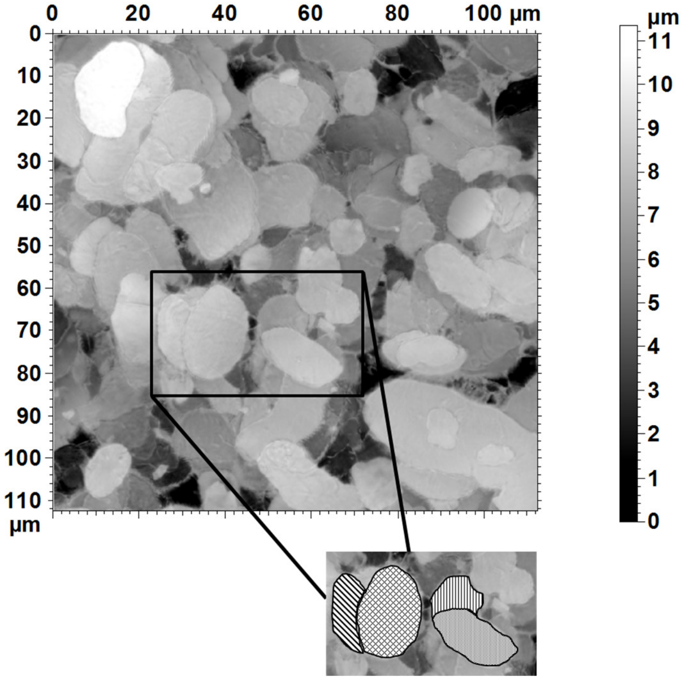

Figure II-3: A height map for the Silver #1 sample obtained from laser-scanning-confocal microscopy. LSCM can only image platelet directly viewable from the surface normal direction. Many platelets are partially shadowed by other platelets. The visible area of some example individual platelet regions are highlighted in the callout. The angular data from each of these regions was weighted by each platelet's relative area to determine if this affected the match between the orientations produced by scattering and LSCM.

As the azimuthal angles were random, only the normal angles of the platelets were considered to be of consequence; these were the only angles considered in the rest of this work.

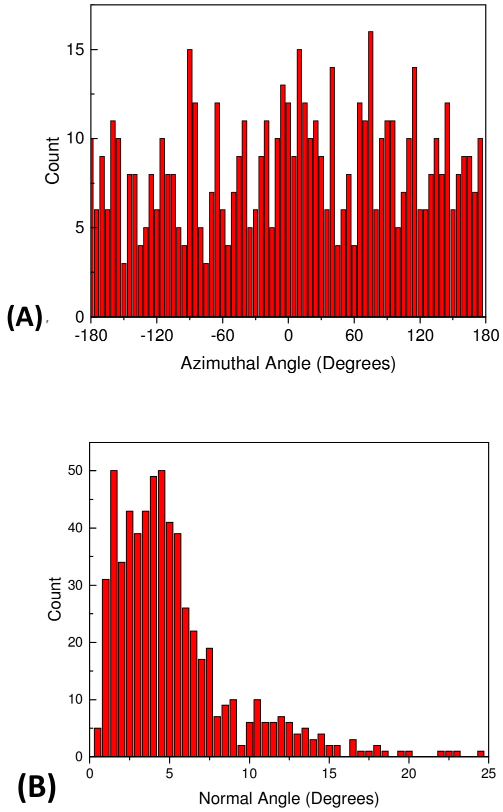

Figure II-4: (A) Azimuthal angle counts (bin size of 5°) measured for Silver #1. The azimuthal angle data showed no obvious trend or bias. As a result, the azimuthal angle was assumed to be random. (B) Normal angle counts (bin size of 0.5°) measured for Silver #1. The normal angle does have a clear bias and distribution, with a maximum frequency of ~5°. The exact shape of this distribution varied slightly from sample to sample. It was this variation that was partially responsible for lightness variations between the samples.

The distribution of normal angles for the orientation of the platelets (θ_F) was measured from the LSCM images. An example of the raw data is shown in **Figure II-4B** for Silver #1. These frequency data were then integrated and normalized to a total value of 1.0 to produce the cumulative-distribution functions (CDFs) for each sample. To provide a point of comparison for these data, hypothetical examples of the CDFs corresponding to the system with (i) a perfectly parallel orientation, (ii) a good orientation, (iii) a poor orientation, and (iv) a perfectly random orientation are shown in **Figure II-5.** The CDFs for the three sets of paints are shown in **Figure II-5B-D**. In these plots, the angles for all the platelets were weighted equally, and were not adjusted for size of the platelets.

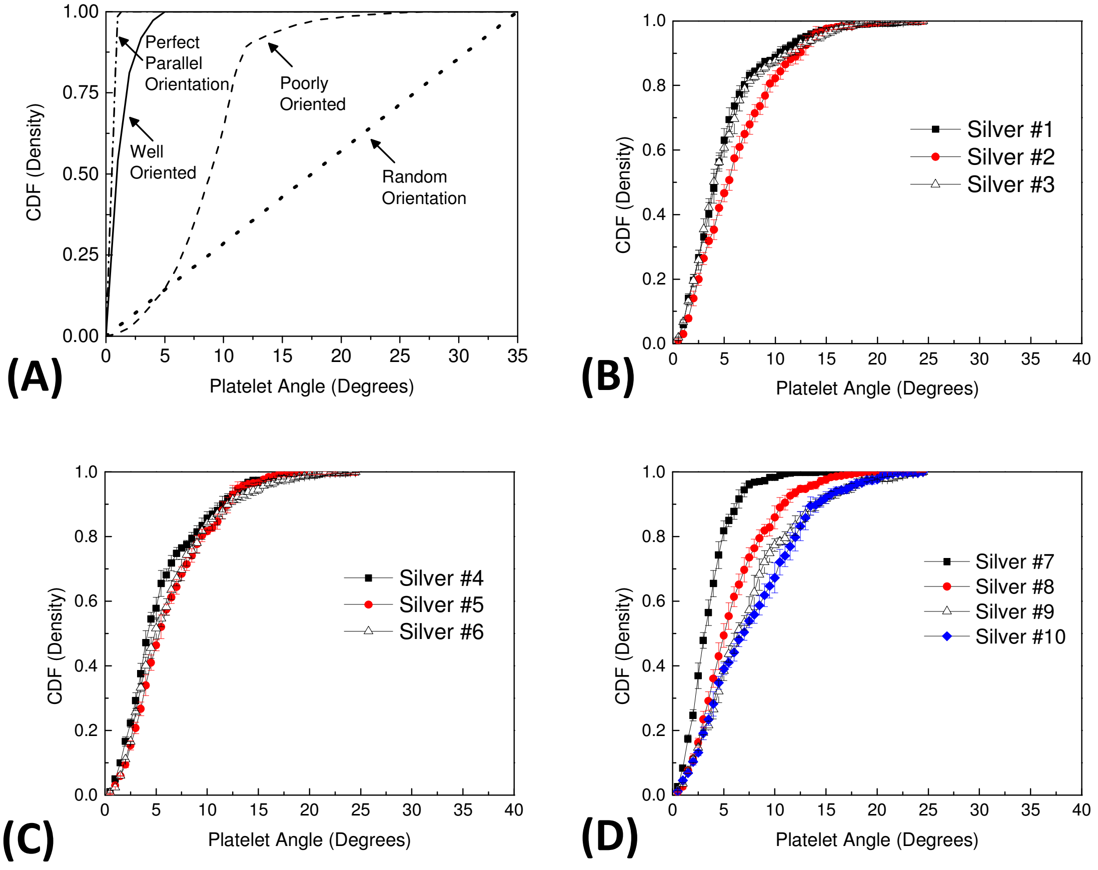

Figure II-5: (A) The expected cumulative-density functions (CDFs) for perfectly oriented, well oriented, poorly oriented, and randomly oriented platelet systems. (B-D) Measured CDFs for the orientation for each paint system, as determined from LSCM observations.

Prediction of microstructure from scattering data

The appearances of the different systems were measured using scattering experiments in which the samples were illuminated at a given angle of incidence, with the scattered light being collected at specific angles of observation. The scattered intensities were measured using a Radiant Zemax IS-SA Imaging Sphere (Redmond, WA). The IS-SA Sphere uses a hemispherical mirror to measure 2π steradians of scattered light at one time. The collimated incident light was produced by a xenon light source that illuminated a 20 mm diameter circular region from which the scattering data were obtained. The measurements were taken at a wavelength of 555 nm.

The angular resolution of the measurements was 0.5°. A single scattering profile of each sample was determined by illuminating the sample at 45° from the normal, and measuring the scattered intensity across the hemisphere. An example of the resulting spherical contour plot of the scattered intensity for Silver #1 is shown in **Figure II-6**. The lightness values, L^*, for each sample 15° OS (θ_{OUT} = 30°) were calculated from Eqn. (3) and are tabulated in **Table II-1.**

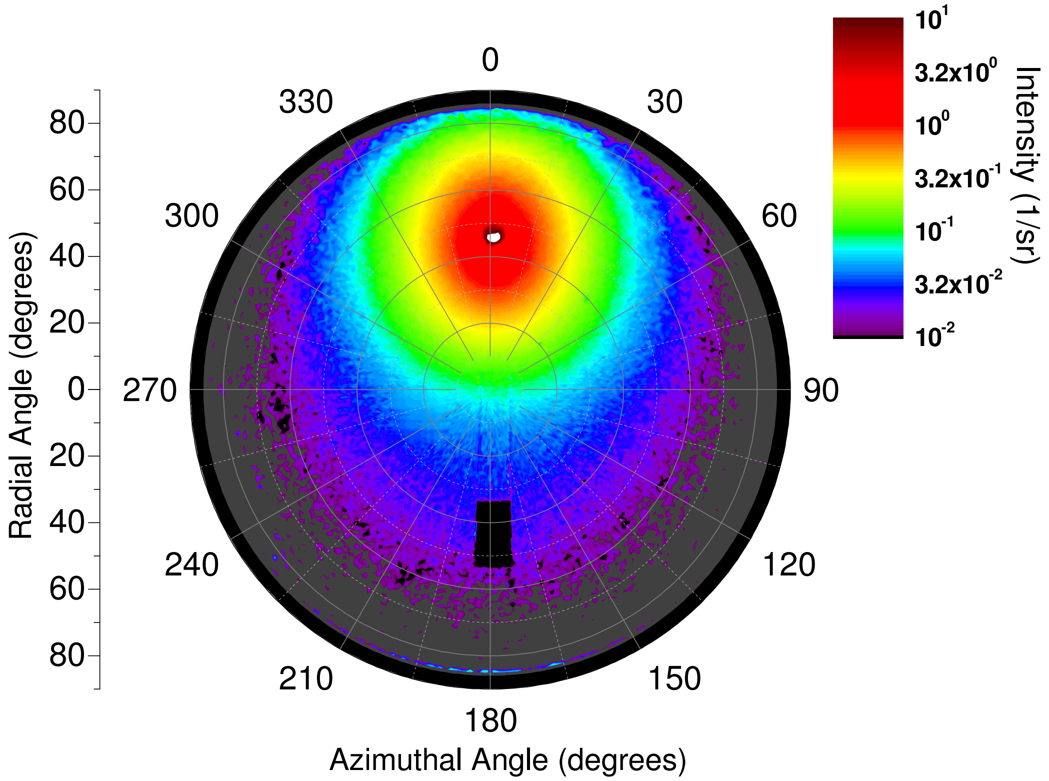

Figure II-6: A spherical contour plot of scattered intensity from Silver #1. Incident light enters from a radial angle of 45° and an azimuthal angle of 180°. The scattered intensity focused around the specular direction and decreases rapidly away from specular.

The scattering profiles obtained for the different paint systems can be used to deduce the distribution of the orientation of the platelets, by re-arranging Eq. (2):

$$\theta_F = 0.5 * [\sin^{-1}({}^{1}\!/_{1.5} \sin \theta_{IN}) - \sin^{-1}({}^{1}\!/_{1.5} \sin \theta_{OUT})], \tag{4}$$

where θ_F is the platelet orientation angle, θ_{OUT} is the flux angle after it exits the clearcoat layer, and $\theta_{IN} = 45^{o}$.

It should be noted that the scattering measurements were made in units of inverse steradians. Therefore, in order to eliminate the effect of the solid angle upon this measured intensity, and to convert the scattered data to values directly proportional to platelet angle area/frequency, the scattering intensities were normalized to that of a perfectly diffuse white scatterer. This normalization results in the relative area of platelets oriented at a particular angle. From the frequency data of these relative areas, CDFs for the orientation of the platelets were calculated. Furthermore, the setup of the scattering measurement resulted in a blind spot at the source of the incident light (at 45^{o} to the normal). As a result, all the calculations for the orientation of the platelets were made from scattered light collected between the direction of the incident light source and the direction of the specular reflection.

The CDFs of the platelet orientations from the different paint systems, as determined by confocal microscopy, are plotted in **Figure II-7a-j.** Superimposed on these plots are the corresponding CDFs predicted from the scattering data**.** Silver #7 was the most oriented system, with a median orientation angle of 3.1 ± 0.2^{o} (based on the LSCM data). Silver #10 was the least oriented system, with a median orientation angle of 7.0 ± 0.4^{o} (based on the LSCM data).

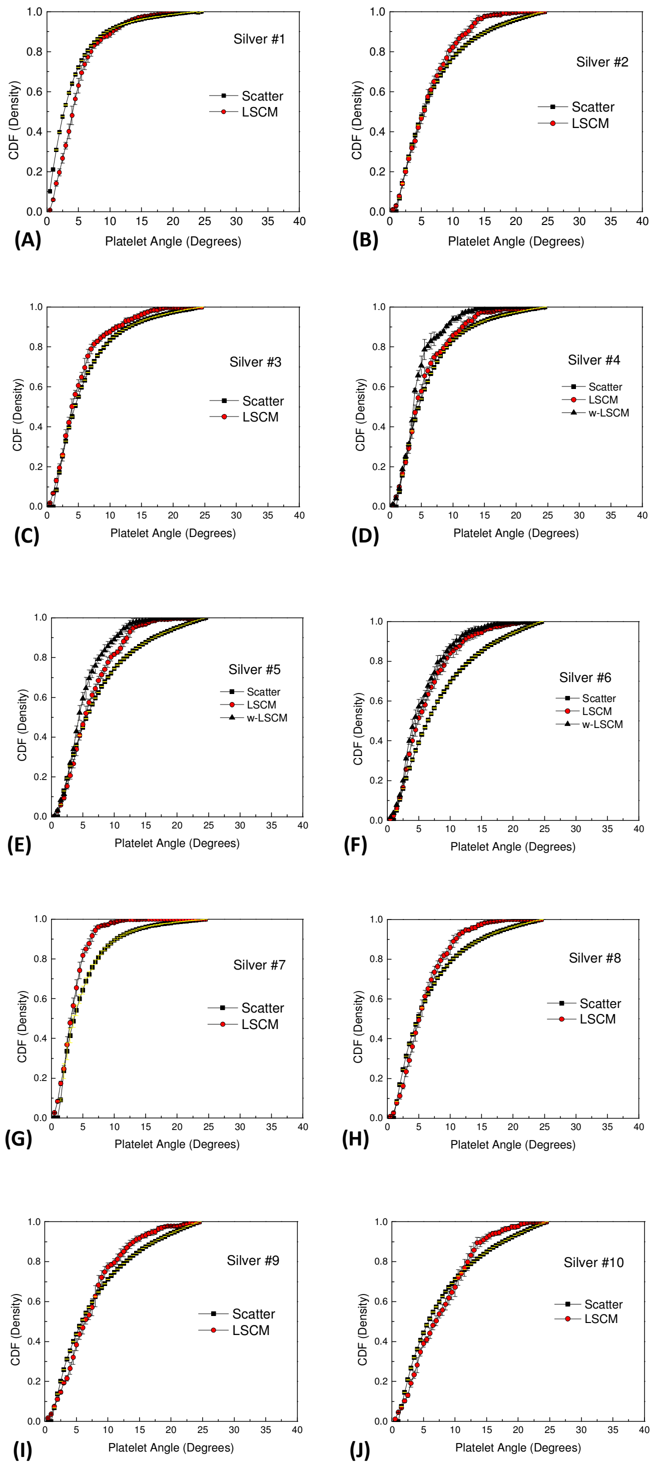

Figure II-7: Comparisons between the distributions of the platelet orientations determined by confocal microscopy experiments (LCSM) and the distributions inferred from the scattering measurements (Scatter). Weighted LSCM profiles, as discussed in the text, have been added to the plots (D) through (F).

Discussion

Relationship between measured and predicted orientations

The strength of the orientation-scattering link between the two measurements can be described by the difference between the orientation curves obtained by the two techniques. Qualitatively, one can see from **Figure II-7** that the orientations obtained from microscopy and from the scattering analyses are similar for Silver #4; they are less so for Silver #6. To quantify the degree of agreement, the root-mean-square (RMS) error between the microscopy and scattering orientation curves was calculated and summed for each sample using the equation

$$RMS_{error} = \sqrt{\sum (X_M - X_S)^2 / n} \tag{5}$$

where X_M and X_S are corresponding points on the orientation curves calculated from the microscopy and scattering measurements, and *n* is the number of points analyzed. The results of this calculation are listed for each sample in **Table II-1.**

To determine if the platelet angles should have been weighted based on the visible area of each platelet, weighted platelet distributions (w-LSCM) were calculated and plotted for Silver #4-Silver #6 in **Figure II-7d-f**. The frequency of the orientation angle for each platelet was scaled by the visible area of the platelet to produce a weighted CDF. The visible area of an individual platelet is the area directly viewable by LSCM and not shadowed by other platelets. Therefore, platelets with large visible areas are expected to have a greater effect on scattering and on lightness than platelets with smaller visible areas. This visible area was measured from LSCM scans, as illustrated in the call-out of **Figure II-3**. As shown in **Figure II-7**, these weighted distributions did not result in a better agreement with the predictions from the scattering distributions.

The strength of the relationship between orientation and scattering is shown to vary as a result of formulations changes (**Figure II-7**). Three effects have been considered to explain the discrepancies between the orientation profiles measured by microscopy and those deduced from scattering measurements. These effects are (i) reflections from the edges of samples, (ii) scattering from rough surfaces, and (iii) multiple reflections between platelets, considered in more detail below.

Edge Reflections

Reflections from the edge of the platelets, as shown schematically in **Figure II-8a**, is one possible reason why there is a discrepancy between the measured and deduced orientations. This type of reflection will be manifested primarily in the backscattered region. An increase in thickness would result in additional reflections from the edges of the platelets. This would affect the interpretation of the scattering data, but would not contribute to the measurements of the orientation distribution from the LSCM experiments. Therefore, the associated RMS_{error} values would be expected to increase for thicker platelets. Furthermore, the two distributions would be expected to be well-matched at small orientation angles, and to deviate only at larger angles (greater than 10^o to 15^o). As shown by the curves of **Figure II-7**, the data do not follow either of these patterns. Therefore, edge reflections do not appear to be the reason for discrepancies between the structure-property relationships.

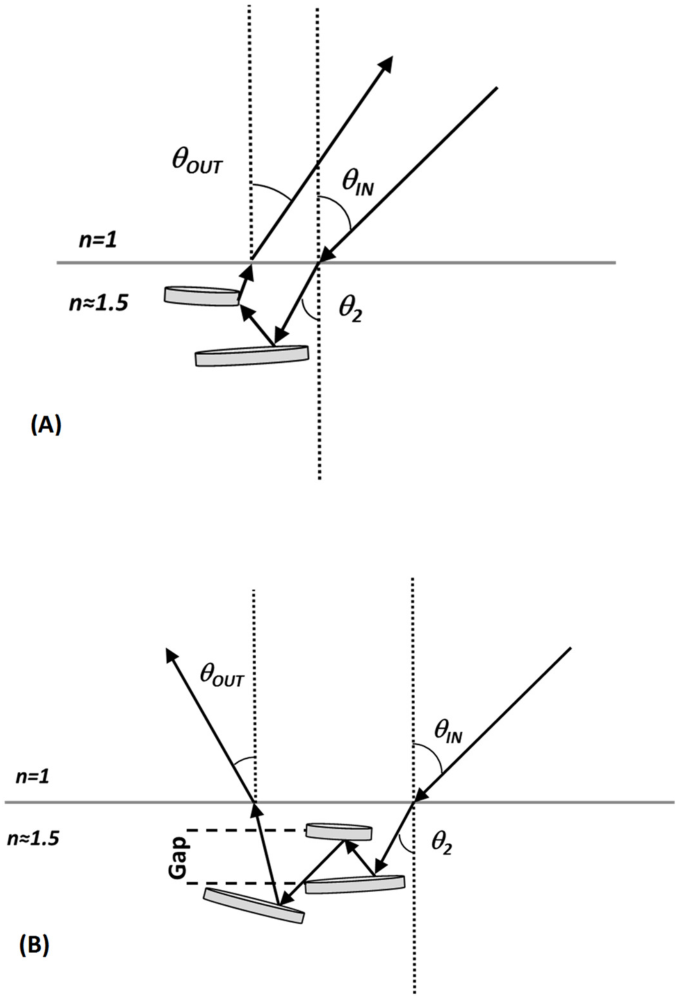

Figure II-8: (A) Schematic illustration of a reflection from the edge of a platelet. (B) Schematic illustration of multiple reflections between platelets. In both cases, one can no longer infer orientation from scattering data, as that inference assumes single reflections off of platelet faces. Edge reflections and multiple reflection events will affect different regions of the scattering profile in different ways. Edge reflections contribute to the backscattered region while multiple reflection events contribute to the forward scattering region.

Surface Roughness

The surface roughness of the platelets is a second possible cause for the discrepancies between the measured and predicted distributions. The surface roughness of the platelets was measured from platelets filtered out of the appropriate basecoats. The liquid paint was dissolved in methylene chloride, and then the mixture was passed through Grade 2 filter paper. A Wyko NT3300 (Bruker Corp., Billerica, MA), non-contacting, white-light interferometer was used to quantify the surface roughness of the platelets that were deposited on the filter paper. The resultant root-mean square roughness was determined to be 51.4 ± 10.0 nm, with no systematic difference being observed between the roughness values of the platelets from different paints.

The Raleigh criterion for the maximum roughness, H, that a surface can have if it is to be considered to be optically smooth is given by [25]

$$H < \frac{\lambda}{8 \sin \beta} \tag{6}$$

where, λ is the wavelength of incident light, and β is the angle of incident light. This limiting value is about 70 to 115 nm for the illumination conditions of the experiments. This is on the order of the root-mean square roughness of the platelets, which was ~51.4 ± 10.0 nm, as discussed above. This indicates that the scattering from a platelet face should be focused in the specular direction, but also may exhibit some broadening of the specular lobe. The exact shape of the reflectance lobe from individual platelets will be reported later in this thesis.

Multiple Reflections

Multiple reflections between the surfaces of platelets are possible if light passes through a space in the top layer of platelets and is subsequently reflected from a deeper platelet to hit the bottom surface of another platelet (**Figure II-8b**). For visible wavelengths, absorption associated with each reflection results in a reduction of the intensity by approximately 8% [26]. These internal reflections will also affect the effective angle of reflection, but numerical simulations would be required to obtain relationships between the angle of incidence and the angle of reflection, since the number of reflections that a particular ray may experience is not known *a priori*. In this section, we address two microstructural features that affect multiple reflections: (i) the height, or gap, between platelets in different layers (**Figure II-8b**), and (ii) the *coverage* - the degree to which platelets are obscured or shadowed by other platelets.

Gap Factor

To determine the effect of gaps upon the scattering behavior, an analysis of the gaps between the platelets was performed using the same LSCM scans that had been employed for measuring the orientations. Line scans provided topographical profiles of the topmost platelets. An example (from Silver #1) is shown in **Figure II-9**.

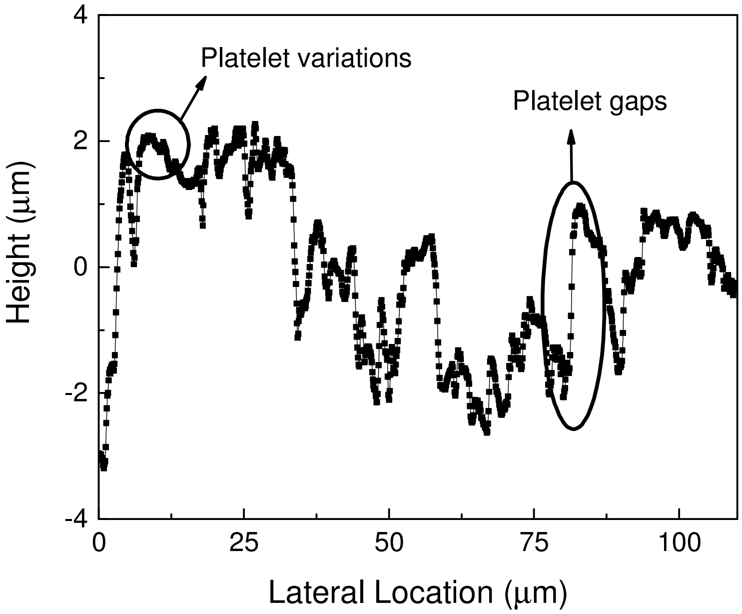

Figure II-9: 2-D line-scan profile taken from the LSCM height map for Silver #1 shown in Figure II-3. Small variations in the height are associated with variations along the surface of a single platelet, while large variations in height are associated with gaps between platelets.

The large height changes are associated with gaps between platelets, while the smaller height differences are associated with local, intra-platelet topographical changes. Small fluctuations in the height were filtered out by calculating the derivative of the height with respect to distance, and eliminating peaks associated with slopes having magnitudes of less than one. The remaining peaks in the derivative profile, which are assumed to be associated with gaps between the platelet upper surfaces, were integrated and summed over the entire profile. The resulting sum is the cumulative gap over the length of the scan. This quantity was normalized by dividing it by the scan length to produce what is termed the “gap factor” for the system. A larger gap factor provides a greater opportunity for light to penetrate below the top layer of platelets, and to undergo multiple reflections, be it off edges or platelets below the surface. The results from ten to twelve line scans were averaged for each of the ten silver paint systems, and the resultant “gap factors” are reported in **Table II-1.**

As shown in **Figure II-10,** a moderate correlation may exist between the gap factor and the RMS_{error}, if the gap factor is greater than about 0.15. The single datum that doesn't seem to fit with the other data is the result from Silver #7. This is a system that was sprayed by hand to complete visible hiding. It exhibited the highest degree of orientation (**Figure II-7g),** and the lowest gap factor out of all the samples tested. For this sample, the scattering must be dominated by primary reflections, since opportunities for multiple reflections are few. Therefore, in this system, broadening of the scattering data is caused primarily by the roughness of the platelets and by reflections from the edges of platelets. On-going work is being done to establish whether this single point indicates a break down in any possible correlation between gap factor and RMS_{error} at low gap factors, or whether it represents a change in the relationship. This study requires the careful preparation of systems with good orientation and low gap factors, which we did not fabricate in this initial study.

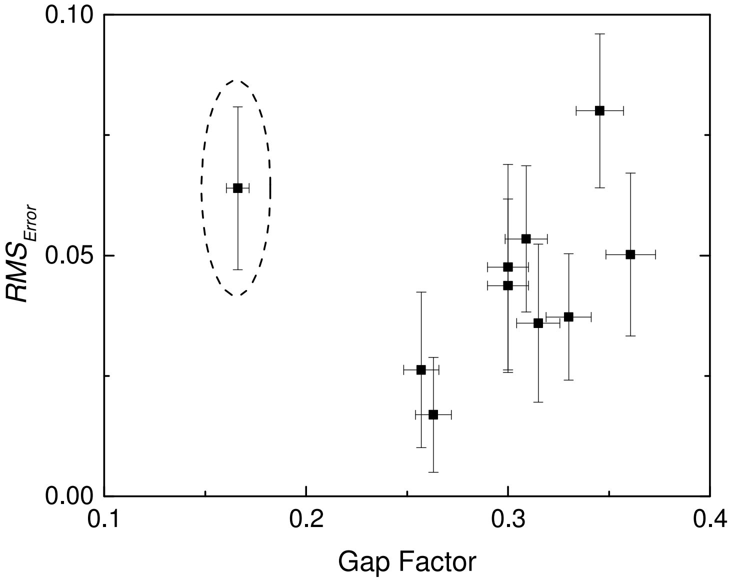

Figure II-10: A plot of the RMS_{error} against the gap factor for all ten samples. The circled datum point is from Sample #7, which was the most oriented sample of the series. On-going work is investigating whether there is any systematic effects on the relationship between the gap factor and the RMS_{error} for highly-oriented systems, or whether these are just a break-down in any apparent correlation.

Figure II-11 shows that when systems with similar orientation profiles are compared, Silver #4 through Silver #6, there appears to be quite a strong linear correlation between the gap factor and the RMS_{error}. This possible connection between orientation distributions and scattering behavior will be explored, later in this thesis, using controlled simulations of these paint systems, in which the effect of each contributing factor can be considered independently.

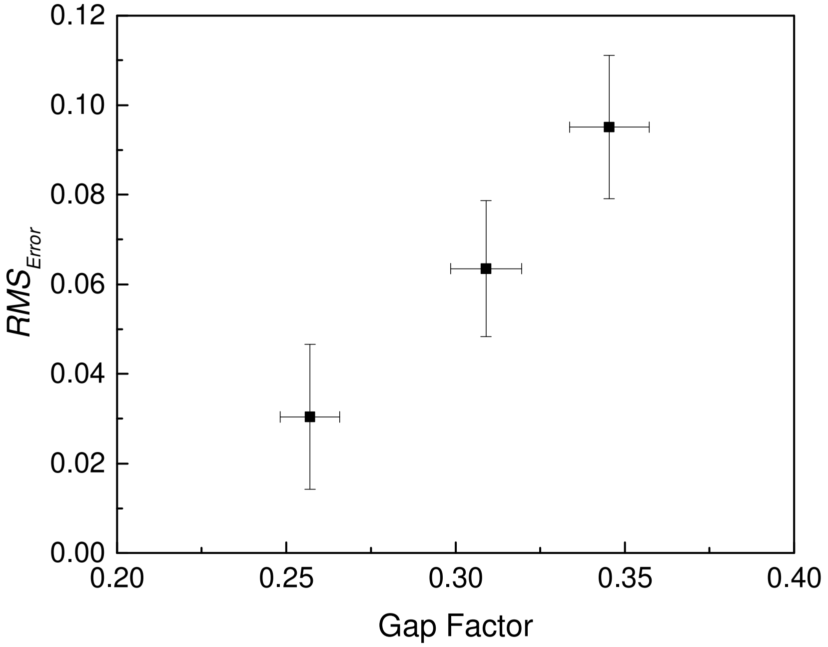

Figure II-11: An apparent correlation between the RMS_{error} and the gap factor for a set of paint systems in which the platelets have similar orientations (Silver #4, Silver #5 and Silver #6).

The three samples identified as Silver #4 through Silver #6 possess very similar platelet orientation distributions (**Figure II-5c**), yet their lightness values at 15° OS are significantly different, as detailed in **Table II-1**. The only significant difference between the three samples is the gap factor. The relationship between the lightness at 15° OS and the gap factor is shown in **Figure II-12** for the three samples. This illustrates that the size of the gaps between the platelets may be an additional microstructural component that contributes to the color of a material. Larger gaps may result in more secondary reflections; the multiple reflections will result in more light being scattered away from the macroscopic specular direction.

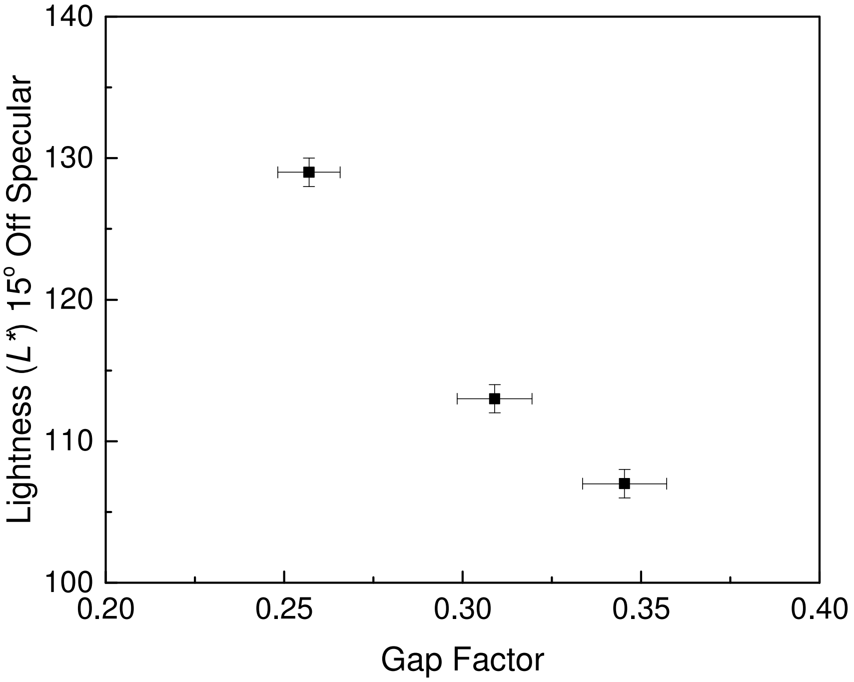

Figure II-12: The correlation between the *L** and gap factor for the samples identified as Silver #4, Silver #5 and Silver #6.

Coverage

Another microstructural feature related to the density of the platelets and the gaps between them is what we will call "fractional coverage" -- the degree to which platelets are obscured or shadowed by other platelets. For example, a platelet that is completely obscured by other platelets is described as exhibiting a fractional coverage of 1.0, while a platelet on the surface of the basecoat layer will have a fractional coverage of 0.0.

To examine the effect of coverage, a pair-correlation microstructural analysis was employed to determine if specific morphologies affected the directional distribution of the scattered light in these systems. The pair-correlation function (also known as the radial-distribution function) is a technique used in statistical mechanics. It describes the density of a system of particles by measuring the distance between particle centers [27–30]. Here, the technique was modified to analyze 2D cross sections, similar to that shown in **Figure I-7** from Chapter I, and it was used to describe the microstructure of the paint systems.

The center of each platelet was identified, and used as a reference point. From that center point, rays were projected towards the surface at 5° increments (**Figure II-13**). The percentage of rays emanating from the center of the upward-facing surface of a platelet that intersect another platelet was defined as the coverage of a platelet, C_v. Conversely, the probability that light entering the system from any direction will have a primary reflection off a platelet is assumed to be given by 1-C_v (ignoring the finite size of the platelets).

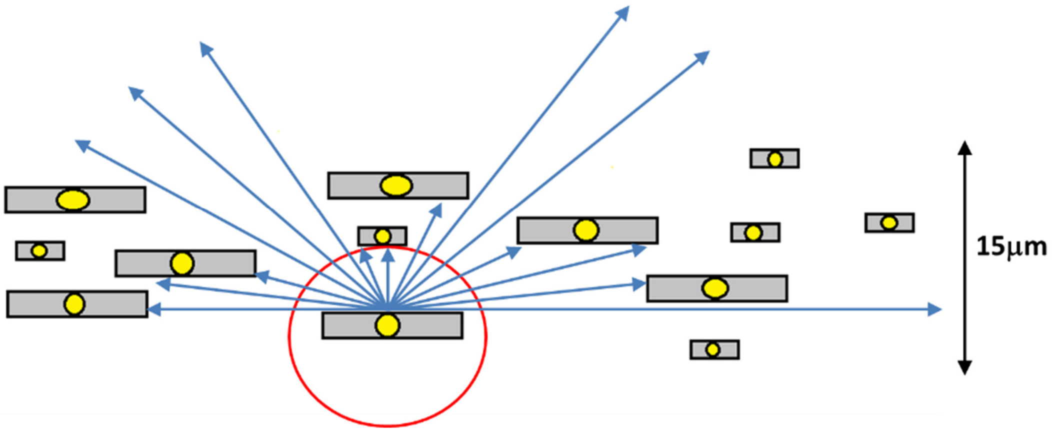

Figure II-13: A schematic illustration of the modified pair-correlation analysis used to analyze the coverage of platelets. In this example, the platelet being considered has a fractional coverage of 0.3.

For a multiple reflection event to occur from a particular platelet, light must reach that platelet, and the reflection must strike a second platelet. The probability of both of these events happening, P_m, for light entering from any direction is

$$P_m = C_V(1 - C_V), \tag{7}$$

This probability has a maximum of 0.25 when C_v is equal to 0.5. So, platelets with a fractional coverage of between 0.25 and 0.75 are the most likely to cause multiple reflections.

The form of Eqn. (7) implies that if a composite paint system is illuminated across all angles (diffuse illumination), a quick transition from platelets with zero coverage to complete coverage as a function of depth will result in a lower incidence of multiple reflections. To examine this prediction, the coverage values for about 30 platelets from each of the Silver #4 and Silver #6 samples are plotted in **Figure II-14** as a function of the depth below the surface. Both of these systems show a transition from platelets with a fractional coverage of 0.0 to a fractional coverage of 1.0 with depth. However, Silver #6, which had larger platelets, had a larger percentage of platelets with a fractional coverage in the range of 0.25-0.75. This suggests that if both of these systems were illuminated by diffuse light, Silver #6 would likely have a reduced lightness compared to Silver #4. A visual qualitative comparison between the two samples under diffuse illumination confirmed this behavior.

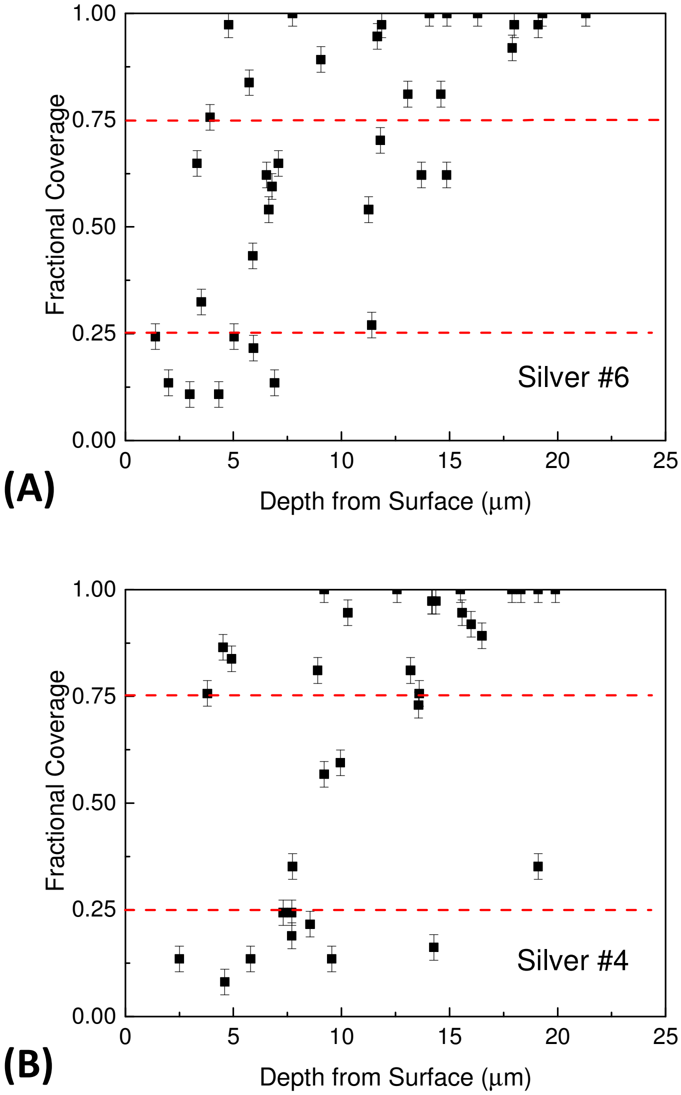

Figure II-14: Plot of the coverage for individual platelets as a function of depth below the surface for (A) Silver #6, with a median platelet diameter of 11.5 μm, and (B) Silver #4, with a median platelet diameter of 25 μm. The system with the smaller platelets has more platelets with a fractional coverage between 0.25 and 0.75 than the other system. It is postulated that this is associated with a higher incidence of multiple reflections, which resulted in a reduced lightness observed in a diffuse illumination environment for Silver #6.

As a final comment, it is noted that a strict relationship between the fractional coverage of the platelets and the measured appearance of a paint system, which is usually conducted with light incident at 45° to the surface, can only be made when the fractional coverage is computed for light incident at that same angle. We expect this fractional coverage to differ from the omni-directional fractional coverage due to path length complications and projected area differences at very shallow angles in the omni-directional case. However, it is noted that the data in **Table II-1** confirm that the measured lightness (*L**) at 15° OS was lower for Silver #6, than for Silver #4. This is consistent with the qualitative observations made under diffuse light.

Summary and Conclusions

In this study we confirm that platelet orientation is the major microstructural property of platelet/polymer paint systems that affects visual appearance across a range of formulations. Other microstructural properties, in addition to orientation, were found to significantly affect appearance through multiple reflection events. Multiple reflections are related to additional microstructural parameters associated with the density and spacing of the platelets, such as the size and frequency of the gaps between the platelets, and the coverage of platelets by other platelets. The relationship between platelet gaps and appearance has not been reported on previously and is of value to both color designers and digital renderers. Because platelet gaps and multiple reflections significantly affect appearance, their inclusion in predictive models or digital rendering software is necessary to insure accurate results.

Digital rendering tools that do not incorporate both primary and secondary scattering events from platelet-containing materials risk overestimating the amount of near-specular scattered light. Other applications such as devices that utilize tiny mirrors such as a digital micro-mirror devices (DMD) [31], where individual mirrors can be addressed and assigned an orientation to produce macroscopic images may benefit from a clearer understand of the link between microstructure and light scattering as well. This link cannot be limited to surface microstructure and must incorporate the entire 3D microstructure of the scattering layer to create a model or simulation based on the structure-property relationship of the scattering system.

References

1. Medina JM, Díaz JA (2013) Characterization of reflectance variability in the industrial paint application of automotive metallic coatings by using principal component analysis. Optical Engineering 52:051202.
2. Seo MK, Kim KY, Kim DB, Lee KH (2011) Efficient representation of bidirectional reflectance distribution functions for metallic paints considering manufacturing parameters. Optical Engineering 50:013603.
3. Ershov S, Kolchin K, Myszkowski K (2001) Rendering Pearlescent Appearance Based On Paint ‐ Composition Modelling. EUROGRAPHICS 2001 20:227-238.
4. Germer TA, Nadal ME (2001) Modeling the appearance of special effect pigment coatings. International Symposium on Optical Science and Technology 1:77-86.
5. Cook RL, Torrance KE (1982) A reflectance model for computer graphics. ACM Transactions on Graphics (TOG) 1:7-24.
6. Weidlich A, Wilkie A (2007) Arbitrarily layered micro-facet surfaces. Proceedings of the 5th international conference on Computer graphics and interactive techniques in Australia and Southeast Asia. ACM 1:171-178.
7. Rump M, Müller G, Sarlette R, Koch D, Klein R (2008) Photo-realistic Rendering of Metallic Car Paint from Image Based Measurements. Computer Graphics Forum 27:527-536.
8. Germer TA, Marx E (2004) Ray model of light scattering by flake pigments or rough surfaces with smooth transparent coatings. Appl Opt 43:1266-1274.
9. Sung L, Nadal ME, McKnight ME, Marx E, Laurenti B (2002) Optical reflectance of metallic coatings: effect of aluminum flake orientation. J Coatings Technol 74:55-63.
10. Kettler W, Richter G (1997) Investigation on topology of platelet-like effect-pigments in automotive surface-coatings. Progress in organic coatings 31:297-306.
11. Klein GA, Meyrath T (2010) Industrial color physics. Springer, New York.
12. Maile FJ, Pfaff G, Reynders P (2005) Effect pigments—past, present and future. Progress in Organic Coatings 54:150-163.
13. Tachi K, Okuda C, Suzuki S (1990) Mechanism of aluminum flake orientation in metallic topcoats. Journal of coatings technology 62:43-50.
14. Thouless M, Dalgleish B, Evans A (1988) Determining the shape of cylindrical second phases by two-dimensional sectioning. Materials Science and Engineering: A 102:57-68.
15. Bandyopadhyay J, Malwela T, Ray SS (2012) Study of change in dispersion and orientation of clay platelets in a polymer nanocomposite during tensile test by variostage small-angle X-ray scattering. Polymer 53:1747-1759.
16. Yang C, Smyrl W, Cussler E (2004) Flake alignment in composite coatings. J Membr Sci 231:1-12.
17. Pelicon P, Klanjšek-Gunde M, Kunaver M, Simcic J, Budnar M (2002) Analysis of metallic pigments by ion microbeam. Nuclear Instruments and Methods in Physics Research Section B: Beam Interactions with Materials and Atoms 190:370-374.

18. Gunde MK, Kunaver M, Mozetic M, Pelicon P, Simcic J, Budnar M, Bele M (2002) Microstructure analysis of metal-effect coatings. Surface Coatings International Part B: Coatings Transactions 85:115-121.
19. Kirchner E, Houweling J (2009) Measuring flake orientation for metallic coatings. Progress in organic coatings 64:287-293.
20. Kasarova SN, Sultanova NG, Ivanov CD, Nikolov ID (2007) Analysis of the dispersion of optical plastic materials. Optical Materials 29:1481-1490.
21. Pauli H (1976) Proposed extension of the CIE recommendation on "Uniform color spaces, color difference equations, and metric color terms". JOSA 66:866-867.
22. Streitberger HJ, Kreis W, Decher G Schlenoff JB (2005) Automotive paints and coatings. VCH Verlag GmbH & Co. KGaA, Weinheim, FRG.
23. Di Domenico J, Henshaw P (2012) The effects of basecoat bell application parameters on elements of appearance for an automotive coatings process. Journal of Coatings Technology and Research 9:675-686.
24. Ellwood KR, Tardiff JL, Alaie SM (2014) A simplified analysis method for correlating rotary atomizer performance on droplet size and coating appearance. Journal of Coatings Technology and Research 11:303-309.
25. Beckmann P, Spizzichino A (1987) The scattering of electromagnetic waves from rough surfaces. Artech House, Inc., Norwood.
26. Bartl J, Baranek M (2004) Emissivity of aluminum and its importance for radiometric measurement. Measurement of Physical Quantities 43:31-36.
27. De Podesta M (2002) Understanding the properties of matter. CRC Press, Boca Raton.
28. Waisman E (1973) The radial distribution function for a fluid of hard spheres at high densities: mean spherical integral equation approach. Molecular Physics 25:45-48.
29. Yuste SB, Santos A (1991) Radial distribution function for hard spheres. Physical Review A 43:5418-5423.
30. Kincaid J, Weis J (1977) Radial distribution function of a hard-sphere solid. Mol Phys 34:931-938.
31. Younse JM (1993) Mirrors on a chip. Spectrum, IEEE 30:27-31.

CHAPTER III

The Creation and Use of a Hybrid Ray-Wave Optics Model to Study the Effect of Platelet Surface Roughness on the Scattering Behavior of Silver Metallic Paint Systems

Introduction

It is important for industries that manufacture consumer products to not only understand how customers perceive color, but also how specific colors are physically produced. The design and manufacturing processes could be accelerated and enhanced substantially by an ability to predict the appearance of color prior to part production. Ideally, designers and engineers could use such a method to visualize a range of color or to assess the risk of unacceptable color harmony on objects painted with highly gonioapparent coatings. Often, large changes in appearance are mistaken for poor color harmony (match) on geometrically complex objects. A method developed for this task would need to accurately simulate real, physical materials to be of value.

While significant progress has been made to accurately render colors based on complete or partial BRDF scans, predictive modeling of colors from material and microstructural data lags in development. Attempts have been made to predict the appearance of paint systems from the scattering behavior of individual layers [1–3], combining the measured scattering behavior of the layers and/or scatterers into a single bulk scatterer. To simulate the scattering behavior of metallic paint systems, researchers also have utilized microfacet models [2,4,5], which assume a single layer of connected faces oriented to produce the BRDF of the gonioapparent systems. However, none of these techniques incorporated the complete 3D microstructure of the platelet layer, or the surface roughness of the platelets/facets.

The generation of a complete 3D microstructure would improve our ability to predict the scattering behavior of a layered platelet containing paint system. An assumption of specularly reflecting platelets, however, would limit the accuracy of a pure ray-based model. While a great deal of work has been conducted on the scattering of radiation and light from metallic surfaces [6–12], no work has been done to examine how a layered microstructure of rough scatterers affects the gonioapparent behavior of platelet-containing coatings. Nor has such a model ever been created for predictive appearance modeling.

Scattering of light from a rough metal surface

The first attribute that must be included in a complete 3D model of a silver metallic paint system is the scattering of light from individual platelets. The BRDF of a solid metal is directly affected by the roughness of the metal's surface [6, 8–12]. While the simplest way to quantify these effects is to measure the BRDF of the metal in question, sometimes it is not possible to conduct a physical measurement due to size and time limitations, the lack of a physical sample, or the delicateness of any physical sample that is possessed. In these cases, reflection models have been proposed by a number of researchers to predict the BRDF of a roughened metallic surface [13–20]. These models are based on two key surface roughness parameters, the RMS roughness (σ_{RMS}) and the surface correlation length (τ). RMS roughness represents the standard deviation of the distribution of surface heights from the surface mean and is calculated in two dimensions using the following equation:

$$\sigma_{RMS} = \sqrt{\frac{1}{n}\sum_{i=1}^{n} {y_i}^2} \tag{1}$$

where y_i are the vertical distances from the mean line for each data point. A large σ_{RMS} indicates large deviations from the mean and a rougher surface. The surface correlation length represents the uniformity of height over finite distances along the surface. It is a measurement of the distance over which the autocorrelation function, which is the cross-correlation of a signal with itself, drops below $1/e \sim 0.368$. Surfaces with slow, gradual changes in surface texture possess a large value of τ, while sharp, large slopes in surface roughness have small values of τ.

The magnitude of σ_{RMS} and τ compared to the wavelength of light (λ), and each other, dictates which scattering model most accurately represents the interaction of light with a roughened surface [21]. Based on the roughness of the surface and the wavelength of the incident light, three different approaches can be taken to quantify the scattering from surfaces: the specular approximation, the geometric optics approximation, and electromagnetic (EM) theory. The schematic, shown in **Figure III-1**, is based on data presented by Tang and illustrates the regions of validity for each of these approximations [21].

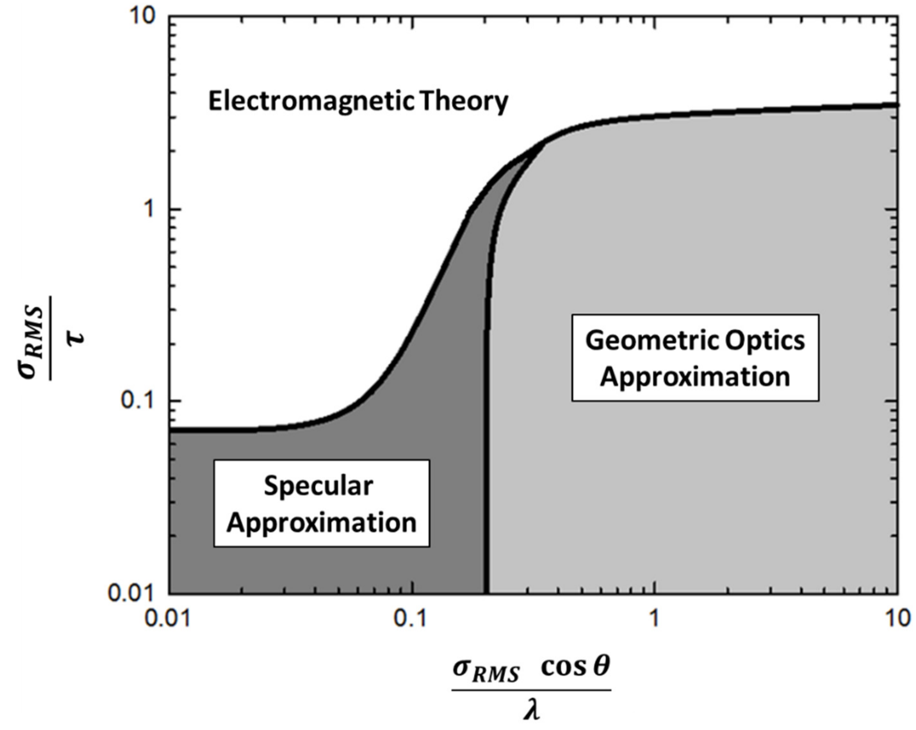

Figure III-1: Plot of $\frac{\sigma_{RMS}}{\tau}$ as a function of $\frac{\sigma_{RMS}\cos\theta}{\lambda}$ across different regions of validity for scattering models. Plot based on data presented by Tang [21].

The specular approximation is the simplest reflection model, with the surface treated as a perfect mirror. This approximation is most accurate when the wavelength of light is large compared to σ_{RMS}, and the magnitude of σ_{RMS}/τ is significantly less than unity [21,22], with many models making this approximation to minimize computational complexity. We will determine if the platelets contained within typical silver metallic paints are smooth enough to be considered a purely specular reflector.

The specular approximation cannot be used when σ_{RMS} approaches the wavelength of the incident light. In this case, geometric optics, which treats radiation as rays and tracks the energy of the rays as they interact with roughened surface, can be used to approximate the scattering behavior of the roughened surface if σ_{RMS}/τ is ≤ 1 [21,23,24]. Many of the reflection models utilized in computer graphics are based on geometrical optics due to their computational simplicity, including Torrance-Sparrow and Cook-Torrance models based on geometric optics [14,25]. Sometimes rendering artists use these models outside of their region of validity because they provide a reasonably accurate, if not exact, "look" to the material.

For quantitatively accurate prediction, one can integrate Maxwell's equations for a roughened surface, regardless of σ_{RMS}, τ, angle of incidence (θ), and λ. Until recently, this has not been possible due to computational limitations. As a result, models were previously proposed to predict the scattering behavior of roughened surfaces that fell outside of the geometric and specular approximation regions [13,20,26–30]. To reduce complexity, these models employ approximations based on the values of σ_{RMS}, θ, λ, and τ. The two most common approximations utilized in these E-M models are the Kirchhoff approximation and the small perturbation approximation [22,31]. The former assumes the E-M field at any point of the surface is equal to the field that would be present on the tangent plane at that point [22]. The latter is an expansion of the scattering amplitude with respect to the small height parameter [32]. The validity of these two approximations have been examined by previous authors, who found that their validity depends on θ and τ specifically [33–36]. Considered to be one of the most accurate reflection models for computer graphics, the He-Torrance model utilizes the Kirchoff approximation with added shadowing and geometric components [13]. However, due to its computational complexity, it is avoided for real –time rendering in favor of simpler, computationally less intensive models.

For the purposes of this study, real-time rendering is not needed, making the integration and solution of Maxwell's equations for a particular scattering surface more feasible. Until recently this integration was computationally expensive for even simple static surfaces, but new finite element analysis (FEA) simulation tools and improved computer hardware have made it possible to predict the scattering of rough surfaces and compare their results to those obtained from the previously discussed approximation methods [37–39]. Isakson modeled scattering behavior of the ocean floor and found that the FEA method produced similar results to the Kirchoff and small perturbation approximations in their regions of validity, and matched the exact integral solution in all cases [40]. This shows that it may be possible to use FEA simulations to model and systematically study the effect of surface roughness on the scattering behavior of the individual platelets and predict the lightness of the entire paint system.

Digital Modeling of Hypothetical Paint Systems

As mentioned, a range of models have been put forth to simulate and predict the appearance of a platelet-containing paint system. While these models can predict the "look" of gonioapparent colors, in general they have so far ignored the effects of platelet microstructure on the appearance of platelet-containing paint systems. To address this limitation in modeling capability, we use ray tracing or casting to assess the interaction of light with the entire microstructure. This simulation approach is used in both optics and graphics to quantify the geometric interaction of discrete light rays with simulated objects and surfaces [41]. For multilayered platelet-containing paint systems, ray tracing allows us to quantify the scattering effects of the complete 3D microstructure by accounting for each ray's multiple reflection events, as well as both edge and face reflections. Geometric ray tracing is valid where diffraction or interference effects are minimal, or when a hybrid approach [42] can be utilized to incorporate wave optics effects into the scattering profile of a simulated object. It is this hybrid ray-wave approach that we feel can be used to accurately predict the scattering and lightness behavior of these metallic coatings.

In this chapter, we attempted to create an accurate hybrid ray-wave predictive model to simulate the scattering behavior of a metallic paint system. First, a finite-element analysis (FEA) simulation was used to solve the electromagnetic interaction of light with individual platelets of varying surface roughness. Platelet roughness values used in the simulation were obtained by measuring the surface roughness of aluminum platelets extracted from liquid paint. Arbitrary rough surfaces were also generated mathematically to assess the sensitivity of the platelets' scattering pattern to σ_{RMS} and τ. These results were compared to current reflection models to qualitatively assess the FEA model against currently accepted reflection models. Finally, a hybrid ray-wave model was created from a complete 3D platelet microstructure that incorporated all the physical properties of the platelets that were used in the physical samples (width, thickness, orientation, and BRDF). The scattering results from individual platelets were incorporated into ray-trace simulations of the complete paint system not only to predict the lightness of physical samples, but also to quantify how platelet roughness affects the scattering and lightness behavior of the complete layered system.

Experimental

Paint materials and application

All samples used to generate and validate the model used in this study comprised a standard silver metallic automotive basecoat/clearcoat. The pigment volume concentration (*PVC*) of each sample was 20% ± 1%. The paint system was sprayed to hiding [43] with a rotary bell applicator onto steel panels that had been previously coated with a grey automotive primer. A low fluid flow and high fluid flow bell application process was used to produce the two physical samples, one with highly oriented platelets (Silver #1) and one with less oriented platelets (Silver #2) respectively. The cured target thickness of the basecoat layer was 20 µm. The clearcoat layer was applied with a cured target thickness of 50 µm and flash dried at ambient conditions to allow for solvent evaporation. The samples were cured in a convection oven for 20 minutes at 130^{o}C.

Platelet extraction and optical profilometry

The surface topography of the aluminum platelets used in the physical samples was characterized using a Wyko NT3300 (Bruker Corp., Billerica, MA), non-contacting, white-light interferometer. A portion of wet basecoat was diluted with methylene chloride and vacuum filtered through Grade 2 filter paper. This created a flattened layer of aluminum platelets on the surface of the filter paper. After the initial filtration step, additional methylene chloride was sprayed onto the filtered platelets to insure any residual acrylic binder was removed from the platelet surface. The surface roughness of isolated, individual platelets was measured and averaged to estimate the platelet population's mean surface roughness parameters σ_{RMS} and τ.

Generation of random rough surfaces based on σ_{RMS} and τ

A complete range of rough surfaces was simulated using the measured surface roughness parameters. A series of Gaussian random rough surfaces based on desired values of σ_{RMS} and τ was created within MATLAB (MathWorks, Natick, MA, USA) using code based on work by Bergström and Garcia & Stoll [44,45]. A 3-D surface texture with *x* & *y* dimensions of 20 μm (250 points) was generated based on the prescribed values of σ_{RMS} and τ. Four unique series of surface textures were generated to identify how changes to either σ_{RMS} or τ impact the BRDF of the platelet and the lightness values of the complete paint system. The values of σ_{RMS} and τ used for surface generation are listed in **Table III-1**.

Table III-1: Surface roughness parameters used to create Gaussian rough surfaces. Four series of surfaces were created to determine the impact of σ_{RMS} and τ on the BRDF of the surface.

Series Number	**σ_{RMS} (nm)**	**τ (nm)**
1	***25***	680
1	***50***	680
1	***100***	680
1	***200***	680
1	***500***	680
1	***1000***	680
2	***15***	120
2	***50***	120
2	***500***	120
3	50	***120***
3	50	***280***
3	50	***520***
3	50	***680***
3	50	***870***
3	50	***1560***
4	500	***120***
4	500	***200***
4	500	***440***
4	500	***680***
4	500	***880***
4	500	***1440***

FEA surface scattering simulations

The effect of surface roughness on the BRDF of the aluminum platelets was quantified using FEA software (Comsol Multiphysics Comsol, Inc., Burlington, MA). To reduce computational complexity, scattering simulations were created in two dimensions. A schematic of the simulation geometry is shown in **Figure III-2**. It was assumed that the surface texture of the platelets was isotropic in the x-y direction, which allowed the 2-D assumption to be made. A 2D surface profile of the roughened aluminum (20 μm in length) was imported from the optical profilometry measurements. The aluminum was assigned an impedance boundary condition because its skin depth at visible wavelengths is very small (~3 nm). Skin depth is a measure of how deeply into a material electromagnetic waves penetrate [46]. Skin depth is dependent on material properties and the frequency of the incident radiation. Most metals have a very small skin depth at visible wavelengths [47].

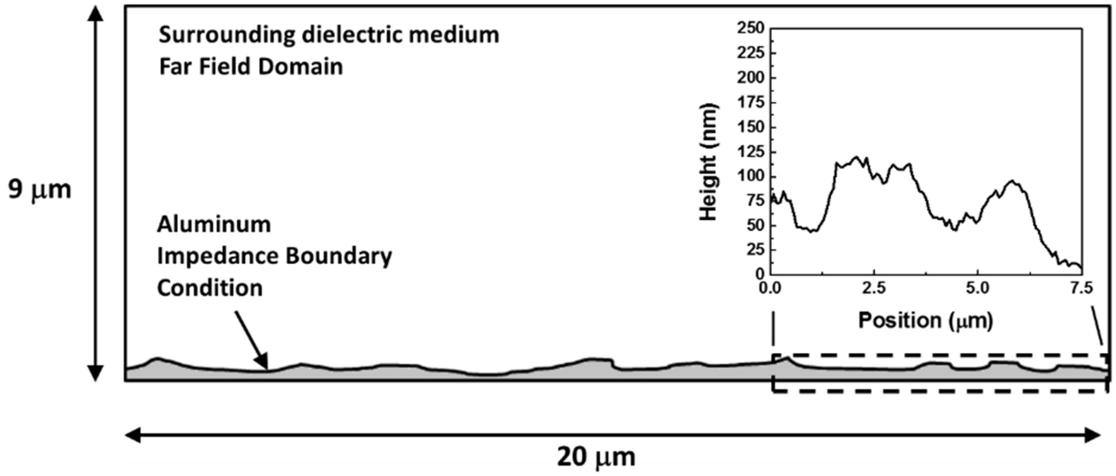

Figure III-2: FEA simulation setup consisting of an aluminum substrate and surrounding dielectric medium. An impedance boundary condition was used for the surface of the aluminum due to the small skin depth and to reduce the simulation size. The 2D line scan obtained from the optical profilometry was imported and used to create the aluminum boundary. The callout is a plot of an actual 2D line scan from a platelet from Silver #1.

Above the aluminum surface was a dielectric medium with a height of 9 μm, with an index of refraction *n* = 1.5 [48], which is the approximate IOR of an acrylic resin. The three outer boundaries of the dielectric region were designated as scattering boundary conditions. A scattering boundary is perfectly transparent to scattered waves. This dielectric region was also designated as the far field domain to capture the shape of the far field scattering pattern.

The background electric field present in this dielectric region and incident upon the roughened aluminum surface had a wavelength of 500 nm. Two incident angles were used for simulation purposes, 0^o and 28^o from normal. A perfectly normal angle of incidence provided a symmetric view of the scattering lobe. To simulate standard colorimetric testing, an incident angle of ~28^o was also used. This angle of incidence occurs when light emitted by a spectrophotometer, used for color tests (45^o from normal), is refracted by the clearcoat layer.

A schematic of this is shown in **Figure III-3.** Both the 0^o and the 28^o far field scatting patterns were used in the approximation of the platelet BRDF.

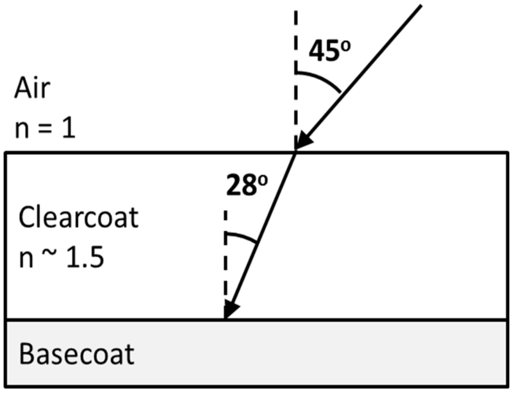

Figure III-3: Schematic of the refraction of a ray of light entering a standard basecoat/clearcoat paint system from 45^o. The index of refraction of the clearcoat is ~1.5, which results in an angle of incidence of ~28^o.

Creation of a simplified ray-based simulation model of a silver metallic paint system

To fully capture the complete microstructure of an aluminum platelet containing silver metallic paint systems, a 3D platelet array was created *in silico*. This array incorporated not only the platelets at the surface (i.e.-microfacet model) of the basecoat layer, but also the platelets contained throughout the basecoat thickness. The platelets also possess a thickness and orientation distribution based on measurements taken from physical samples in our previous study [49]. The creation of this complete, 3D microstructure should improve the accuracy of simulations of lightness and appearance changes that result from formulation/microstructural differences. The ray-trace simulation was conducted within a commercial ray-optics software package (TracePro, Lambda Research Corp, Littleton, MA, USA).

Creation of platelet array using width, thickness, PVC, and orientation parameters

Platelets were assigned dimensional and orientation properties similar to those found in physical systems. These 3-dimensional scatterers were each assigned a width and thickness, as well as an angular rotation about the *x*-, *y*-, and/or *z*-axis. A diagram of the platelet is shown in **Figure III-4**. The platelets were also centered on a designated *x*-, *y*-, *z*-coordinate and assigned a BRDF that was identical across all of the scatterers and their respective surfaces. The BRDF of each platelet surface could be set as desired, whether it was purely specular or more diffuse, based on the roughness of the platelets. Attenuation due to reflections from individual aluminum platelets was fixed at ~8%, based on the visible wavelength of light used in the simulation [50].

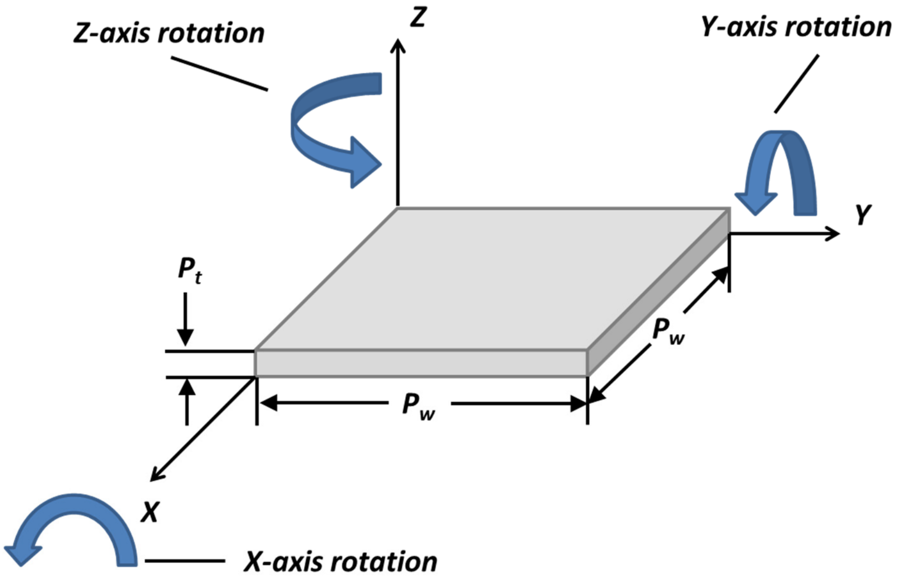

Figure III-4: Schematic of the defined properties and rotations of each simulated platelet. X-axis rotation is based on measured platelet orientation data fitted to a gamma distribution. Z-axis rotation is random. Platelet width (P_w) and thickness (P_t) are conditions of the simulated formulation under study.

Typical dimensional values and orientations for standard aluminum platelets were assigned to these scatterers to simulate aluminum platelets within the basecoat. A platelet width, thickness, *PVC,* and orientation distribution based on those measured from actual physical samples was used to generate each platelet's physical properties [49]; see **Appendix III-A** for details. The best fit for the measured orientation distribution was found to be a 2-parameter gamma distribution (shape; scale). The shape and scale parameters that best fit the orientation profile of Silver #1 were 2.29 and 2.18, respectively. Silver #2 had shape and scale parameters of 2.98 and 2.10 respectively. These distributions were used to assign an x-axis rotation to each of the simulated platelets.

Two additional assumptions were made in creating the simulated platelet array: 1) each platelet is randomly rotated about the *z*-axis [49], and 2) platelets are randomly distributed within the volume of the platelet-containing layer, with no preferential layering or structure formed during application and cure [51]. A schematic showing the progression of these changes to the platelet microstructure is shown in **Figure III-5**.

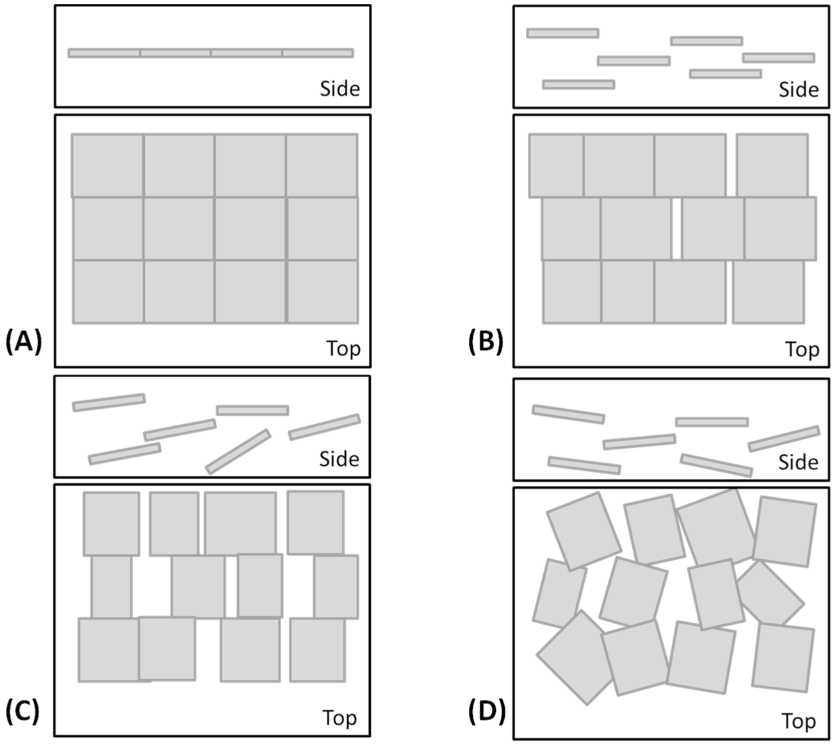

Figure III-5: Schematic of the progression of platelet placement and rotation within layer volume. (A) Single layer of platelets; (B) Platelets randomly distributed in *z*-direction; (C) Platelets rotates about the *x*-axis in the same direction; (D) Platelets randomly rotated about the *z*-axis.

Placement of the platelets within simulated layer to prevent piercings

Platelets were placed within the final paint microstructure by first randomly assigning each platelet *x*-, *y*-, and *z*-coordinates within the designated platelet layer volume as the center point, followed by defining the platelet volume, from which multiple platelets were found to occupy the same physical space. A piercing check algorithm based on an intersecting triangle algorithm developed by Moller [52] was implemented to minimize this issue, with some modifications. The geometry of each platelet was incorporated into the algorithm with the mid-plane of each platelet subdivided into four triangular regions. An example of two platelets divided into triangular regions is shown in **Figure III-6**. The mid-plane was selected to reduce the number of surfaces checked for intersection, reducing computing cost. Triangles in spatially close platelets were then checked for intersection. Platelets with intersections (as shown in **Figure III-6**) were assigned a new location, while maintaining its previously generated orientation, width, and thickness. This replacement continued until either no intersection was detected or 1000 failures (to reduce computational time) resulted. Note that there could still be piercings at the true simulated platelet surfaces that were offset from the midplane. However, the offset distance was small enough to allow the assumption that the number of missed intersections was small, producing a negligible effect. The series of code used for the platelet generation, placement, and pierce checking is shown in **Appendix III-B**.

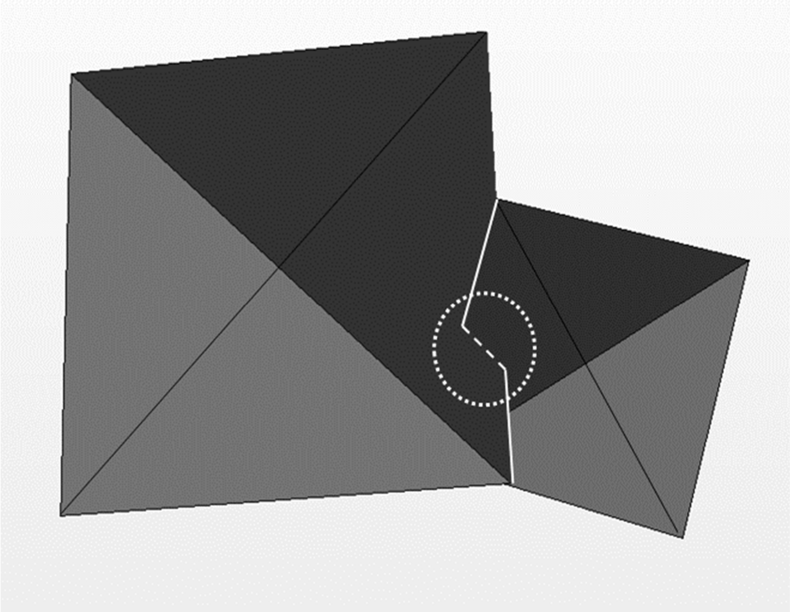

Figure III-6: Schematic of two platelet mid-planes divided into four triangular regions. Each triangular region is checked to insure no pierced faces exist. If a pierced face is detected, the platelet is relocated within the platelet layer volume. A pierced location is circled with a dotted line.

Platelet array creation for incorporation into ray based simulation

Using the approach described above, a platelet array of 15 x 20 mm was created, its size designed to exceed the illuminated area. Once built, the platelet array was imported into the ray-tracing environment and surrounded by a volume of material with an *n*=1.5, a generally accepted value for the binder used in automotive basecoats and clearcoats [53]. A platelet-free clearcoat region was layered over the simulated basecoat with no unique optical interface between the two layers. The lack of an optical interface results from the automotive industry standard practice of wet-on-wet application of the basecoat and clearcoat layers, where intermixing between the layers occurs during application and cure.

BRDF generation and ray trace simulation of metallic paint system

The scattering data obtained from the FEA simulations was imported into a commercial ray optics software package (TracePro, Lambda Research Corp, Littleton, MA, USA) and converted into surface BRDFs. The conversion process assumed scattering was symmetrical about the scattering plane and linearly interpolated any scattering data at angles of incidence between 0^o and 28^o. Rays with angles of incidence greater than 28^o were assumed to have a reflection lobe equal to that of the 28^o angle of incidence lobe, but focused at the appropriate specular reflection angle. The calculated BRDF was applied to each platelet surface within a ray trace simulation. The platelet orientation, width, and thickness for the two physical samples under study--Silver #1 and Silver #2--were based on physically measured data presented in our previous orientation studies [49].

To simulate the gonioapparent behavior of the generated platelet array, a virtual goniospectrophotometer was created (**Figure III-7A**), comprising a circular, collimated light source with radius of 6 mm, and a spherical shell placed around the simulated geometry to capture all of the scattered light. The generated scattering data was used to quantify the lightness of the material as a function of the illumination and observation angles.

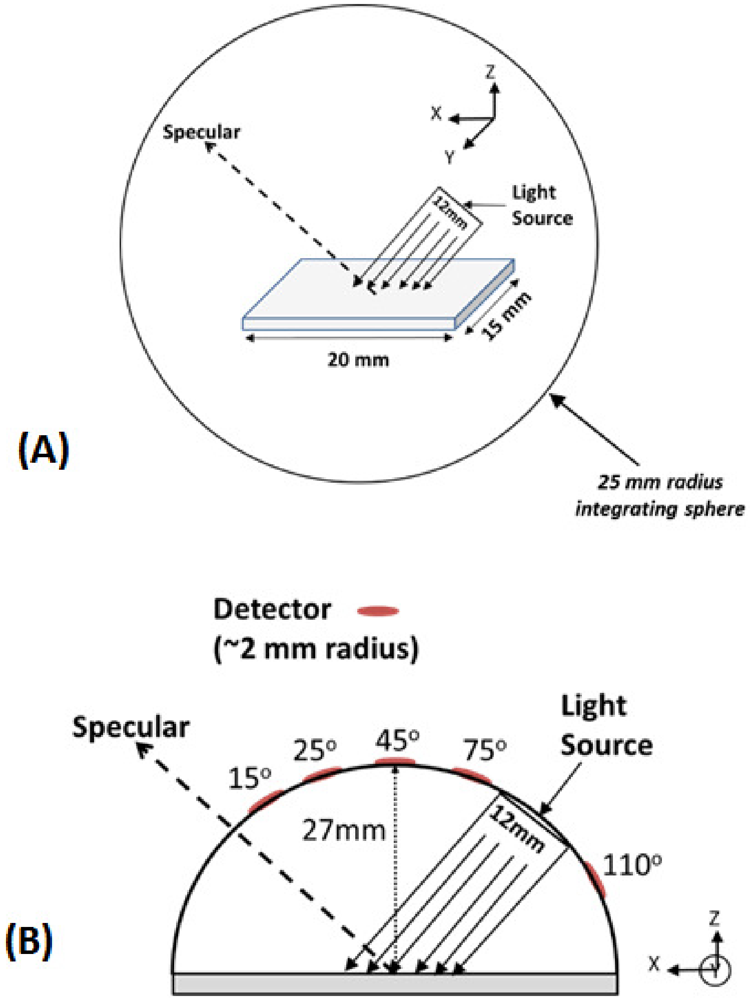

Figure III-7: (A) Schematic of simulation environment. Sample size is 15x20 mm, circular light source with radius of 5.5 mm located 21 mm from surface, integrating sphere of radius 25 mm surrounds the environment. (B) Schematic of handheld spectrophotometer measurement environment. 2 mm sensors are placed at 15°, 25°, 45°, 75°, and 110° OS in the plane of the illumination source. Collimated illumination enters from 45° from normal.

Lightness and flop index measurement and simulation

A small sub-section of the *BRDF* was measured using a handheld spectrophotometer to quantify the color of physical sample. Lightness measurements of the two physical samples under study --Silver #1 and Silver #2-- were made using an MA98 handheld spectrophotometer

(X-rite, Inc., Grand Rapids, MI, USA). This spectrophotometer illuminated the sample —at 45^o from normal— and then captured the scattered light at specific angles: 15^o, 25^o, 45^o, 75^o, and 110^o off-specular (OS). A diagram of this measurement is shown in **Figure III-7B.**

Lightness ($L*$) values were calculated for each of these angles from [54]

$$L* = 116\ (Y/Y_n)^{1/3} - 16\ , \tag{2}$$

where Y is the measured intensity or flux of the light reflected from the sample, and Y_n is the intensity or flux of light that would be reflected at the same angle from a perfectly diffuse white reflector, while 116 and 16 are empirically determined factors.

Flop index (FI) is another colorimetric quantity that was calculated and is of interest to designers. FI is the measurement of how quickly the lightness of a material changes as it is rotated through a range of viewing angles [55]. It is calculated for both the physical and simulated systems using the empirical formula:

$$FI = \frac{2.69(L^*_{15^\circ} - L^*_{110^\circ})^{1.11}}{(L^*_{45^\circ})^{0.86}} \tag{3}$$

A larger value of FI indicates a greater light to dark shift—or lightness travel—as the materials is rotated through the viewing angles. This behavior, in combination with absolute lightness at specific angles, can be of great interest to designers to provide a product with a significant lightness travel.

To simulate the measurement of lightness and FI, a handheld spectrophotometer was virtually built within the simulation environment. The same circular, collimated light source with radius of 6 mm was used to illuminate the system, and circular ports were placed at the above prescribed angles from specular. Each port was created with a 2.0 mm radius and located 36.0 mm from the center of the sample, based on dimensional measurements taken of the spectrophotometer. Each port was also shaded by a 13.0 mm long, 100% absorbing, enclosed cylinder, which prevented rays that did not exit at the prescribed angle from hitting the sensor.

All ray-trace simulations used a collimated light source consisting of 5M individual rays randomly distributed across the aperture, with each ray assigned a flux of 1 watt and a wavelength of 546 nm. The flux of each ray is not significant, as lightness calculations are performed on a relative scale. The wavelength of the light source is also not significant because aluminum platelets reflect uniformly across the visible spectrum, and no other absorptive species are present within these simulated systems. A ray's reflection direction was dictated by the BRDF assigned to the platelet's surface. The effects of the different surface roughness and resulting BRDFs on the final lightness and flop index of the full system will be discussed in the following sections.

Results of physical measurements and simulations

The data presented below show the results of the steps that were taken to generate the physically accurate hybrid ray-wave model for platelet containing paint systems. The effect of surface roughness on the BRDF of individual platelets is reported. How changes in the individual platelet BRDF affect the lightness of the entire paint system is also reported.

Physical measurement of lightness values

Lightness measurements of the two physical samples under study—Silver #1 and Silver #2—and the calculated flop indices are listed in **Table III-2**. These values measured from the physical samples will act as the target values for the hybrid simulations of the Silver #1 and Silver #2 samples.

Table III-2: Lightness and flop index for each of the physically measured and simulated samples. The difference between the simulated and physically measured samples varies based on the angle of observation. The simulation matched well at all angles of observation except 45° OS.

Sample Name	Physical/ Simulation	Platelet BRDF Shape	L^*_{15}	L^*_{25}	L^*_{45}	L^*_{75}	L^*_{110}	*FI*
Silver #1	Physical	N/A	143.3± 0.3	107.2± 0.3	58.6 ± 0.3	37.2± 0.3	32.1± 0.3	15.3± 0.1
Silver #1	Simulation	Measured	128.2± 0.5	112.6± 1.2	81.3± 2.1	42.1± 0.7	36.3± 0.8	8.9± 0.1
Silver #1	Microfacet Simulation	Specular	187.5± 0.7	128.6± 0.5	50.6± 0.2	4.2± 0.02	0	31.9± 0.2
Silver #2	Physical	N/A	129.0± 0.3	106.1± 0.3	67.7± 0.3	43.7± 0.3	36.2± 0.3	11.1± 0.1
Silver #2	Simulation	Measured	122.9± 0.5	109.5± 1.2	81.6± 2.1	47.1± 0.7	37.0± 0.8	8.6± 0.1

Optical profilometry of extracted platelet surfaces and generated Gaussian surfaces

Optical profilometry scans were taken of the platelets extracted from the liquid basecoat. An example of this process is shown in **Figure III-8**. The σ_{RMS} and τ were measured from 20 individual line scans from random platelet regions. An example of a line scan taken from a platelet extracted from Silver #1 is shown in **Figure III-9A**. The average σ_{RMS} was 51.4 nm ± 10.0 nm, and the average τ was 637 nm ± 110 nm.

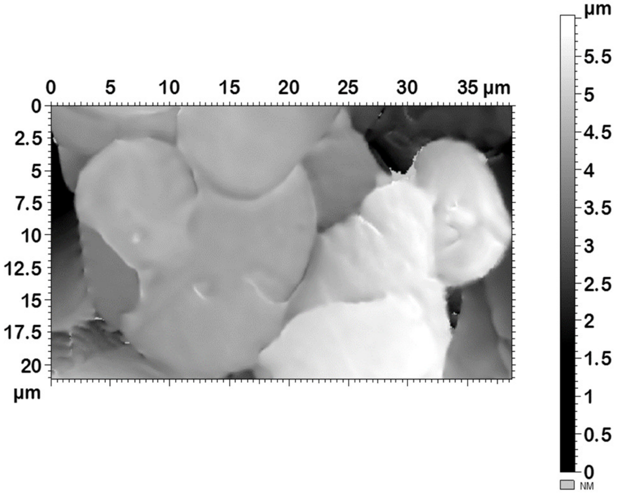

Figure III-8: Optical profilometry scan of platelets extracted from silver metallic paint system. Flakes were washed in acetone and vacuum filtered through No. 2 filter paper.

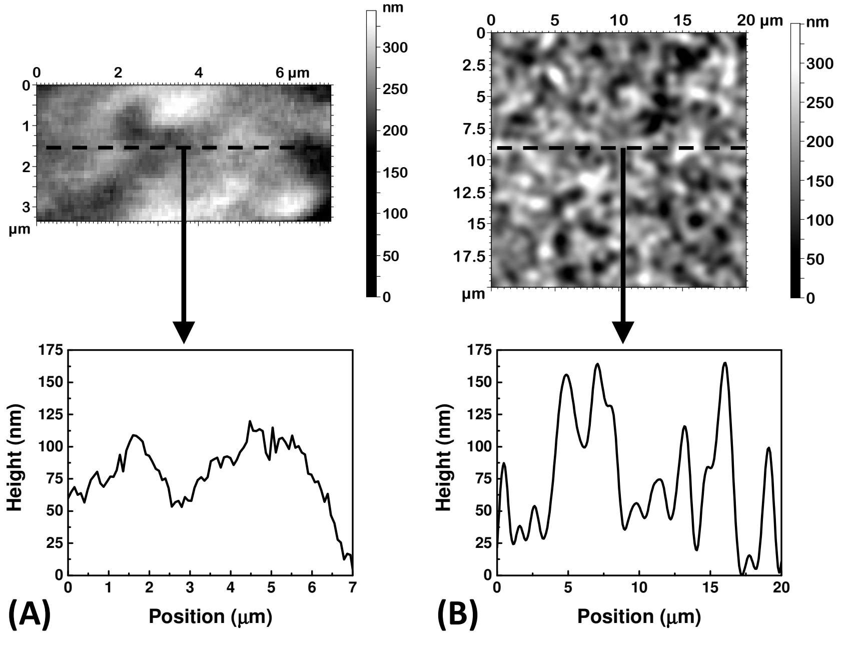

Figure III-9: (A) A series of line profiles were extracted from scanned platelets to measure the true scattering of light from the platelet surfaces. The line profiles were used in the FEA simulations to generate the BRDF of each line profile. The results from ten line profiles were averaged to generate the final BRDF. An example of a profile measured from a platelet in Silver #1 is shown here. (B) Line profiles were also extracted from generated Gaussian surfaces. These line profiles were used to simulate how light would scatter from these hypothetical surfaces. Ten measurements were averaged to create the BRDF of a particular surface. This surface and profile was generated with a σ_{RMS} of 49.2 nm and a τ of 683 nm respectively.

Line scans were directly taken from not only from the measured profilometry data, but also from the simulated 3D Gaussian surfaces for use in the FEA simulations. An example line scan taken from a generated Gaussian surface with σ_{RMS} = 50 nm and τ = 680 nm is shown in **Figure III-9B**. The line scans from the extracted platelets as well as the generated Gaussian surfaces were directly imported into the FEA simulations to calculate their resulting BRDFs.

FEA simulation and BRDF creation from roughness profiles

The line scans obtained from the profilometry of the physical and generated surfaces were imported into the FEA simulation tool for scattering analysis. A far field scattering pattern is shown in **Figure III-10**. In all cases (measured and generated surfaces), the average far field scattering pattern for a particular system was calculated from ten different line scans at 0^{o} and 28^{o} angles of incidence. The average far field scattering pattern for each angle of incidence was then used to estimate the complete BRDF through the interpolation process discussed in section 3.5. The reflection coefficient of the generated BRDF was set to that of aluminum, which is ~92% [56]. This method of BRDF generation was compared to the well-known and generally accepted He-Torrance reflection model. This comparison is discussed in **Appendix III-C**. In addition, a series of studies was performed to measure the likely BRDF of the physically extracted platelets and to determine how the shape of the BRDF differs due to changes in σ_{RMS} and τ.

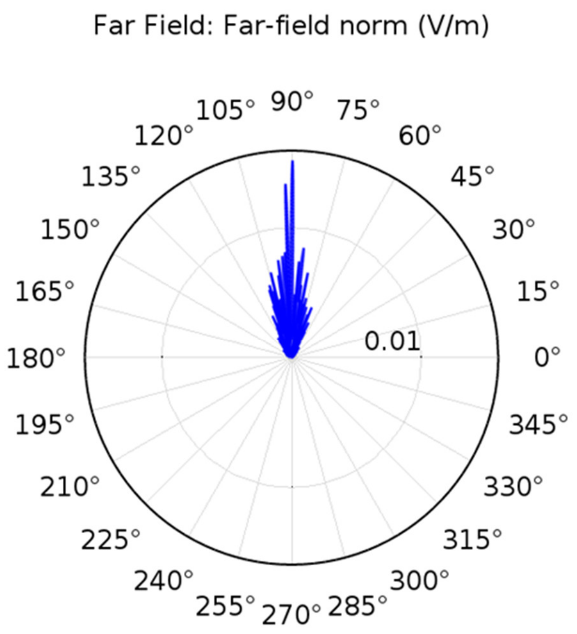

Figure III-10: An example a far field scattering pattern for a simulated surface illuminated by 500 nm light perfectly normal to the surface. Ten far field simulation were averaged to estimate the BRDF of the measured platelet surface. Two angles of illumination—0° and 28°— were used to interpolate the complete BRDF of the surface.

FEA simulation of platelet BRDF

The FEA technique was used to simulate the BRDF for the platelets that were extracted from the silver metallic paint system and whose roughness was measured via optical profilometry. Again, ten separate line patterns were taken from the profilometry data, simulated, and averaged to create the resulting BRDF. This BRDF for illumination nominally normal to the surface is shown in **Figure III-11**. The BRDF possesses a clear specular peak, but also contains a significant amount of light outside of the specular zone.

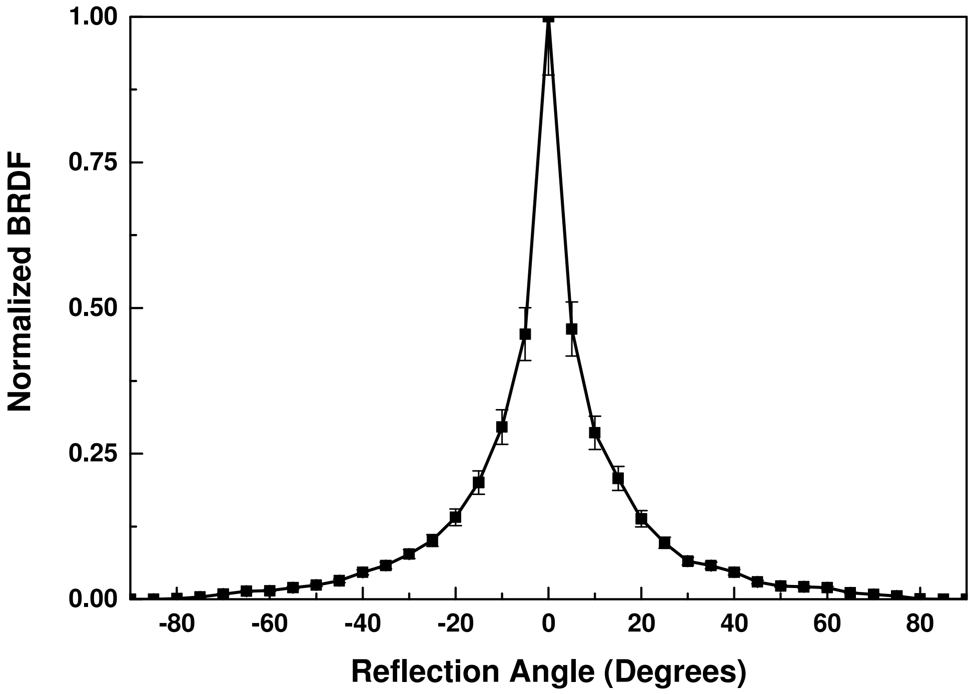

Figure III-11: Normalized BRDF obtained from FEA simulations for extracted aluminum platelets. Angle of incidence was normal to the surface. The reflection pattern still contains a strong specular peak, but contains light outside of the specular zone. Data points are connected as a visual cue only.

FEA simulation of BRDF from generated Gaussian surfaces

Details of the simulated Gaussian surfaces are listed in **Table III-1**. These surfaces were systematically studied to understand how both σ_{RMS} and τ affect the shape of the normalized BRDF. For example, **Figure III-12** shows how the shape of the BRDF changed as σ_{RMS} varied between 25 – 500 nm while τ was held constant at 680 nm. Note how the specular peak disappears once σ_{RMS} reaches ~100 nm and how the reflection lobe broadened as σ_{RMS} increased.

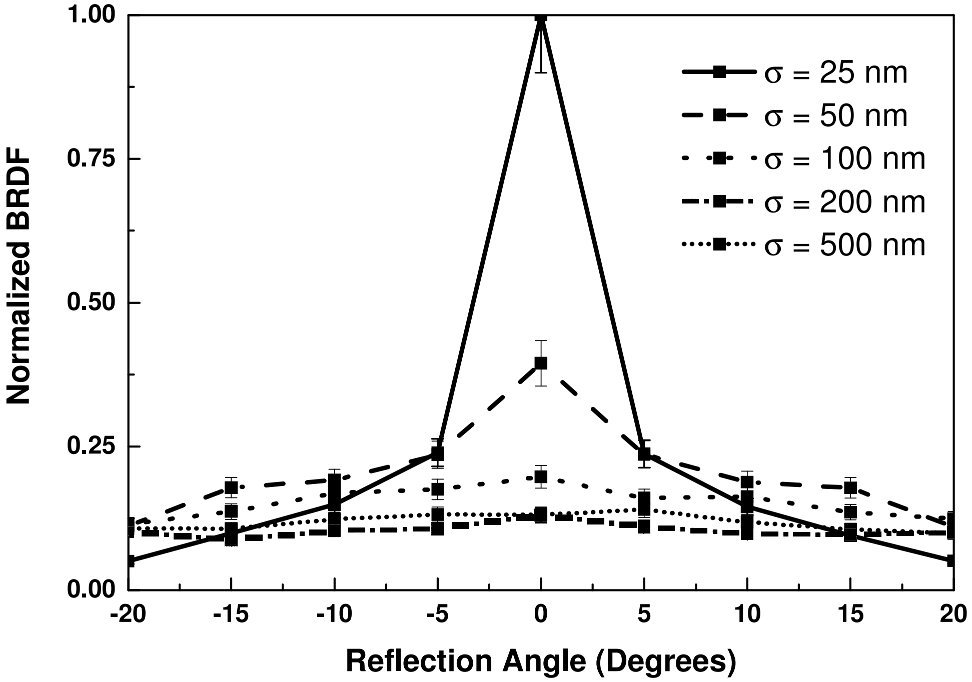

Figure III-12: Normalized BRDF obtained from FEA simulations of surfaces generated with a constant surface correlation length (τ) of 680 nm (slightly larger than the wavelength of light). RMS roughness (σ_{RMS}) was varied between 25 and 500 nm to identify its impact on the shape of the reflection lobe. As σ_{RMS} increased, the specular lobe decreased while the amount of energy diffusely reflected increased. When σ_{RMS} approached 100 nm, the specular reflection lobe vanished. As the roughness continued to increase, little change in the reflection lobe was observed. Data points are connected as a visual cue only.

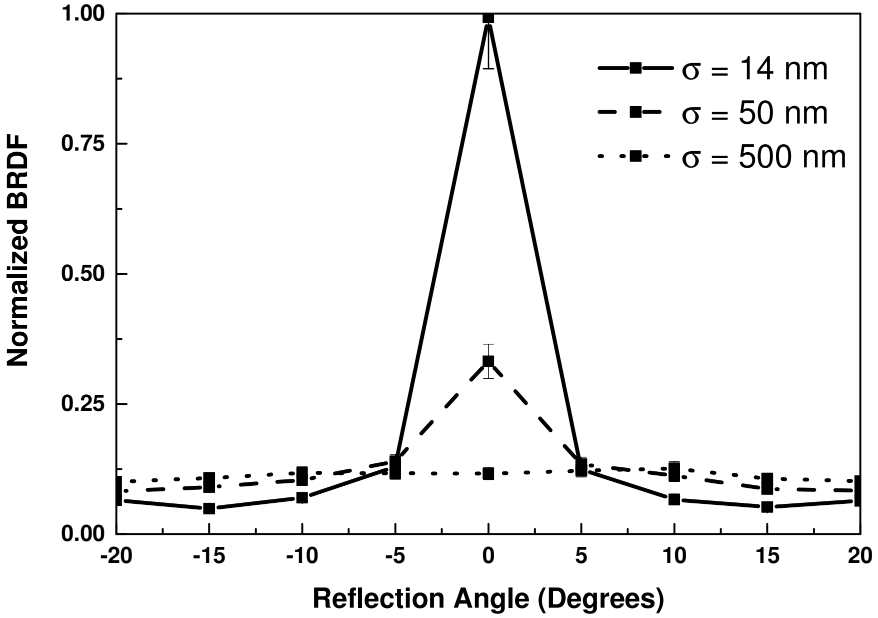

Figure III-13: Normalized BRDF obtained from FEA simulations of generated surfaces with a constant surface correlation length (τ) of 120 nm (significantly less than the wavelength of light). RMS roughness (σ_{RMS}) was evaluated at 14, 50, and 500 nm to identify its impact on the shape of the reflection lobe. As σ_{RMS} increased, the specular lobe decreased while the amount of energy diffusely reflected increased. Again, the specular lobe disappeared when the roughness was > 50 nm. The shape of the 50 nm roughness sample did differ slightly from the 50 nm roughness/680 nm surface correlation length simulation, with additional scattering at the angles outside of ±40^o. Data points are connected as a visual cue only.

The effect of changes in σ_{RMS}, at a low value of τ (120 nm) is shown in **Figure III-13**. A similar loss of the specular peak occurred, but the broadening of the reflection lobe was more apparent even at a σ_{RMS}=50 nm.

The effect of changes in τ on the shape of the BRDF was examined by varying τ between 120 – 1560 nm while holding σ_{RMS} constant at 50 nm. Changes in τ had less impact on the shape of the BRDF than σ_{RMS}, except at the extremes of the range tested. As is shown in

Figure III-14, at the lowest value of τ, a broad BRDF occurred with a small specular peak. As τ increased, the BRDF narrowed slightly into a directionally diffuse shape and did not change significantly until τ was increased to 1560 nm. Once that occurred, the BRDF narrowed even more significantly and exhibited a stronger specular peak.

To determine if the magnitude of σ_{RMS} affects how changes in τ impacts the shape of the BRDF, τ was again varied between 120 – 1440 nm, but σ_{RMS} was increased to 500 nm. Across this range of *τ*, the BRDF was very broad and diffuse in nature, and no change in the specular peak was observed.

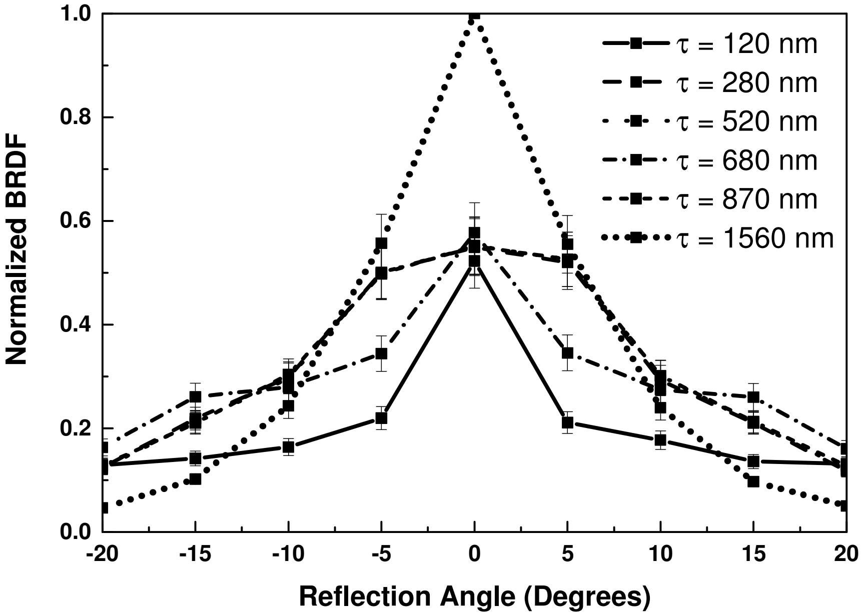

Figure III-14: Normalized BRDF obtained from FEA simulations of generated surfaces with a constant roughness (σ_{RMS}) of 50 nm (significantly less than the wavelength of light). Surface correlation length was varied between 120 and 1560 nm to identify its impact on the shape of the reflection lobe. The BRDFs produced by τ = 280, 520, and 870 nm were all nearly identical and are overlaying each other on the plot. As τ increased, the high angle scattering decreased and transferred into the specular or near specular zone (directionally diffuse). At a correlation length of 300% the wavelength of light, the specular peak/directionally diffuse lobe increased significantly. Data points are connected as a visual cue only.

Ray tracing simulations of Silver #1 and Silver #2 with varying BRDFs

The BRDFs obtained from the extracted platelets (**Figure III-11**) was applied to the platelet surfaces. The resulting lightness properties that resulted from the two different BRDFs were compared.

Five angle lightness values of ray trace simulations that utilized specular and measured BRDFs

The scattering pattern for a simulated coating with the platelet orientation and *PVC* measured for Silver #1 is shown in **Figure III-15** . The scattering pattern simulated from the ray tracing simulations allowed the lightness to be calculated at the standard 5 angles of observations: 15^o, 25^o, 45^o, 75^o, and 110^o OS. The difference between the simulated lightness value and those physically measured at each of the five angles of observation for both Silver #1 and Silver #2 are listed in **Table III-2**. Also shown in **Table III-2** is the result of a microfacet simulation (no gaps or 3D microstructure) based on the same measured platelet orientation for Silver #1 and a purely specular platelet reflection model. The use of the BRDF obtained from the extracted platelets resulted in a relatively accurate simulation of the lightness at 15^o, 25^o, 75^o and 110^o OS when compared to the physical measurements and provides a dramatic improvement over the specular microfacet model. However, the difference between the simulation and physically measured lightness values at 45^o was quite large, where the simulation predicted a significantly lighter sample than what was physically measured. Possible causes of this discrepancy will be discussed later.

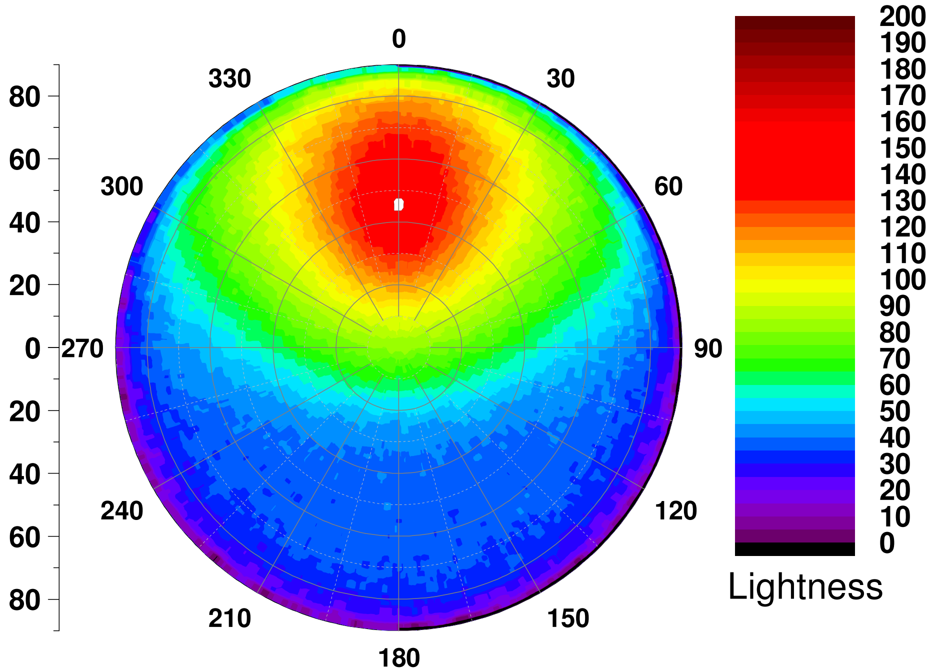

Figure III-15: Polar contour plot of the lightness values obtained from ray trace simulations of the Silver #1 microstructure that utilized the reflection lobe obtained from simulation of the extracted platelets shown in **Figure III-11**. Rays were incident on the surface from the 45° direction at an azimuthal angle of 180°

Five angle lightness values and flop index changes due to surface roughness variation

Lightness values at 15° and 110° OS—geometry illustrated in **Figure III-16**—as well as the flop index that resulted from surface roughness variations (**Table III-1**) are shown in **Figure III-17**. As σ_{RMS} was increased and τ was held constant at 680 nm, lightness at 15° OS rapidly decreased to ~80. Over that same surface roughness range, lightness at 110° OS increased in a linear fashion until reaching ~80. This resulted in a flop index dropping from a value of ~7 to zero when σ_{RMS} reached 500 nm.

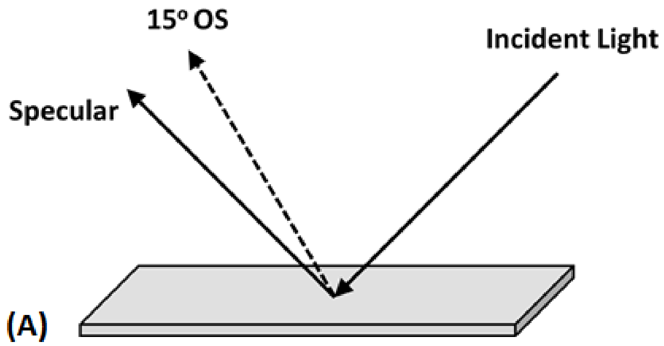

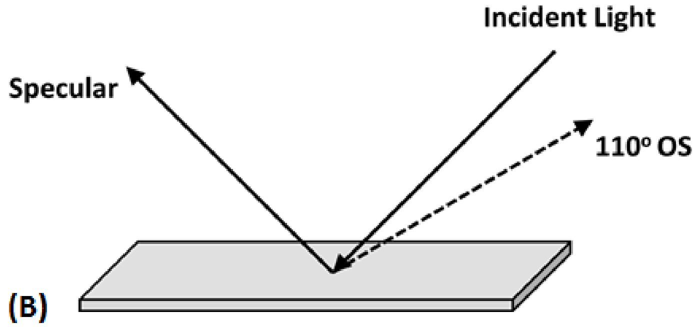

A similar behavior was observed in the lightness and flop index behavior (**Figure III-18**), when σ_{RMS} was again varied between 15 – 500 nm, but τ was reduced to 120 nm (Series #2; **Table III-1**). The lightness at 15^{o} OS again dropped rapidly to a value of ~ 80 as σ_{RMS} increased, while lightness at 110^{o} OS rapidly increased to ~80. The flop index dropped to near zero at a similar rate.

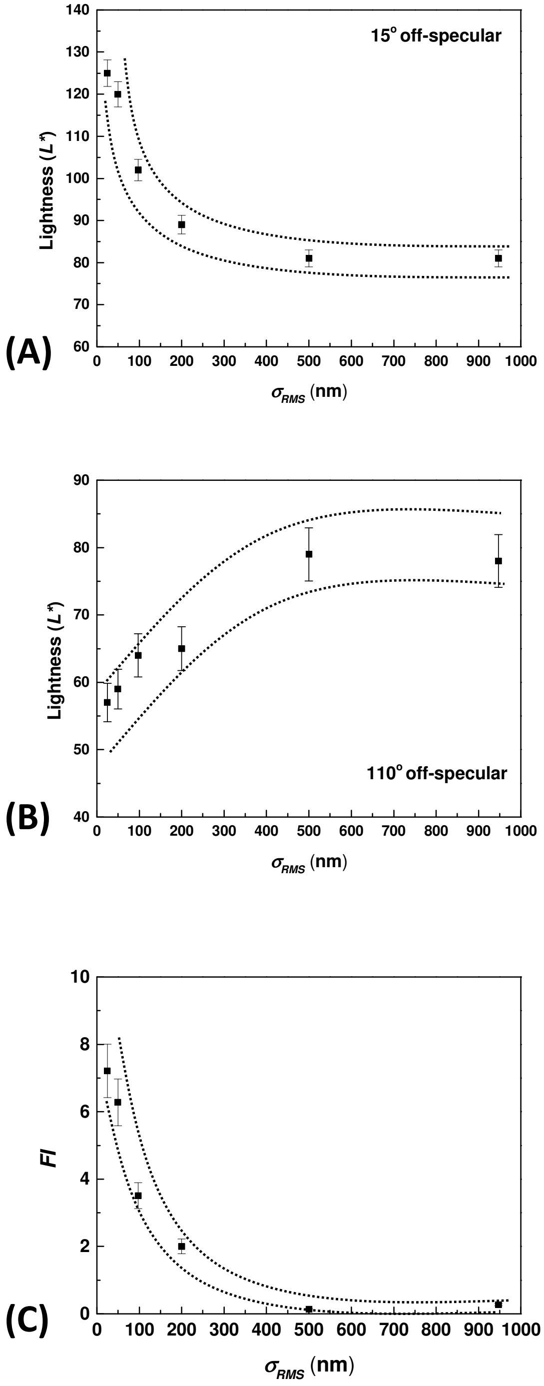

Figure III-17: Simulated lightness at (A) 15° and (B) 110° OS as well as (C) the flop index for the simulated platelet paint system that utilized the reflection patterns based on varying σ_{RMS} and a constant τ of 680 nm (**Figure III-12**). The broadening of the reflection lobe resulted in a rapid decay in lightness at 15° OS and flop index as well as a linear increase in lightness at 110° OS. Once the reflection lobe approached a nearly diffuse state, the lightness at both OS angles approached ~80 and the flop index neared zero. Dashed lines were added to provide a data trend visual cue.

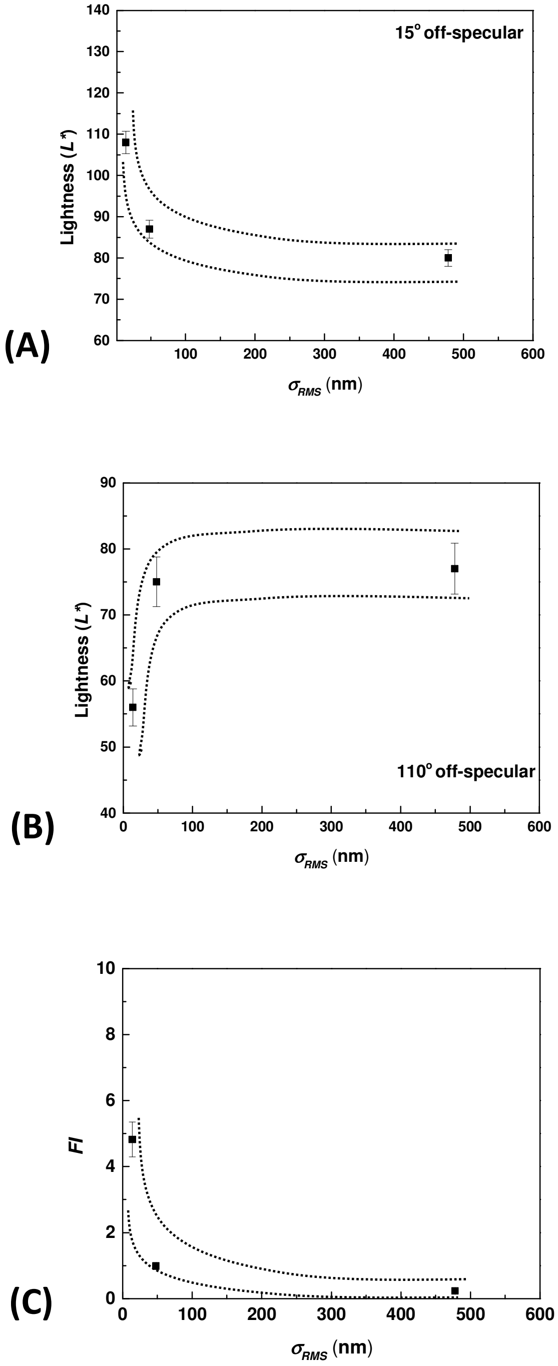

S

Figure III-18: Simulated lightness at (A) 15° and (B) 110° OS as well as (C) the flop index for the simulated platelet paint system that utilized the reflection patterns based on varying σ_{RMS} and a constant τ of 120 nm (**Figure III-13**). The effect of roughness changes was enhanced due to the relatively low correlation length and lead to the lightness at 15° and 110° *OS* to rapidly approach ~80. This was caused by the significant amount of scattering occurs out to angles outside of ± 30° at low roughness values of ~15-50 nm. Flop index followed a similar trend. Dashed lines were added to provide data trend visual cue.

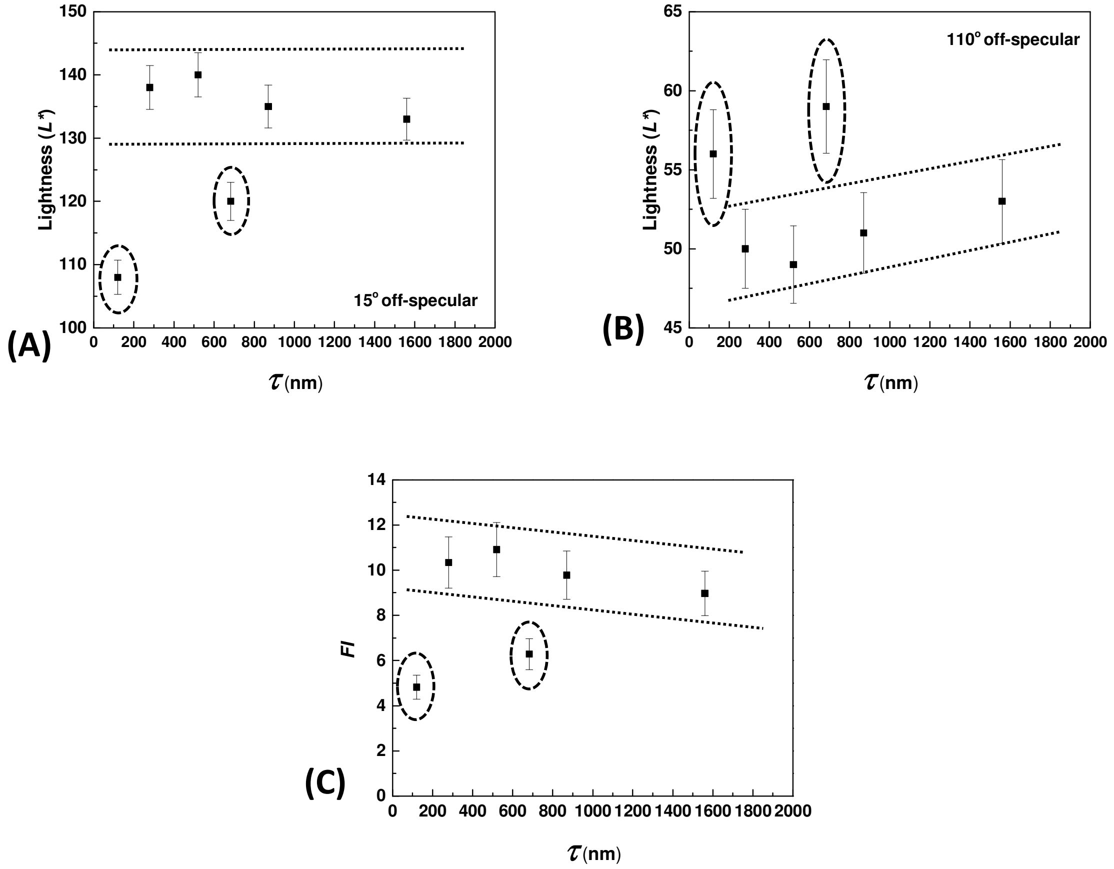

Figure III-19: Simulated lightness at 15° (A) and 110° (B) OS as well as the flop index (C) for the simulated platelet paint system that utilized the reflection patterns based on varying τ and a constant of σ_{RMS} of 50 nm (**Figure III-14**). The effect of surface correlation length changes had minimal effect on the resulting lightness and flop index. At very low τ the lightness at 15° *OS* hit a minimum for the series and is due to the small surface correlation length causing significant amounts of diffuse scattering. However, once τ approached the wavelength of light, this diffuse scattering disappeared and resulted in a relatively stable lightness and flop index behavior. The point at $\tau = 680$ nm fell just outside of the error bars of the other points and may simply be an anomaly of the simulation related to the wavelength of the light, the simulation size, and the length scales of the roughness and surface correlation length. Outliers are circled with a dashed line while dotted lines were added to provide data trend visual cue.

Values of lightness and flop index that resulted when σ_{RMS} was held constant at 50 nm, but τ was varied between 120 – 1560 nm (**Table III-1**) are shown in **Figure III-19**. At the lowest value of τ (120 nm), the lightness at 15° OS and flop index reached minimums of ~107 and ~5 respectively. The lightness at 110° OS ranged between ~50 – 60 for all values of τ and exhibited no particular trend. At values of τ greater than 120 nm, the lightness at 15° OS also showed no particular trend, with all but one sample possessing a lightness of 135 – 140. However, the 15° OS lightness for the sample with a τ of 680 nm fell significantly outside of this range with a value of ~120.

Discussion

Silver metallic paint systems contain features on a variety of size scales, from micrometer sized platelets arranged in multiple layers to the nanometer sized roughness of the platelet surfaces. These multiple length scales were the motivation to utilize a hybrid approach that incorporated both wave and ray optics within a single simulation environment. This sequential, hybrid approach was used to more accurately predict the scattering behavior of physical silver metallic paint systems and predict how changes to both the platelet microstructure and the surface roughness affected the appearance of the system. This approach, however, can be used to predict the scattering behavior of any 3D layered structure where the size of the microstructural feature is on the order of the wavelength of light.

Physical measurements vs. simulated lightness values

The BRDF used for the surfaces of the platelets contained within the ray trace simulation is shown in **Figure III-11**. As expected, the BRDF has a strong specular component, but also contains a significant amount of light outside of the specular zone.

The difference between the lightness values obtained from ray trace simulations and the physically measured lightness values for each physical sample is shown in **Table III-2**. As was previously discussed, the simulation proved to be highly accurate, especially compared to a specular microfacet model, and allowed us to identify the same darkening at 15^o and lightening at 110^o that was observed the physical samples. It should be noted that the accuracy of the simulation at 45^o OS was not as high.

We hypothesize that neither gap factor nor platelet edges significantly affect the lightness at 45^o. It is possible the shape of the platelet BRDF significantly contributes to this 45^o lightness. The region of the BRDF that would affect the lightness @ 45^o OS is the outer edge of the reflection lobe. The location of this edge is likely susceptible to error due to variations in platelet roughness. A simple narrowing of the BRDF lobe could significantly change the lightness at 45^o OS while having minimal effect on the lightness at other near specular angles.

Simulated surface roughnesses

It is clear that the shape of the platelet BRDF significantly affects the lightness of the final paint system. To explore these effects further, Gaussian surfaces were generated based on σ_{RMS} and τ to quantify how changes in each of these parameters affect not only the BRDF of the rough surface, but also how that BRDF affects the lightness behavior of the complete paint system.

Roughness and BRDF shape

The impact of changes in σ_{RMS} and τ on the shape of the BRDF are shown in

Figure III-12 - Figure III-14. As was discussed previously, if σ_{RMS}/λ is near unity, the shape of the platelet BRDF approaches that of a perfectly diffuse reflector.

As σ_{RMS} was decreased below the illumination wavelength, the BRDF became more focused in the specular direction. A strong specular peak did not appear until σ_{RMS} approached 50 nm, regardless of the value of τ.

Even though τ did not affect the appearance of the specular peak that resulted from a reduction in σ_{RMS}, it did have an effect on the shape of the BRDF outside of the specular zone. In general, the BRDFs exhibited a moderate specular component. But, at extreme values of τ, the amount of light reflected at angles > 10^{o} changed significantly. A small value of τ (~0.2λ) resulted in a significant amount of reflection through ~±60^{o}—see **Figure III-14**. Once τ was increased to a range of ~0.5-1.5λ, the BRDF narrowed and only possessed a significant amount of light through ~±40^{o}. Once τ reached a value of 3λ, the BRDF was even more focused and specular. While τ does not affect the BRDF as much as σ_{RMS}, it must be considered if this model and method is used to digitally create a new scattering microstructure using layered, roughened metallic scatterers. Slight changes in the BRDF generated with this model can and will likely cause significant changes in the appearance of the newly produced color.

BRDF effect on lightness and FI of full paint system

The results presented in **Figure III-17--Figure III-19** show how changes to the roughness and BRDF affect the overall lightness of the paint system. Qualitative inspection of the BRDF curves that resulted from changes in surface roughness show σ_{RMS} has a greater impact on the shape of the BRDF curve than τ. It was shown that even a small improvement in σ_{RMS} can result in a significant, observable change in lightness and flop index. This is important not only for designers and formulators to consider, but also for computer models and visualization packages to include in their simulations to improve their accuracy. A BRDF shape that is “close enough” is unacceptable if engineering decisions need to be made based on simulation results.

Interestingly, as σ_{RMS} approached the wavelength of light and its BRDF approached a perfectly diffuse reflector, the lightness at the forward and backward scattering angles approached a value of 80. This is significantly less than the expected value of a perfectly diffuse reflector, which is 100. The difference is likely due to the absorption of energy that occurs when light reflects off the aluminum platelets. Additional absorption occurs as a result of multiple reflection events. Our previous work has shown that the gaps between platelets can increase the number of multiple reflection events. Additionally, a broadened BRDF can reflect some light below the critical angle and increase the number of multiple reflection events. A system that increases multiple reflection events via either of these two pathways will reduce the lightness even further.

The lightness of these layered platelet paint systems does not appear to be as dependent on τ as it is on σ_{RMS}. The data presented in **Figure III-19** does show a lightness minimum when τ was only 120 nm. As τ was increased above 120 nm, the lightness leveled off for the 15^o and 110^o OS angles of observation at ~135 and 50 respectively and exhibited little further change as τ increased. The simulated system with a τ of 680 nm did fall just outside of the error range, indicating that this sample exhibited a significant difference in lightness at both the 15^o and 110^o OS angles of observation. As no obvious physical reason for this outlier behavior exists, it is possible that this was simply an unexpected error in the width of the simulated BRDF in **Figure III-14** compared to the simulated BRDFs in **Figure III-12** and **Figure III-13** respectively.

It has already been shown that the lightness at 15^o can change dramatically because of small changes in the BRDF shape. To maximize flop index, platelets with the optimal σ_{RMS} should be chosen as τ has little effect once it is greater than ~100 nm.

Ideally, an equation that predicts the lightness of these layered systems from specific BRDF attributes such as peak height or full width at half maximum (FWHM) could be generated from the reported data. However, this specific relationship can change significantly if other microstructural properties are altered, such as platelet orientation or *PVC.* Qualitatively, the trends may be similar, but it is not possible to generate an overarching equation to predict how surface roughness affects the lightness of any and all 3D metallic paint systems. The hybrid model must be used to analyze specific formulations and microstructure and identify the necessary relationships between surface roughness, platelet orientation, *PVC*, gap factor, platelet thickness, etc. if any type of predictive modeling is desired.

Conclusion

Color and appearance is a key product differentiator for a range of industries. In order to minimize the time and cost associated with the development of a new color, a hybrid modeling approach was developed that utilized both ray tracing and FEA simulations to predict the lightness of a silver metallic paint system over all angles of illumination and observation.

We explored the effect of surface roughness on the shape of the BRDF of the platelet surfaces and ultimately the lightness of the complete paint system. Flake roughness, σ_{RMS}, significantly affected the lightness behavior of the silver paint systems, especially at the near specular reflection angles, whereas the surface correlation length, τ, had little effect on the lightness behavior once it exceeded ~100 nm.

With regard to predicting appearance, this hybrid approach can be used to model the impact of unique scattering media contained within a dielectric medium. Particles or platelets based on structural color, interference effects, or other unique scattering or absorptive properties can be built into a model paint system and optically analyzed. The use of this model can help designers and engineers focus their development efforts on high impact, high return systems that provide new and unique appearance characteristics.

A desired improvement in the appearance of silver paint systems includes a maximization of lightness at 15^{o} OS and a minimization of lightness at 110^{o} OS. This change was observed when the BRDF of these platelet paint systems was changed to be purely specular. However, it is unclear how a change in the shape of the platelet's BRDF affects the relationship between bulk microstructural properties (platelet width, PVC, thickness) and lightness. We will systematically examine this relationship in future work.

Outside of product appearance, scattering particles can help a material perform a specific function. One area of interest is the creation of stealth and cloaking technologies. Physical prototypes of these technologies are difficult and expensive to produce. A researcher could potentially use the methodology discussed above to evaluate new scattering technologies and identify potential systems and microstructures of interest. Once these technologies have been placed into a digital simulation environment and optimized, physical samples can be produced and tested for performance. This workflow could limit cost and development time and help companies focus on high impact optical systems.

Appendix III-A

The volume concentration of platelets contained within the wet paint layer differs from that within the cured paint layer due to loss of binder volume that occurs during cure due to crosslinking and the formation of crosslinking products, such as low molecular weight alcohols. The in-film platelet volume concentration was measured by 2D cross sectional analysis of cured physical samples (**Figure III-20**). The 3D volume concentration has been shown to be equivalent to 2D area fraction if a statistically sufficient number of regions are analyzed [57,58]. This analysis resulted in a measured 2D area fraction of ~20%.

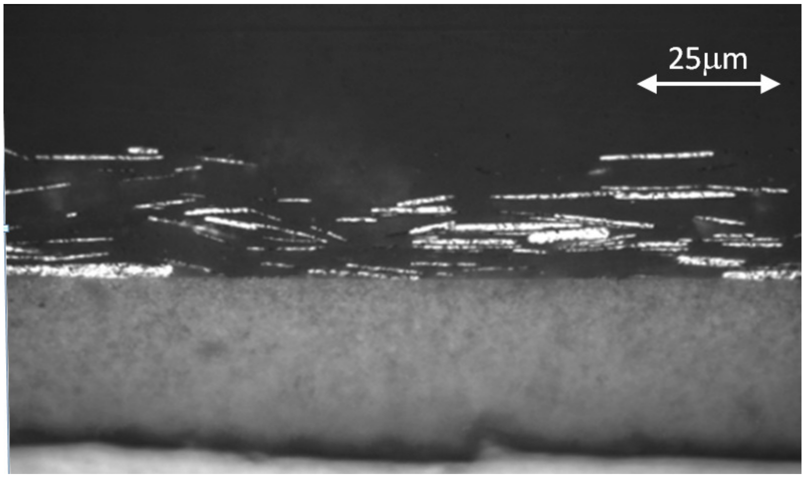

Figure III-20: 2D cross sectional view of Silver #1 that was studied previously [49]. Area fraction of the platelets was measured for a series of cross sections to determine the approximate volume concentration of a typical hiding silver basecoat. This pigment volume concentration was calculated to be 20 ± 4%

Appendix III-B

File name: Main.cpp

```
// Main module that generates the flakes/platelets, tracks attributes, and exports different
formats as needed.
// Flake Creation settings are in FlakeCreator.cpp.

// Global protected variables
#ifndef FLAKE_CPP_INCLUDED
#define FLAKE_CPP_INCLUDED
#include "Flake.cpp"
#endif
#ifndef FLAKECREATOR_CPP_INCLUDED
#define FLAKECREATOR_CPP_INCLUDED
#include "FlakeCreator.cpp"
#endif
#ifndef FLAKEBOX_CPP_INCLUDED
#define FLAKEBOX_CPP_INCLUDED
#include "FlakeBox.cpp"
#endif
#ifndef VOLUMEOFBOXES_CPP_INCLUDED
#define VOLUMEOFBOXES_CPP_INCLUDED
#include "VolumeOfBoxes.cpp"
#endif
#ifndef SAVEFLAKES_CPP_INCLUDED
#define SAVEFLAKES_CPP_INCLUDED
#include "SaveFlakes.cpp"
#endif

using namespace std;

// Prototyping
void load(int* printFlakeDataPoints, int* printTexture, int* printVertexes);
float convertStringToFloat(string line);

// Start of the program. The main part that is run
int main()
{

   srand(time(NULL)); // Seed the random number generator

   // Setup defaults for values
```

```
   int printFlakeDataPoints = 1;
   int printTexture = 1;
   int printVertexes = 1;
   int printSpecial = 1;
   int printThickness = 1;

   // Format output
   cout << setiosflags(ios::fixed) << setprecision(8);

   // Attempt to read data from config file
   load(&printFlakeDataPoints,&printTexture,&printVertexes);

   // Create the flakes/platelets
   FlakeCreator flakeCreator = FlakeCreator();
   flakeCreator.print(); // Print the values loaded with the creator
   vector<Flake> flakes = flakeCreator.createFlakes();
   cout << "Number of Flakes: " << flakes.size() << endl;

   // Create the Boxes, The last arg is the largest flake
   Flake flake = flakes.at(0);
   VolumeOfBoxes volumeOfBoxes = VolumeOfBoxes(flake.getXArea(), flake.getYArea(),
flake.getZArea(), flakes.back().getXWidth());

   int fails = 0;
   int failures = 0;


   // These are the x, y, and z positions
   float x = 0.0;
   float y = 0.0;
   float z = 0.0;


   // This section is when uniform spacing is desired
   //---------------------------------------------------
   // Set uniform spacing
   float xSpacing = flakeCreator.getXSpace() * .000001;
   float ySpacing = flakeCreator.getYSpace() * .000001;
   float zSpacing = flakeCreator.getZSpace() * .000001;

   // These represent the number of flakes stored in a line in each dimension for a random
distribution
   int xPosR = 0;
   int yPosR = 0;
```

```
   int zPosR = 0;

   // These represent the number of flakes stored in a line in each dimension for a uniform
distribution
   int xPosU = 0;
   int yPosU = 0;
   int zPosU = 0;

   // These are the maximum number of flakes used in both the x and y directions, they are
used to end the loop if there are less flakes available than a filled layer of flakes
   int xMax = 0;
   int yMax = 0;

   float size = 0.0; // This is the number of flakes that are not given a location
   float fractionOfLength = pow(flakeCreator.filledVolume, (1.0/3.0)); //this is used to
determine how much space randomly distributed flakes should take up, NOT SURE IF math to
this number is correct

   // This loop acts like a nested loop, where the if statements at the bottom regulate the
change in x, y, and z positions

   for(int a = flakes.size()-1; a >= 0;) { // Loop through every flake

      if (flakeCreator.getUniformXDist() == 0) { // Position of random x spacing
         flakes.at(a).generateXPosition();
         xPosR += 1;
      } else { // Position of uniform x spacing
         flakes.at(a).generateXPosition(x);
         x = x + xSpacing + flakes.at(flakes.size()-1).getXWidth();
         xPosU += 1;
      }


      if (flakeCreator.getUniformYDist() == 0) { // Position of random y spacing
         flakes.at(a).generateYPosition();
      } else {
         flakes.at(a).generateYPosition(y); // Position of uniform y spacing
      }


      if (flakeCreator.getUniformZDist() == 0) { // Position of random z spacing
         flakes.at(a).generateZPosition();
      } else {
         flakes.at(a).generateZPosition(z); // Position of uniform z spacing
```

```
    }



    // This section checks the boundries of the Volume of Boxes for flake placement and it
records the maximum number of flakes in a row/column
    if(xPosU > xMax) {
       xMax = xPosU;
    }

    // This resets the x position if there is no more space in the x direction and it increases the
y position
    if((x > volumeOfBoxes.boxDimension *  volumeOfBoxes.xBoxes) || (((xPosR *
flakes.back().getXWidth())/(volumeOfBoxes.boxDimension *  volumeOfBoxes.xBoxes)) >
fractionOfLength)) {
       // These reset the appropriate variables for the types of y spacing
       if(flakeCreator.getUniformYDist()==0) {
          yPosR +=1;
          xPosR = 0;
          x = 0.0;
          xPosU = 0;
       } else {
          yPosU +=1;
          x = 0.0;
          xPosU = 0;
          y = y + ySpacing + flakes.at(flakes.size()-1).getYWidth();
       }
    }

    if(yPosU > yMax) { // Records the maximum flakes that are in the y direction
       yMax = yPosU;
    }

    // This resets the y position if there is no more space in the y direction and it increases the
z position
    if ((y > volumeOfBoxes.boxDimension *  volumeOfBoxes.yBoxes) || (((yPosR *
flakes.back().getYWidth())/(volumeOfBoxes.boxDimension *  volumeOfBoxes.yBoxes)) >
fractionOfLength)) {
       // These reset the appropriate variables in the z direction
       if(flakeCreator.getUniformZDist()==0) {
          yPosR = 0;
          zPosR +=1;
          yPosU = 0;
          y = 0.0;
```

```
           } else {
              zPosU +=1;
              z = z + zSpacing + flakes.at(flakes.size()-1).getThickness();
              yPosU = 0;
              y = 0.0;
           }
        }

        // This section checks for intersections
        vector<FlakeBox*> boxes = volumeOfBoxes.relevantBoxes(flakes.at(a));// Find the boxes
that it is in collision with
        bool intersection = false;
        for(int j = 0; j < boxes.size(); j++) { // For every box the flake is intersecting
           if(boxes.at(j)->flakeIntersection(flakes.at(a))) { // If the flake does intersect with the
flakes in the box

              intersection = true;
              fails++;
              break;
           }
        }

        intersection = false;

        if(!intersection) { // If no intersections were found
           for(int j = 0; j < boxes.size(); j++) { // loop through every box
              boxes.at(j)->addFlake(flakes.at(a)); // add the flake to the box
           }
           if(a%10000 == 0) { // Every 1000 flakes
              cout << a << endl;
           }
           a--; // Move to the next flake
           fails = 0;
        }
        if(fails > 1000) { // We have failed too many times and just place the flake in the volume
           cout << "FAILURE" << endl;
           failures++;
           a--;
           fails = 0;
        }


        // This terminates the loop if there is no more space in the z direction or a new layer
cannot be completed
```

```
        if((z > volumeOfBoxes.boxDimension *  volumeOfBoxes.zBoxes) || (a <= (xMax*yMax)) ||
(((zPosR * flakes.back().getThickness())/(volumeOfBoxes.boxDimension *
volumeOfBoxes.zBoxes)) > fractionOfLength)) {

            size = a;
            a = -1;
        }

    }
    // This removes the flakes that were not given a space
    flakes.erase(flakes.begin(), flakes.begin() + size);


//==============================================================================
====



    cout << "Failures: " << failures << endl;

    cout << "Clear Boxes" << endl;
    volumeOfBoxes.emptyBoxes(); // Desconstruct the boxes to save memory


    if(printFlakeDataPoints) {
        cout << "Saving Flake Data Points" << endl;
        saveFlakeDataPoints(flakes);
    }

    if(printTexture) {
        cout << "Saving Flake Textures" << endl;
        saveFlakeTextures(flakes);
    }
    if(printTexture) {
        cout << "Saving Flake Textures" << endl;
        saveFlakeTextures1(flakes);
    }
    if(printTexture) {
        cout << "Saving Flake Textures" << endl;
        saveFlakeTextures2(flakes);
    }
    if(printTexture) {
        cout << "Saving Flake Textures" << endl;
        saveFlakeTextures3(flakes);
```

```
    }
    if(printTexture) {
        cout << "Saving Flake Textures" << endl;
        saveFlakeTextures4(flakes);
    }
    if(printTexture) {
        cout << "Saving Flake Textures" << endl;
        saveFlakeTextures5(flakes);
    }
    if(printVertexes) {
        cout << "Saving Flake Vertexes" << endl;
        saveFlakeVertexes(flakes,flake.getCirclePoints());
    }

    if(printSpecial) {
        cout << "Saving Flake Vertexes Special" << endl;
        saveFlakeSpecial(flakes);
    }
    if(printThickness) {
        cout << "Saving Flake Thicknesses" << endl;
        saveFlakeThicknesses(flakes);
    }
    cout << "Number of Flakes: " << flakes.size() << endl;
    cout << "Finished!" << endl;
    flakes.clear();
    return 0;
}

// Loads in some values from the config file
void load(int* printFlakeDataPoints, int* printTexture, int* printVertexes)
{
    ifstream config ("Config.txt");
    string line;
    if(config.is_open()) {
        getline(config,line);
        *printFlakeDataPoints = convertStringToFloat(line);
        getline(config,line);
        *printTexture = convertStringToFloat(line);
        getline(config,line);
        *printVertexes = convertStringToFloat(line);
        config.close();
    } else {
        cout << "Failed to open config file, continuing with defaults" << endl;
    }
```

```
}

float convertStringToFloat(string line)
{
   float toReturn = 0.0;
   stringstream convert(line);
   convert >> toReturn;
   return toReturn;
}
```

Filename: Flakecreator.cpp

```
// This module generates each flakes width, thickness, orientation, and center point location
within a prescribed volume.  Values used to generate these quantities are located within the
config.txt file

// Protected global variables
#ifndef FLAKECREATOR_H_INCLUDED
#define FLAKECREATOR_H_INCLUDED
#include "FlakeCreator.h"
#endif
#ifndef CHRONO_INCLUDED
#define CHRONO_INCLUDED
#include <chrono>
#endif
#ifndef FSTREAM_INCLUDED
#define FSTREAM_INCLUDED
#include <fstream>
#endif
#ifndef RANDOM_INCLUDED
#define RANDOM_INCLUDED
#include <random>
#endif
#ifndef ALGORITHM_INCLUDED
#define ALGORITHM_INCLUDED
#include <algorithm>
#endif

using namespace std;

FlakeCreator::FlakeCreator()
{
```

```
   // Constructor called the load method to put the values into their respective spots

load(&filledVolume,&xArea,&yArea,&zArea,&percentFlakeThickness,&percentThickness,&other
FlakeThickness,&p1,&p2,&p3,&p4,&q1p5,&q2p6,&q3p7,&p8,&circlePoints,&alpha,&beta,&hav
eXAngle,&elongated, &setXAngle, &newXAngle, &setZAngle, &newZAngle, &uniformXDist,
&xSpace, &uniformYDist, &ySpace, &uniformZDist, &zSpace);
}

// The actualy part of the code that creates all the flakes.  May need changing in the future
vector<Flake> FlakeCreator::createFlakes()
{
   // Calculate up the total volume that flakes will populate
   float totalVolume = xArea * yArea * zArea;
   float currentVolume = 0;
   // Create a structure to hold out flakes
   vector<Flake> flakes;

   float xAngle = 0;
   float zAngle = 0;

   // Allows the user to manually set the x angle of the flakes
   int YorNx;
   YorNx = setXAngle;

   if (YorNx == 1) {
      xAngle = newXAngle;

   }


   // Allows user to uniformly set the z angle
   int YorNz;
   YorNz = setZAngle;

   if (YorNz == 1) {
      zAngle = newZAngle;

   }

   // Tracker used to calculate total created flake/platelet volume generated.  Once total
volume exceeds volume fraction of flakes/platelets, generator stops.
   while(currentVolume < (totalVolume*filledVolume)) {

      // GENERATE FLAKE THICKNESS
```

```
    // ------------------------------------------------------------------------------------
    // Generate a random to decide which thickness to make this flake/platelet.  This is used if more than one thickness of flake/platelet is present used.
    float randForThickness = ((float)rand()/(float)RAND_MAX);
    float flakeThickness = 0;
    // If our rand is less than or equal to our percent thickness
    if(randForThickness<=percentThickness) {
       // Make our thickness our percent percent flake thickness
       flakeThickness = percentFlakeThickness;
    } else {
       // Else it is just the other flake thickness
       flakeThickness = otherFlakeThickness;
    }
    // ------------------------------------------------------------------------------------

    // GENERATE FLAKE RADIUS
    // ------------------------------------------------------------------------------------
    float m0 = ((float)rand()/(float)RAND_MAX); // Random # 0 to 1
    float flakeRadius = 0.0;
    if(p8 == 0) { // For distributions of radaii, flake radius was fitted to either a 7th or 8th order polynomial.
       flakeRadius = (p1*pow(m0,3) + p2*pow(m0,2) + p3*m0 + p4) / (pow(m0,3) + q1p5*pow(m0,2) + q2p6*m0 + q3p7);
    } else { // Else just use the 7th level polynomial
       flakeRadius = (p1*pow(m0,7) + p2*pow(m0,6) + p3*pow(m0,5) + p4*pow(m0,4) + q1p5*pow(m0,3) + q2p6*pow(m0,2) + q3p7*m0 + p8);
    }
    flakeRadius *= 0.001; // Convert micrometers to mm for correct inclusion in ray tracing software.
    // ------------------------------------------------------------------------------------

    float area = 3.14159*pow(flakeRadius,2); // Calculate the area the flake is taking up
    if(elongated == 1) area *= 1.5; // Added feature if elongated rectangular flakes are wanted.

    // GENERATE WIDTHS
    // ------------------------------------------------------------------------------------
    float yWidth = pow(area,0.5);
    float randWidth = ((float)rand()/(float)RAND_MAX) + 1; //  Rand num 1 to 2
    float xWidth = pow(area,0.5);
    if(elongated == 1) xWidth *= randWidth;
    // ------------------------------------------------------------------------------------

    currentVolume += area * flakeThickness; // Add the flake volume to the current volume
```

```
        // GENERATE ANGLES
        // --------------------------------------------------------------------------------------
        if (YorNx == 0) {
           if(haveXAngle) { // If the flakes/platelets are supposed to have a xangle, we used a
gamma distribution to generate the flake/platelet angle.
              // http://www.cplusplus.com/reference/random/gamma_distribution/
              // Use the alpha and beta values for the gamma distribution
              gamma_distribution<float> distro(alpha,beta);
              unsigned seed = chrono::system_clock::now().time_since_epoch().count();
              std::default_random_engine generator(seed); // Use the clock time as a number for
our generator
              xAngle = distro(generator); // generate a random number within our disribution
           }
        }

        if(YorNz == 0) {

           zAngle = 360 * ((float)rand()/(float)RAND_MAX); // Rotation about the z-axis is simply a
random angle between 0 and 360 degrees.

        }

        // --------------------------------------------------------------------------------------

        // Construct the flake and add it to the vector structure
        flakes.push_back(Flake(xWidth, yWidth, flakeThickness, xAngle, zAngle, xArea, yArea,
zArea, circlePoints, uniformXDist, xSpace, uniformYDist, ySpace, uniformZDist, zSpace));
    }
    cout << "CurrentVolume: " << currentVolume << endl;
    cout << "Volume to be Filled: " << totalVolume*filledVolume << endl;
    // Sort the flakes so the largest is at the end
    sort(flakes.begin(),flakes.end());
    return flakes;
}

// Dumps the loaded in data into standard out so what was loaded in can be double checked
void FlakeCreator::print()
{
    cout << "Flake Creation Values" << endl;
    cout << "filledVolume:\t\t\t" << filledVolume << endl;
    cout << "xArea:\t\t\t\t\t" << xArea << endl;
    cout << "yArea:\t\t\t\t\t" << yArea << endl;
    cout << "zArea:\t\t\t\t\t" << zArea << endl;
```

```
   cout << "percentFlakeThickness:\t" << percentFlakeThickness << endl;
   cout << "percentThickness:\t\t" << percentThickness << endl;
   cout << "otherFlakeThickness:\t" << otherFlakeThickness << endl;
   cout << "p1:\t\t\t\t\t" << p1 << endl;
   cout << "p2:\t\t\t\t\t" << p2 << endl;
   cout << "p3:\t\t\t\t\t" << p3 << endl;
   cout << "p4:\t\t\t\t\t" << p4 << endl;
   cout << "q1p5:\t\t\t\t" << q1p5 << endl;
   cout << "q2p6:\t\t\t\t" << q2p6 << endl;
   cout << "q3p7:\t\t\t\t" << q3p7 << endl;
   cout << "p8:\t\t\t\t\t" << p8 << endl;
   cout << "alpha:\t\t\t\t" << alpha << endl;
   cout << "beta:\t\t\t\t" << beta << endl;
   cout << "setXAngle:\t\t\t\t\t" << setXAngle << endl;
   cout << "newXAngle:\t\t\t\t\t" << newXAngle << endl;
   cout << "setZAngle:\t\t\t\t\t" << setZAngle << endl;
   cout << "newZAngle:\t\t\t\t\t" << newZAngle << endl;
   cout << "uniformXDist:\t\t\t\t\t" << uniformXDist << endl;
   cout << "xSpace:\t\t\t\t\t\t" << xSpace << endl;
   cout << "uniformYDist:\t\t\t\t\t" << uniformYDist << endl;
   cout << "ySpace:\t\t\t\t\t\t" << ySpace << endl;
   cout << "uniformZDist:\t\t\t\t\t" << uniformZDist << endl;
   cout << "zSpace:\t\t\t\t\t\t" << zSpace << endl;

}

// Load method
void FlakeCreator::load(float* filledVolume, float* xArea, float* yArea, float* zArea, float*
percentFlakeThickness, float* percentThickness, float* otherFlakeThickness, float* p1, float*
p2, float* p3, float* p4, float* q1p5, float* q2p6, float* q3p7, float* p8, int* circlePoints, float*
alpha, float* beta, int* haveXAngle, int* elongated, float* setXAngle, float* newXAngle, float*
setZAngle, float* newZAngle, float* uniformXDist, float* xSpace, float* uniformYDist, float*
ySpace, float* uniformZDist, float* zSpace)
{
   ifstream config ("Config.txt");
   string line;
   if(config.is_open()) {
      // Skip the first 3 which are printing varaibles
      for(int i = 0; i < 3; i++)
         getline(config,line);
      getline(config,line);
      *filledVolume = convertStringTofloat(line);
      getline(config,line);
      *xArea = convertStringTofloat(line);
```

```
getline(config,line);
*yArea = convertStringTofloat(line);
getline(config,line);
*zArea = convertStringTofloat(line);
getline(config,line);
*percentFlakeThickness = convertStringTofloat(line);
getline(config,line);
*percentThickness = convertStringTofloat(line);
getline(config,line);
*otherFlakeThickness = convertStringTofloat(line);
getline(config,line);
*p1 = convertStringTofloat(line);
getline(config,line);
*p2 = convertStringTofloat(line);
getline(config,line);
*p3 = convertStringTofloat(line);
getline(config,line);
*p4 = convertStringTofloat(line);
getline(config,line);
*q1p5 = convertStringTofloat(line);
getline(config,line);
*q2p6 = convertStringTofloat(line);
getline(config,line);
*q3p7 = convertStringTofloat(line);
getline(config,line);
*p8 = convertStringTofloat(line);
getline(config,line);
*circlePoints = convertStringTofloat(line);
getline(config,line);
*alpha = convertStringTofloat(line);
getline(config,line);
*beta = convertStringTofloat(line);
getline(config,line);
*haveXAngle = convertStringTofloat(line);
getline(config,line);
*elongated = convertStringTofloat(line);
getline(config,line);
*setXAngle = convertStringTofloat(line);
getline(config,line);
*newXAngle = convertStringTofloat(line);
getline(config,line);
*setZAngle = convertStringTofloat(line);
getline(config,line);
*newZAngle = convertStringTofloat(line);
```

```
        getline(config,line);
        *uniformXDist = convertStringTofloat(line);
        getline(config,line);
        *xSpace = convertStringTofloat(line);
        getline(config,line);
        *uniformYDist = convertStringTofloat(line);
        getline(config,line);
        *ySpace = convertStringTofloat(line);
        getline(config,line);
        *uniformZDist = convertStringTofloat(line);
        getline(config,line);
        *zSpace = convertStringTofloat(line);
        getline(config,line);
        config.close();
    } else {
        cout << "Failed to open config file, continuing with defaults" << endl;
    }
}

float FlakeCreator::convertStringTofloat(string line)
{
    float toReturn = 0.0;
    stringstream convert(line);
    convert >> toReturn;
    return toReturn;
}

//the Getter Methods
float FlakeCreator::getXSpace()
{
    return xSpace;
}
float FlakeCreator::getYSpace()
{
    return ySpace;
}
float FlakeCreator::getZSpace()
{
    return zSpace;
}

float FlakeCreator::getUniformXDist()
{
    return uniformXDist;
```

```
}
float FlakeCreator::getUniformYDist()
{
   return uniformYDist;
}
float FlakeCreator::getUniformZDist()
{
   return uniformZDist;
}
```

Filename: Flake.cpp

```
// This module generates each flake's/platelet's takes each flake's
dimensions/orientation/location and generates the vertices of the rectangular flake/plateet.
// This module is called every time a flake/platelet is created.


// Protected global variables
#ifndef FLAKE_H_INCLUDED
#define FLAKE_H_INCLUDED
#include "Flake.h"
#endif
#ifndef MATH_H_INCLUDED
#define MATH_H_INCLUDED
#include <math.h>
#endif
#ifndef IOSTREAM_INCLUDED
#define IOSTREAM_INCLUDED
#include <iostream>
#endif
#ifndef FSTREAM_INCLUDED
#define FSTREAM_INCLUDED
#include <fstream>
#endif
#ifndef SSTREAM_INCLUDED
#define SSTREAM_INCLUDED
#include <sstream>
#endif
#ifndef STRING_INCLUDED
#define STRING_INCLUDED
#include <string>
#endif
```

```
#ifndef IOMANIP_INCLUDED
#define IOMANIP_INCLUDED
#include <iomanip>
#endif
#ifndef RANDOM_INCLUDED
#define RANDOM_INCLUDED
#include <random>
#endif
#define PI 3.14159

using namespace std;

Flake::Flake() {}

// The format of the initial construct is defined here for each flake/platelet
Flake::Flake(float xW, float yW, float t, float xA, float zA, float xAr, float yAr, float zAr, int cp,
float uniformxdist, float xSpce, float uniformydist, float ySpce, float uniformzdist,float zSpce)
{
   xWidth = xW;
   yWidth = yW;
   thickness = t;
   xAngle = xA;
   zAngle = zA;
   xArea = xAr;
   yArea = yAr;
   zArea = zAr;
   xPosition = 0;
   yPosition = 0;
   zPosition = 0;
   circlePoints = cp;
   minXOriginPoint = 0;
   maxXOriginPoint = 0;
   minYOriginPoint = 0;
   maxYOriginPoint = 0;
   minZOriginPoint = 0;
   maxZOriginPoint = 0;
   seed = rand();

   // We based dimensions on reported dimensions from pigment suppliers.  These dimensions
assume flakes/platelets are circular, not rectangular.
   // In this simulation, flakes/platelets are rectangular, so a conversion is needed
   generateApproximateCircle();
   generateRotation();
   uniformXDist = uniformxdist;
```

```
   xSpace = xSpce;
   uniformYDist = uniformydist;
   ySpace = ySpce;
   uniformZDist = uniformzdist;
   zSpace = zSpce;
   vector<vector<float> > points(3, vector<float>(circlePoints));
   placedPoints = points;
}

// Deconstructor to save memory
Flake::~Flake()
{
   originPoints.clear();
   placedPoints.clear();
}



void Flake::generateApproximateCircle()
{
   // Outer points of the flake/platelet are placed
   vector<vector<float> > points(3, vector<float>(circlePoints));
   for(int i = 0; i < circlePoints; i++) {
      points[0][i] = sqrt(2.0)*xWidth/2 * cos((360.0*((float)i/(float)circlePoints))*PI/180.0-
PI/4.0);
      points[1][i] = sqrt(2.0)*yWidth/2 * sin((360.0*((float)i/(float)circlePoints))*PI/180.0-PI/4.0);
      points[2][i] = 0.0;
   }
   originPoints = points;
}

void Flake::generateRotation()
{

   // In order to rotate outer points about x- and z- axes, given angles of rotation must be used
within rotational matrices.
   float xCos = cos(xAngle*PI/180.0);
   float xSin = sin(xAngle*PI/180.0);
   float zCos = cos(zAngle*PI/180.0);
   float zSin = sin(zAngle*PI/180.0);
   float xRotation[3][3] = {{1,0,0},{0,xCos,-xSin},{0,xSin,xCos}};
   float zRotation[3][3] = {{zCos,-zSin,0},{zSin,zCos,0},{0,0,1}};
   float totalRotation[3][3] = {{0,0,0},{0,0,0},{0,0,0}};

   // Generate the combined rotation
```

```
    for(int i = 0; i < 3; i++) {
        for(int j = 0; j < 3; j++) {
            totalRotation[i][j] = 0.0;
            for(int k = 0; k < 3; k++) {
                totalRotation[i][j] += zRotation[i][k] * xRotation[k][j];
            }
        }
    }

    float rotatedOuterPoints[3][circlePoints];
    for(int i = 0; i < 3; i++) {
        for(int j = 0; j < circlePoints; j++) {
            rotatedOuterPoints[i][j] = 0.0;
            for(int k = 0; k < 3; k++) {
                rotatedOuterPoints[i][j] += totalRotation[i][k] * originPoints[k][j];
            }
        }
    }

    for(int i = 0; i < 3; i++) {
        for(int j = 0; j < circlePoints; j++) {
            originPoints[i][j] = rotatedOuterPoints[i][j];
            if(i == 0) {
                if(originPoints[i][j] > originPoints[i][maxXOriginPoint])
                    maxXOriginPoint = j;
                if(originPoints[i][j] < originPoints[i][minXOriginPoint])
                    minXOriginPoint = j;
            }
            if(i == 1) {
                if(originPoints[i][j] > originPoints[i][maxYOriginPoint])
                    maxYOriginPoint = j;
                if(originPoints[i][j] < originPoints[i][minYOriginPoint])
                    minYOriginPoint = j;
            }
            if(i == 2) {
                if(originPoints[i][j] > originPoints[i][maxZOriginPoint])
                    maxZOriginPoint = j;
                if(originPoints[i][j] < originPoints[i][minZOriginPoint])
                    minZOriginPoint = j;
            }
        }
    }
}
```

```
// Generate X position of the center of the flake/platelet
void Flake::generateXPosition()
{
   // Generate the position within in the given volume.
   xPosition = xArea*((float)rand_r(&seed)/(float)RAND_MAX);

   // Add the position change to the points to create the placed points
   for(int i = 0; i < circlePoints; i++) {
      placedPoints[0][i] = originPoints[0][i] + xPosition;
   }
}

//uniform x Distribution
void Flake::generateXPosition(float x)
{
   xPosition = x;

   // Add the position change to the points to create the placed points
   for(int i = 0; i < circlePoints; i++) {
      placedPoints[0][i] = originPoints[0][i] + xPosition;
   }

}

// Generate Y position of the center of the flake/platelet
void Flake::generateYPosition()
{
   // Create the random position.
   yPosition = yArea*((float)rand_r(&seed)/(float)RAND_MAX);


   // Add the position change to the points to create the placed points
   for(int i = 0; i < circlePoints; i++) {
      placedPoints[1][i] = originPoints[1][i] + yPosition;
   }
}

//uniform y Distribution
void Flake::generateYPosition(float y)
{

   yPosition = y;
   // Add the position change to the points to create the placed points
   for(int i = 0; i < circlePoints; i++) {
```

```
      placedPoints[1][i] = originPoints[1][i] + yPosition;
   }

}

// Generate Z position of the center of the flake/platelet
void Flake::generateZPosition()
{
   // Create the random position.
   zPosition = zArea*((float)rand_r(&seed)/(float)RAND_MAX);

   // Add the position change to the points to create the placed points
   for(int i = 0; i < circlePoints; i++) {
      placedPoints[2][i] = originPoints[2][i] + zPosition;
   }
}

//uniform z Distribution
void Flake::generateZPosition(float z)
{
   zPosition = z;

   // Add the position change to the points to create the placed points
   for(int i = 0; i < circlePoints; i++) {
      placedPoints[2][i] = originPoints[2][i] + zPosition;
   }

}




// Set up operator so the flakes/platelets can be sorted from largest to smallest.  Want to add
largest flakes to the volume first, as smaller flakes can fit into open volumes easier.
bool Flake::operator<( const Flake& flake ) const
{
   return xWidth < flake.xWidth;
}

// Print out some quick data about the flake
void Flake::print()
{
   cout << endl;
   cout << "xWidth:\t\t" << xWidth << endl;
```

```
    cout << "yWidth:\t\t" << yWidth << endl;
    cout << "thickness:\t" << thickness << endl;
    cout << "xAngle:\t\t" << xAngle << endl;
    cout << "zAngle:\t\t" << zAngle << endl;
    cout << "xPosition:\t" << xPosition << endl;
    cout << "yPosition:\t" << yPosition << endl;
    cout << "zPosition:\t" << zPosition << endl;
    cout << "originPoints:" << endl;
    for(int i = 0; i < 3; i++) {
        for(int j = 0; j < circlePoints; j++) {
            cout << originPoints[i][j] << "\t";
        }
        cout << endl;
    }
    cout << "placedPoints:" << endl;
    for(int i = 0; i < 3; i++) {
        for(int j = 0; j < circlePoints; j++) {
            cout << placedPoints[i][j] << "\t";
        }
        cout << endl;
    }
    cout << "xMin: " << getMinX() << endl;
    cout << "xMax: " << getMaxX() << endl;
    cout << "yMin: " << getMinY() << endl;
    cout << "yMax: " << getMaxY() << endl;
    cout << "zMin: " << getMinZ() << endl;
    cout << "zMax: " << getMaxZ() << endl;
}

// Getter methods for the flake
float Flake::getXWidth()
{
    return xWidth;
}
float Flake::getYWidth()
{
    return yWidth;
}
float Flake::getThickness()
{
    return thickness;
}
float Flake::getXAngle()
{
```

```
    return xAngle;
}
float Flake::getZAngle()
{
    return zAngle;
}
float Flake::getXArea()
{
    return xArea;
}
float Flake::getYArea()
{
    return yArea;
}
float Flake::getZArea()
{
    return zArea;
}
float Flake::getXPosition()
{
    return xPosition;
}
float Flake::getYPosition()
{
    return yPosition;
}
float Flake::getZPosition()
{
    return zPosition;
}
float Flake::getCirclePoints()
{
    return circlePoints;
}
vector<vector<float> > Flake::getPlacedPoints()
{
    return placedPoints;
}
float Flake::getMinX()
{
    return placedPoints[0][minXOriginPoint];
}
float Flake::getMaxX()
{
```

```
   return placedPoints[0][maxXOriginPoint];
}
float Flake::getMinY()
{
   return placedPoints[1][minYOriginPoint];
}
float Flake::getMaxY()
{
   return placedPoints[1][maxYOriginPoint];
}
float Flake::getMinZ()
{
   return placedPoints[2][minZOriginPoint];
}
float Flake::getMaxZ()
{
   return placedPoints[2][maxZOriginPoint];
}
```

Filename: FlakeBox.cpp

```
// This module is the flake/platelet intersection detection module.  A series of bound boxes are
created throughout the simulated volume to localize the intersection checks and reduce
// the number of intersection checks that must be run.  This module pulls from
TriTriIntersection.cpp, which includes the intersection detection method put forth by Tomas
Moller.


// Protected global variables
#ifndef FLAKEBOX_H_INCLUDED
#define FLAKEBOX_H_INCLUDED
#include "FlakeBox.h"
#endif
#ifndef TRITRIINTERSECTION_INCLUDED
#define TRITRIINTERSECTION_INCLUDED
#include "TriTriIntersection.cpp"
#endif

using namespace std;

FlakeBox::FlakeBox() {}
```

```
// Initial constructor
FlakeBox::FlakeBox(float xMin, float yMin, float zMin, float xMax, float yMax, float zMax)
{
   // Min and max corner points make up the geometry
   xBounds[0] = xMin;
   xBounds[1] = xMax;
   yBounds[0] = yMin;
   yBounds[1] = yMax;
   zBounds[0] = zMin;
   zBounds[1] = zMax;
}

// Calculate if there is a intersection between a flake and a box
bool FlakeBox::boxIntersection(Flake flake)
{

   // Calculate the bounding box intersection first to see if there is even a chance they intersect
   if(!(xBounds[1] > flake.getMinX() && xBounds[0] < flake.getMaxX() && yBounds[1] >
flake.getMinY() && yBounds[0] < flake.getMaxY() && zBounds[1] > flake.getMinZ() &&
zBounds[0] < flake.getMaxZ())) {
      return false;
   }

   // The following size sections are all checking if the flake is on a particular side of the box
then you only have to calculate 1 side of intersection. This should optimize the process of
intersection checking.

   // If the flake is at a greater xposition than the box
   if(flake.getXPosition() > xBounds[1]) {
      // Then create the side wall of the box
      float p1[3] = {xBounds[1],yBounds[0],zBounds[0]};
      float p2[3] = {xBounds[1],yBounds[0],zBounds[1]};
      float p3[3] = {xBounds[1],yBounds[1],zBounds[1]};
      float p4[3] = {xBounds[1],yBounds[1],zBounds[0]};
      // Create a focal points of the flake that points will be based off of
      float flakeFocal[3] =
{flake.getPlacedPoints()[0][0],flake.getPlacedPoints()[1][0],flake.getPlacedPoints()[2][0]};
      for(int i = 0 ; i < flake.getCirclePoints()-2; i++) {
         // Create the other two points of the triangle
         float fp1[3] =
{flake.getPlacedPoints()[0][i+1],flake.getPlacedPoints()[1][i+1],flake.getPlacedPoints()[2][i+1]};
         float fp2[3] =
{flake.getPlacedPoints()[0][i+2],flake.getPlacedPoints()[1][i+2],flake.getPlacedPoints()[2][i+2]};
```

```
      // Check the flake triangle with the two triangles that make the box wall
      if(NoDivTriTriIsect(p1,p2,p3,flakeFocal,fp1,fp2) ||
NoDivTriTriIsect(p1,p3,p4,flakeFocal,fp1,fp2)) {
        return true;
      }
    }
  }
  // If the flake is at a lesser xposition than the box
  if(flake.getXPosition() < xBounds[0]) {
    // Then create the side wall of the box
    float p1[3] = {xBounds[0],yBounds[0],zBounds[0]};
    float p2[3] = {xBounds[0],yBounds[0],zBounds[1]};
    float p3[3] = {xBounds[0],yBounds[1],zBounds[1]};
    float p4[3] = {xBounds[0],yBounds[1],zBounds[0]};
    // Create a focal points of the flake that points will be based off of
    float flakeFocal[3] =
{flake.getPlacedPoints()[0][0],flake.getPlacedPoints()[1][0],flake.getPlacedPoints()[2][0]};
    for(int i = 0 ; i < flake.getCirclePoints()-2; i++) {
      // Create the other two points of the triangle
      float fp1[3] =
{flake.getPlacedPoints()[0][i+1],flake.getPlacedPoints()[1][i+1],flake.getPlacedPoints()[2][i+1]};
      float fp2[3] =
{flake.getPlacedPoints()[0][i+2],flake.getPlacedPoints()[1][i+2],flake.getPlacedPoints()[2][i+2]};
      // Check the flake triangle with the two triangles that make the box wall
      if(NoDivTriTriIsect(p1,p2,p3,flakeFocal,fp1,fp2) ||
NoDivTriTriIsect(p1,p3,p4,flakeFocal,fp1,fp2)) {
        return true;
      }
    }
  }
  // If the flake is at a greater yposition than the box
  if(flake.getYPosition() > yBounds[1]) {
    // Then create the side wall of the box
    float p1[3] = {xBounds[0],yBounds[1],zBounds[0]};
    float p2[3] = {xBounds[1],yBounds[1],zBounds[0]};
    float p3[3] = {xBounds[0],yBounds[1],zBounds[1]};
    float p4[3] = {xBounds[1],yBounds[1],zBounds[1]};
    // Create a focal points of the flake that points will be based off of
    float flakeFocal[3] =
{flake.getPlacedPoints()[0][0],flake.getPlacedPoints()[1][0],flake.getPlacedPoints()[2][0]};
    for(int i = 0 ; i < flake.getCirclePoints()-2; i++) {
      // Create the other two points of the triangle
      float fp1[3] =
{flake.getPlacedPoints()[0][i+1],flake.getPlacedPoints()[1][i+1],flake.getPlacedPoints()[2][i+1]};
```

```
      float fp2[3] =
{flake.getPlacedPoints()[0][i+2],flake.getPlacedPoints()[1][i+2],flake.getPlacedPoints()[2][i+2]};
      // Check the flake triangle with the two triangles that make the box wall
      if(NoDivTriTriIsect(p1,p2,p3,flakeFocal,fp1,fp2) ||
NoDivTriTriIsect(p2,p3,p4,flakeFocal,fp1,fp2)) {
        return true;
      }
    }
  }
  // If the flake is at a lesser yposition than the box
  if(flake.getYPosition() < yBounds[0]) {
    // Then create the side wall of the box
    float p1[3] = {xBounds[0],yBounds[0],zBounds[0]};
    float p2[3] = {xBounds[1],yBounds[0],zBounds[0]};
    float p3[3] = {xBounds[0],yBounds[0],zBounds[1]};
    float p4[3] = {xBounds[1],yBounds[0],zBounds[1]};
    // Create a focal points of the flake that points will be based off of
    float flakeFocal[3] =
{flake.getPlacedPoints()[0][0],flake.getPlacedPoints()[1][0],flake.getPlacedPoints()[2][0]};
    for(int i = 0 ; i < flake.getCirclePoints()-2; i++) {
      // Create the other two points of the triangle
      float fp1[3] =
{flake.getPlacedPoints()[0][i+1],flake.getPlacedPoints()[1][i+1],flake.getPlacedPoints()[2][i+1]};
      float fp2[3] =
{flake.getPlacedPoints()[0][i+2],flake.getPlacedPoints()[1][i+2],flake.getPlacedPoints()[2][i+2]};
      // Check the flake triangle with the two triangles that make the box wall
      if(NoDivTriTriIsect(p1,p2,p3,flakeFocal,fp1,fp2) ||
NoDivTriTriIsect(p2,p3,p4,flakeFocal,fp1,fp2)) {
        return true;
      }
    }
  }
  // If the flake is at a greater zposition than the box
  if(flake.getZPosition() > zBounds[1]) {
    // Then create the side wall of the box
    float p1[3] = {xBounds[1],yBounds[1],zBounds[1]};
    float p2[3] = {xBounds[1],yBounds[0],zBounds[1]};
    float p3[3] = {xBounds[0],yBounds[1],zBounds[1]};
    float p4[3] = {xBounds[0],yBounds[0],zBounds[1]};
    // Create a focal points of the flake that points will be based off of
    float flakeFocal[3] =
{flake.getPlacedPoints()[0][0],flake.getPlacedPoints()[1][0],flake.getPlacedPoints()[2][0]};
    for(int i = 0 ; i < flake.getCirclePoints()-2; i++) {
      // Create the other two points of the triangle
```

```
         float fp1[3] =
{flake.getPlacedPoints()[0][i+1],flake.getPlacedPoints()[1][i+1],flake.getPlacedPoints()[2][i+1]};
         float fp2[3] =
{flake.getPlacedPoints()[0][i+2],flake.getPlacedPoints()[1][i+2],flake.getPlacedPoints()[2][i+2]};
         // Check the flake triangle with the two triangles that make the box wall
         if(NoDivTriTriIsect(p1,p2,p3,flakeFocal,fp1,fp2) ||
NoDivTriTriIsect(p2,p3,p4,flakeFocal,fp1,fp2)) {
            return true;
         }
      }
   }
   // If the flake is at a lesser zposition than the box
   if(flake.getZPosition() < zBounds[0]) {
      // Then create the side wall of the box
      float p1[3] = {xBounds[1],yBounds[1],zBounds[0]};
      float p2[3] = {xBounds[1],yBounds[0],zBounds[0]};
      float p3[3] = {xBounds[0],yBounds[1],zBounds[0]};
      float p4[3] = {xBounds[0],yBounds[0],zBounds[0]};
      // Create a focal points of the flake that points will be based off of
      float flakeFocal[3] =
{flake.getPlacedPoints()[0][0],flake.getPlacedPoints()[1][0],flake.getPlacedPoints()[2][0]};
      for(int i = 0 ; i < flake.getCirclePoints()-2; i++) {
         // Create the other two points of the triangle
         float fp1[3] =
{flake.getPlacedPoints()[0][i+1],flake.getPlacedPoints()[1][i+1],flake.getPlacedPoints()[2][i+1]};
         float fp2[3] =
{flake.getPlacedPoints()[0][i+2],flake.getPlacedPoints()[1][i+2],flake.getPlacedPoints()[2][i+2]};
         // Check the flake triangle with the two triangles that make the box wall
         if(NoDivTriTriIsect(p1,p2,p3,flakeFocal,fp1,fp2) ||
NoDivTriTriIsect(p2,p3,p4,flakeFocal,fp1,fp2)) {
            return true;
         }
      }
   }
   return false;
}

// Calculate if there is a intersection between a flake and the flakes in the box
bool FlakeBox::flakeIntersection(Flake flake)
{
   for(int i = 0; i < flakes.size(); i++) { // Loop through every flake
      // Bounding box check between the flakes
```

```
      if(flakes.at(i).getMaxX() > flake.getMinX() && flakes.at(i).getMinX() < flake.getMaxX() &&
flakes.at(i).getMaxY() > flake.getMinY() && flakes.at(i).getMinY() < flake.getMaxY() &&
flakes.at(i).getMaxZ() > flake.getMinZ() && flakes.at(i).getMinZ() < flake.getMaxZ()) {
         // There boxes intersected so now calculate the more intense check
         if(flakeToFlakeIntersection(flake,flakes.at(i))) {
            return true;
         }
      }
   }

   return false;
}

// The final and ultimate check between flakes/platelets.  Each flake/platelet is broken down
into a series of triangles.  Each triangle is checked for an intersection with all other triangles in
its local box.
// If a failure is detected, a "true" is returned to the main algorithm and a new location for the
current flake/platelet is generated.

bool FlakeBox::flakeToFlakeIntersection(Flake flake1, Flake flake2)
{
   // Get the origin for the triangles from the flake
   float flakeFocal1[3] =
{flake1.getPlacedPoints()[0][0],flake1.getPlacedPoints()[1][0],flake1.getPlacedPoints()[2][0]};
   float flakeFocal2[3] =
{flake2.getPlacedPoints()[0][0],flake2.getPlacedPoints()[1][0],flake2.getPlacedPoints()[2][0]};
   for(int i = 0 ; i < flake1.getCirclePoints() - 2; i++) { // Find the other two points of that triangle
      float fp1[3] =
{flake1.getPlacedPoints()[0][i+1],flake1.getPlacedPoints()[1][i+1],flake1.getPlacedPoints()[2][i+1
]};
      float fp2[3] =
{flake1.getPlacedPoints()[0][i+2],flake1.getPlacedPoints()[1][i+2],flake1.getPlacedPoints()[2][i+2
]};
      for(int j = 0; j < flake2.getCirclePoints() - 2; j++) {
         float fp3[3] =
{flake2.getPlacedPoints()[0][j+1],flake2.getPlacedPoints()[1][j+1],flake2.getPlacedPoints()[2][j+1
]};
         float fp4[3] =
{flake2.getPlacedPoints()[0][j+2],flake2.getPlacedPoints()[1][j+2],flake2.getPlacedPoints()[2][j+2
]};

         // Triangles are generated.  Next intersections are analyzed.
         if(NoDivTriTriIsect(flakeFocal1,fp1,fp2,flakeFocal2,fp3,fp4)) {
            return true;
```

```
         }
      }
   }
   return false;
}

// Add a intersected flake to the box
void FlakeBox::addFlake(Flake flake)
{
   flakes.push_back(flake);
}

// Calles a deconstructor on all the flakes to save space
void FlakeBox::emptyBox()
{
   flakes.clear();
}
```

Filename: TriTriIntersection.cpp

```
/* Triangle/triangle intersection test routine,
 * by Tomas Moller, 1997.
 * See article "A Fast Triangle-Triangle Intersection Test",
 * Journal of Graphics Tools, 2(2), 1997
```

Filename: VolumeOfBoxes.cpp

```
// This module is used to calculate the volume of the bound boxes based on the size of the largest flakes used.

// Protected global variables
#ifndef VOLUMEOFBOXES_H_INCLUDED
#define VOLUMEOFBOXES_H_INCLUDED
#include "VolumeOfBoxes.h"
#endif

using namespace std;

VolumeOfBoxes::VolumeOfBoxes(float xArea, float yArea, float zArea, float largestFlake)
{
```

```
   // Calculate number of boxes needed for each direction to fill space.  Box size is based on
largest flake.
   xBoxes = ceil(xArea/largestFlake);
   yBoxes = ceil(yArea/largestFlake);
   zBoxes = ceil(zArea/largestFlake);
   boxDimension = largestFlake;
   cout << "boxDimension:\t" << boxDimension << endl;
   cout << "xBoxs:\t\t\t" << xBoxes << endl;
   cout << "yBoxs:\t\t\t" << yBoxes << endl;
   cout << "zBoxs:\t\t\t" << zBoxes << endl;


   // Create Boxes
   vector<vector<vector<FlakeBox> > > boxes(xBoxes, vector<vector<FlakeBox> >(yBoxes,
vector<FlakeBox>(zBoxes)));
   for(int x = 0; x < xBoxes; x++) {
      for(int y = 0; y < yBoxes; y++) {
         for(int z = 0; z < zBoxes; z++) {
            float xMin = x*boxDimension;
            float yMin = y*boxDimension;
            float zMin = z*boxDimension;
            float xMax = (1+x)*boxDimension;
            float yMax = (1+y)*boxDimension;
            float zMax = (1+z)*boxDimension;
            // Make points out of the float values and put into box arg
            boxes[x][y][z] = FlakeBox(xMin,yMin,zMin,xMax,yMax,zMax); // Construct the box
instead
         }
      }
   }
   // Not pointer, new instance
   flakeBoxes = boxes;
   boxes.clear();


}

// Blank deconstructor
VolumeOfBoxes::~VolumeOfBoxes()
{

}

// Check to get the relevant boxes for the flakes for intersection testing
```

```
vector<FlakeBox*> VolumeOfBoxes::relevantBoxes(Flake flake)
{



   vector<FlakeBox*> toReturn;


   // Find the box the flake is actually in
   int boxX = floor(flake.getXPosition() / boxDimension);
   int boxY = floor(flake.getYPosition() / boxDimension);
   int boxZ = floor(flake.getZPosition() / boxDimension);
   // Add the box for the array of relevant boxes


   toReturn.push_back(&flakeBoxes.at(boxX).at(boxY).at(boxZ));
   // loop through the adjacent


   for(int x = -1; x < 2; x++) {
      for(int y = -1; y < 2; y++) {
         for(int z = -1; z < 2; z++) {
            // Here do the adding to the center box coords
            int bX = x + boxX;
            int bY = y + boxY;
            int bZ = z + boxZ;

            // Check if box is less than 0 or one of its dimensions are larger than the number of
boxes for that dimension
            if(bX >= 0 && bY >= 0 && bZ >= 0 && bX < xBoxes && bY < yBoxes && bZ < zBoxes) {
               // Grab the box from the array and check it
               // If it intersects add it to the return

               if(flakeBoxes.at(bX).at(bY).at(bZ).boxIntersection(flake)) {
                  toReturn.push_back(&flakeBoxes.at(bX).at(bY).at(bZ));
               }

            }

         }

      }

   }
```

```
    return toReturn;

}

// Starts a chain of calling deconstructors to save memory
void VolumeOfBoxes::emptyBoxes()
{
    for(int x = 0; x < xBoxes; x++) {
        for(int y = 0; y < yBoxes; y++) {
            for(int z = 0; z < zBoxes; z++) {
                flakeBoxes[x][y][z].emptyBox();
            }
        }
    }
}
```

Filename: SaveFlakes.cpp

```
// This module is used to output the flake/platelet matrices in specific file formats for certain simulation platforms.

// Protected global variables
#ifndef IOSTREAM_INCLUDED
#define IOSTREAM_INCLUDED
#include <iostream>
#endif
#ifndef FSTREAM_INCLUDED
#define FSTREAM_INCLUDED
#include <fstream>
#endif
#ifndef SSTREAM_INCLUDED
#define SSTREAM_INCLUDED
#include <sstream>
#endif
#ifndef STRING_INCLUDED
#define STRING_INCLUDED
#include <string>
#endif
#ifndef IOMANIP_INCLUDED
#define IOMANIP_INCLUDED
#include <iomanip>
#endif
```

```
void saveFlakeDataPoints(vector<Flake> flakes)
{
    // Open a stream to the file or create and open, delete anything inside of it
    ofstream out ("FlakeDataPoints.txt", ios::out | ios::trunc);
    if (out.is_open()) {
        // Never use scientific notation and use a precision of 9
        out << setiosflags(ios::fixed) << setprecision(9);
        for(int i = 0; i < flakes.size(); i++) {
            // Use only 1 out statement to reduce overhead of the call
            out << flakes.at(i).getXWidth()<<" "<<flakes.at(i).getYWidth()<<"
"<<flakes.at(i).getThickness()<<" "<<flakes.at(i).getXPosition()-(flakes.at(i).getXArea()/2)<<"
"<<flakes.at(i).getYPosition()-(flakes.at(i).getYArea()/2)<<" "<<(flakes.at(i).getZPosition()-
(flakes.at(i).getZArea()/2))-0.020<<" "<<flakes.at(i).getXAngle()<<" "<<0<<
<<(flakes.at(i).getZAngle())*-1 << "\r\n";
        }
        out.close();
    } else cout << "Unable to open or create flake data point file" << "\r\n";
}

// Tracepro file format
void saveFlakeTextures(vector<Flake> flakes)
{
    ofstream out ("flaketexture.txt", ios::out | ios::trunc);
    if (out.is_open()) {
        // Never use scientific notation and use a precision of 9
        out << setiosflags(ios::fixed) << setprecision(9);
        out << "RepTile Texture File" << "\r\n";
        out << "Filename: C:/Users/cseubert/Documents/Flake
Orientation/Tracepro/FlakeDataPointstest.txt" << "\r\n";
        out << "13/06/04" << "\r\n";
        out << "Version:  1.0" << "\r\n";
        out << "Texture Type:  18" << "\r\n";
        for(int i = 0; i < flakes.size(); i++) {
            //Main Output
            out << 14<<" "<<0<<" "<<(flakes.at(i).getXPosition()-(flakes.at(i).getXArea()/2))*-1<<"
"<<(flakes.at(i).getYPosition()-(flakes.at(i).getYArea()/2))<<" "<<flakes.at(i).getZPosition()-
(flakes.at(i).getZArea()/2) + 0.025<<" "<<flakes.at(i).getXWidth()<<"
"<<flakes.at(i).getYWidth()<<" "<<flakes.at(i).getThickness()<<" "<<(flakes.at(i).getXAngle())*-
1<<" "<<0<<" "<<flakes.at(i).getZAngle() << "\r\n";
        }
        out.close();
    } else cout << "Unable to open or create flake texture file" << "\r\n";
}
```

```
// Optis file format
void saveFlakeSpecial(vector<Flake> flakes)
{
   ofstream out ("flakespecial.txt", ios::out | ios::trunc);
   if (out.is_open()) {
      // Never use scientific notation and use a precision of 9
      out << setiosflags(ios::fixed) << setprecision(9);
      // Useful: http://www.youtube.com/watch?v=cUv-5unQxtE
      out << flakes.size() << endl;
      for(int i = 0; i < flakes.size(); i++) {
         // Use only 1 out statement to reduce overhead of the call
         float xCos = cos(flakes.at(i).getXAngle()*PI/180.0);
         float xSin = sin(flakes.at(i).getXAngle()*PI/180.0);
         float zCos = cos(flakes.at(i).getZAngle()*PI/180.0);
         float zSin = sin(flakes.at(i).getZAngle()*PI/180.0);
         float xRotation[3][3] = {{1,0,0},{0,xCos,-xSin},{0,xSin,xCos}};
         float zRotation[3][3] = {{zCos,-zSin,0},{zSin,zCos,0},{0,0,1}};
         float totalRotation[3][3] = {{0,0,0},{0,0,0},{0,0,0}};

         // Generate the combined rotation
         for(int l = 0; l < 3; l++) {
            for(int j = 0; j < 3; j++) {
               totalRotation[l][j] = 0.0;
               for(int k = 0; k < 3; k++) {
                  totalRotation[l][j] += zRotation[l][k] * xRotation[k][j];
               }
            }
         }


         out <<flakes.at(i).getXPosition()<<" "<<flakes.at(i).getYPosition()<<" "<<"
"<<flakes.at(i).getZPosition() << " "
            << totalRotation[0][0] << " " << totalRotation[1][0]  << " " << totalRotation[2][0] << " "
            << totalRotation[0][1] << " " << totalRotation[1][1]  << " " << totalRotation[2][1] << " "
            << flakes.at(i).getXWidth() << " " << flakes.at(i).getYWidth() << " " <<
flakes.at(i).getThickness() <<endl;
      }
      out.close();
   } else cout << "Unable to open or create flake texture file" << "\r\n";

}

// File of all flake thicknesses created
```

```
void saveFlakeThicknesses(vector<Flake> flakes)
{
   // Open a stream to the file or create and open, delete anything inside of it
   ofstream out ("flakethickness.txt", ios::out | ios::trunc);
   if (out.is_open()) {
      // Never use scientific notation and use a precision of 9
      out << setiosflags(ios::fixed) << setprecision(9);
      for(int i = 0; i < flakes.size(); i++) {
         // Use only 1 out statement to reduce overhead of the call
         out << flakes.at(i).getThickness()<<"\r\n";
      }
      out.close();
   } else cout << "Unable to open or create flake data point file" << "\r\n";
}

// File of all flake vertices created
void saveFlakeVertexes(vector<Flake> flakes, int circlePoints)
{

   ofstream out ("flakevertex.obj", ios::out | ios::trunc);

   if (out.is_open()) {
      // Never use scientific notation and use a precision of 9
      out << setiosflags(ios::fixed) << setprecision(9);
      for(int i = 0; i < flakes.size(); i++) {
         for(int j = 0; j < circlePoints; j++) {
            // Use only 1 out statement to reduce overhead of the call
            out<<"v "<<(flakes.at(i).getPlacedPoints()[0][j]-flakes.at(i).getXArea()/2)<<"
"<<(flakes.at(i).getPlacedPoints()[1][j]-flakes.at(i).getYArea()/2)<<"
"<<(flakes.at(i).getPlacedPoints()[2][j]-flakes.at(i).getZArea()/2)<<" \r\r\n";
         }

      }
      for(int i = 0; i < flakes.size(); i++) {
         out << "f";
         for(int j = 0; j < circlePoints; j++) {
            out << " " << j+1+i*circlePoints << " ";
         }
         out << "\r\r\n";
      }

      out.close();
   } else cout << "Unable to open or create flake vertex file" << "\r\n";
}
```

Filename: config.txt

//Configuration file that contains all necessary microstructural data. Each line's information is listed below.

1. Boolean to print the flake point data, 1 = print data
2. Boolean to print the flake texture data 1 = print data
3. Boolean to print the flake vertex data 1 = print data
4. Fraction of the total volume to be filled with flakes
5. X area of the volume
6. Y area of the volume
7. Z area of the volume
8. Thickness of flakes created
9. Percentage of flakes with the above thickness
10. Thickness of the other flakes
11. p1
12. p2
13. p3
14. p4
15. q1/p5
16. q2/p6
17. q3/p7
18. bool/p8 (If not 0 then will use 7th order poly)
19. Number of points to make up the outer edge of the flake
20. Gamma alpha value
21. Gamma beta value
22. Boolean for the flakes to have a xangle (If 0 then xangle will be 0 if 1 then angle will be random)
23. Boolean to have the flakes elongated
24. Boolean for uniformly setting the xAngles
25. The manually set xAngle
26. Boolean for uniformly setting the zAngles
27. The manually set zAngle
28. Boolean to uniformly distribute the X spacing of flakes 1= uniform 0 = random
29. X spacing in nanometers
30. Boolean to uniformly distribute the Y spacing of flakes 1= uniform 0 = random
31. y spacing in nanometers
32. Boolean to uniformly distribute the Z spacing of flakes 1= uniform 0 = random
33. z spacing in nanometers

Appendix III-C

He-Torrance reflection model vs. FEA simulation method

To assess the accuracy of our FEA simulations, the FEA method was compared against the highly regarded He-Torrance model. A BRDF was created from a generated Gaussian surface with surface roughness parameters similar to the aluminum material modeled by He. These values were σ_{RMS} = 280 nm and τ = 1770 nm respectively. In all cases, the material was illuminated at an angle of 10°, per He's procedure.[13] The BRDF results were then compared to the results obtained by He. **Figure III-21** shows a plot of both the He-Torrance model and the measurement of a physical sample also taken by He. Also included on **Figure III-21** is the normalized BRDF created using the FEA technique presented here. The FEA technique matched the results of the He-Torrance model across the entire reflection pattern.

It should be noted that the size of the FEA simulation may need to be altered if it is to be used for significantly longer/shorter wavelength and surface roughness scales. Examples include radar and microwave scattering from large surfaces. While the FEA technique does not include any length scale assumptions like He-Torrance or other reflection models, it does require a simulation geometry that is sufficiently large to capture a statistically representative interaction of light with the surface. The exact ratio of simulation geometry size to surface roughness and/or wavelength is not known at this time.

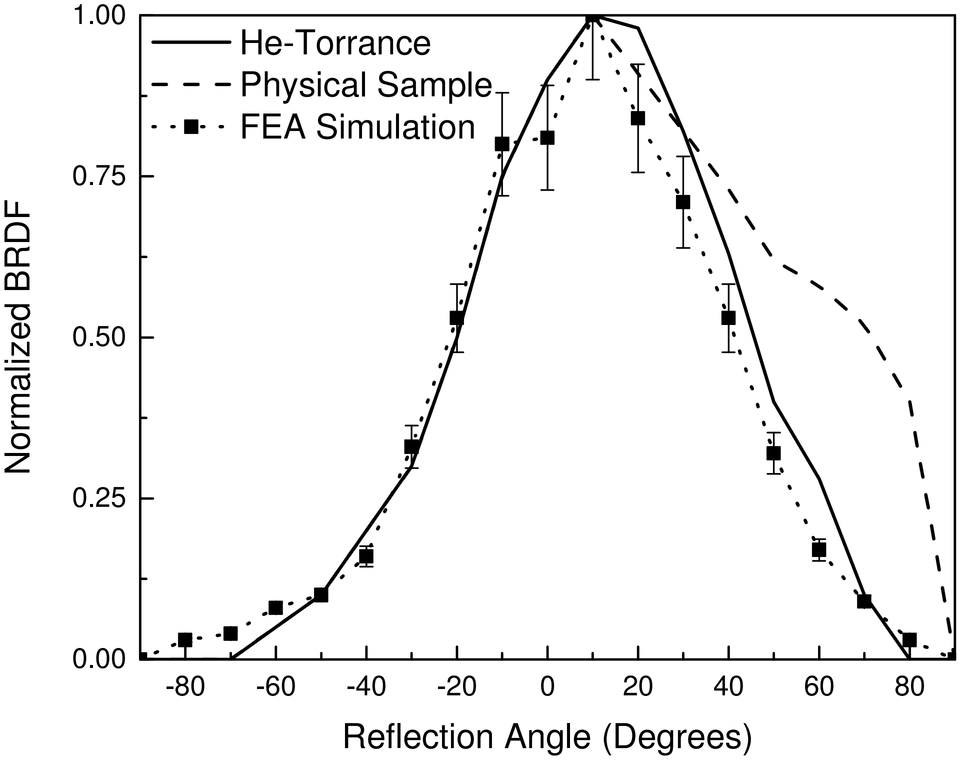

Figure III-21: A plot of the normalized BRDF reflection lobe for an aluminum surface with σ_{RMS} = 280 nm and τ = 1770 nm. The He-Torrance (considered one of the most accurate light reflection models) and physical sample data was taken from He's paper [13] that introduced his light reflection model. The FEA results were plotted against the He-Torrance model and the physical sample measurement to establish any deficiencies in the FEA simulation technique. The results appear to match well with that of the He-Torrance model. Incident angle of the incoming light was 10°. Wavelength of incoming light was 500 nm. Error bars were plotted for the FEA data only.

References

1. Ershov S, Kolchin K, Myszkowski K (2001) Rendering Pearlescent Appearance Based On Paint-Composition Modelling. EUROGRAPHICS 2001, 20:227-238.
2. Weidlich A, Wilkie A (2007) Arbitrarily layered micro-facet surfaces. Proceedings of the 5th international conference on Computer graphics and interactive techniques in Australia and Southeast Asia. ACM 1:171-178.
3. Seo MK, Kim KY, Kim DB, Lee KH (2011) Efficient representation of bidirectional reflectance distribution functions for metallic paints considering manufacturing parameters. Optical Engineering, 50:013603.
4. Ashikmin M, Premoze S, Shirley P (2000) A microfacet-based BRDF generator. Proceedings of the 27th annual conference on Computer graphics and interactive techniques. ACM Press/Addison-Wesley Publishing Co. 65-74.
5. Jakob W, Hasan M, Yan LQ, Lawrence J, Ramamoorth R, Marschner S (2014) Discrete stochastic microfacet models. ACM Transactions on Graphics (TOG), 33*:*115.
6. An KH, O’Connor B, Pipe KP, and Shtein M, (2009) Organic photodetector with spectral response tunable across the visible spectrum by means of internal optical microcavity. Organic Electronics, 10(6), 1152-1157.
7. Beaglehole D and Hunderi O (1970) Study of the interaction of light with rough metal surfaces. I. Experiment. Physical Review B 2(2): 309-321.
8. Celli V, Maradudin AA, Marvin AM, and McGurn AR (1985) Some aspects of light scattering from a randomly rough metal surface. J. Opt. Soc. Am. A. 2:2225-2239.
9. Bennett HE and Porteus JO (1961) Relation between surface roughness and specular reflectance at normal Incidence. J. Opt. Soc. Am. 51, 123-129.
10. Birkebak RC and Eckert EG. (1965) Effects of roughness of metal surfaces on angular distribution of monochromatic reflected radiation. ASME. J. Heat Transfer. 87(1):85-93.
11. Peiponen KE and Tsuboi T (1990) Metal surface roughness and optical reflectance. Optics & Laser Technology. 22(2):127-130.
12. Hongsong L and Torrance KE (2005) An experimental study of the correlation between surface roughness and light scattering for rough metallic surfaces. Proc. SPIE 5878, Advanced Characterization Techniques for Optics, Semiconductors, and Nanotechnologies II, 58780V.
13. He XD, Torrance KE, Sillion FX, Greenberg DP (1991) A comprehensive physical model for light reflection. SIGGRAPH Comput. Graph. 25(4):175-186.
14. Cook RL and Torrance KE (1982) A Reflectance Model for Computer Graphics. ACM Trans. Graph. 1:7-24.
15. Smith B (1967) Geometrical shadowing of a random rough surface. IEEE Transactions on Antennas and Propagation. 15(5):668-671.
16. Barrick D (1968) Rough Surface Scattering Based on the Specular Point Theory. IEEE Transactions on Antennas and Propagation. 16(4):449-454.
17. Tang K and Buckius RO (2001) A statistical model of wave scattering from random rough surfaces. International Journal of Heat and Mass Transfer. 44(21):4059-4073.

18. Hunderi O and Beaglehole D (1970) Study of the interaction of light with rough metal surfaces. II. Theory. Physical Review B. 2(2): 321-329.
19. Garcia N and Stoll E (1984) Monte Carlo calculation for electromagnetic-wave scattering from random rough surfaces. Physical review letters. 52(20): 1798-1801.
20. Soto-Crespo JM and Nieto-Vesperinas M (1989) Electromagnetic scattering from very rough random surfaces and deep reflection gratings. J. Opt. Soc. Am. A. 6:367-384.
21. Tang K, Dimenna RA, Buckius RO (1996) Regions of validity of the geometric optics approximation for angular scattering from very rough surfaces. International Journal of Heat and Mass Transfer. 40(1):49-59.
22. Beckmann P, Spizzichino A (1987) The scattering of electromagnetic waves from rough surfaces. Artech House, Inc., Norwood.
23. Macaskill C (1991) Geometric optics and enhanced backscatter from very rough surfaces. J. Opt. Soc. Am. A. 8:88-96.
24. Yablonovitch E (1982) Statistical ray optics. J. Opt. Soc. Am. 72:899-907.
25. He XD, Torrance KE, Sillion FX, Greenberg DP (1991) A comprehensive physical model for light reflection. SIGGRAPH Comput. Graph. 25(4):175-186.
26. Fung AK, Li Z, Chen KS (1992) Backscattering from a randomly rough dielectric surface. IEEE Transactions on Geoscience and Remote Sensing. 30(2):356-369.
27. Houchens AF and Hering RG (1967) Bidirectional reflectance of rough metal surfaces. Progress in Aeronautics and Astronautics. 20:65-90.
28. Snyder WC and Wan Z (1998) BRDF models to predict spectral reflectance and emissivity in the thermal infrared. IEEE Transactions on Geoscience and Remote Sensing, 36(1):214-225.
29. Bruce NC and Dainty JC (1991) Multiple scattering from random rough surfaces using the Kirchhoff approximation. Journal of modern optics. 38(3):579-590.
30. Bendler JT, Feldman SF, Hatti H, Hobbs SY (1998) Approximate model of diffuse reflectance from rough polymer surfaces. Journal of applied physics. 83(2):998-1004.
31. Bass FG and Moiseevich Fuks I (2013) Wave Scattering from Statistically Rough Surfaces: International Series in Natural Philosophy. Vol. 93. Elsevier, West Sussex.
32. Elfouhaily TM and Guérin CA (2004) A critical survey of approximate scattering wave theories from random rough surfaces. Waves in Random Media. 14(4):R1-R40.
33. Chen MF and Fung AK (1988) A numerical study of the regions of validity of the Kirchhoff and small-perturbation rough surface scattering models. Radio Science. 23(2):163-170.
34. Soto-Crespo JM, Friberg AT, Nieto-Vesperinas M (1990) Scattering from slightly rough random surfaces: a detailed study on the validity of the small perturbation method. JOSA A 7(7): 1185-1201.
35. Thorsos EI (1988) The validity of the Kirchhoff approximation for rough surface scattering using a Gaussian roughness spectrum. The Journal of the Acoustical Society of America 83(1):78-92.
36. Thorsos EI and Jackson DR (1989) The validity of the perturbation approximation for rough surface scattering using a Gaussian roughness spectrum. The Journal of the Acoustical Society of America. 86(1):261-277.

37. Bonomo AL, Isakson MJ, Chotiros NP (2014) Acoustic scattering from a sand layer and rock substrate with rough interfaces using the finite element method. The Journal of the Acoustical Society of America. 135(4):2298-2298.
38. Bonomo AL, Isakson MJ, Chotiros NP (2015) A comparison of finite element and analytic models of acoustic scattering from rough poroelastic interfaces. The Journal of the Acoustical Society of America. 137(4):EL235-EL240.
39. Isakson M, Yarbrough R, Chotiros N (2008) A finite element model for seafloor roughness scattering. In Proceedings of the International Symposium on Underwater Reverberation and Clutter. 173-180.
40. Isakson M, Yarbrough R, Chotiros N (2008) A finite element model for seafloor roughness scattering. In Proceedings of the International Symposium on Underwater Reverberation and Clutter. 173-180.
41. Glassner AS ed. (1989) An introduction to ray tracing. Morgan Kaufmann, Burlington.
42. Sapper ED, Hinderliter BR (2013) Computational Tools and Approaches for Design and Control of Coating and Composite Color, Appearance, and Electromagnetic Signature. Coatings 3:59-81.
43. Buxbaum, G. (Ed.). (2008). Industrial inorganic pigments. John Wiley & Sons, New York.
44. Bergström D, Powell J, Kaplan AFH (2008) The absorption of light by rough metal surfaces—A three-dimensional ray-tracing analysis. Journal of Applied Physics. 103(10):103515.
45. Garcia N and Stoll E (1984) Monte Carlo calculation for electromagnetic-wave scattering from random rough surfaces. Physical review letters. 52(20):1798.
46. Popovic Z and Popovic BD (2000) Introductory electromagnetics. 382-392, Prentice Hall, Upper Saddler River, New Jersey.
47. Neelakanta PS (1995) Handbook of electromagnetic materials: monolithic and composite versions and their applications. 501-507, CRC press New York, New York.
48. Kasarova SN, Sultanova NG, Ivanov CD, Nikolov ID (2007) Analysis of the dispersion of optical plastic materials. Optical Materials 29:1481-1490.
49. Seubert CM, Nichols ME, Frey J, Shtein M, and Thouless MD (2015) The characterization and effects of microstructure on the appearance of platelet–polymer composite coatings. Journal of Materials Science, 51(5):2259-2273.
50. Bartl J, Baranek M (2004) Emissivity of aluminum and its importance for radiometric measurement. Measurement of Physical Quantities 43:31-36.
51. Klein GA, Meyrath T (2010) Industrial color physics. Springer, New York.
52. Möller T (1997) A fast triangle-triangle intersection test. Journal of graphics tools 2:25-30.
53. Kasarova SN, Sultanova NG, Ivanov CD, Nikolov ID (2007) Analysis of the dispersion of optical plastic materials. Optical Materials 29:1481-1490.
54. Pauli H (1976) Proposed extension of the CIE recommendation on "Uniform color spaces, color difference equations, and metric color terms". JOSA 66:866-867.
55. McCamy C (1996) Observation and measurement of the appearance of metallic materials. Part I. Macro appearance. Color Research & Application 21:292-304.
56. Hass G and Waylonis JE (1961) Optical constants and reflectance and transmittance of evaporated aluminum in the visible and ultraviolet. JOSA 51(7):719-722.

57. Russ JC (1986) *Practical stereology*. Springer, New York.
58. Underwood EE (1970) Quantitative stereology. Addison-Wesley, Reading.

CHAPTER IV

Hybrid simulation of lightness changes due to microstructural differences in silver metallic paint systems

Introduction and organization

The way light interacts with surfaces is of profound importance across a range of industries such as consumer products, aerospace, and automotive. Designers can modify the appearance of materials using paint to scatter and reflect light in different ways. As industrial paints evolved into multi-functional, multi-component, multi-layer systems, designing a new color for certain products (e.g. cars) has become expensive and time consuming. The size of the platelets (width (P_w) and thickness (P_t)) and the pigment volume concentration (*PVC*) of platelets within the coating primarily determines the appearance of a metallic paint [1–5]. But, the link between changes in the physical properties of the platelets and the scattering behavior of the paint system is poorly understood, in part because paint application parameters impact microstructure. Changes to bell speed, fluid flow, spray pattern, etc. can yield two unique platelet microstructures from the same wet paint sample. As a result, it is nearly impossible to predict how a new paint system will look based on a formulation change alone unless that paint system has already been physically produced and applied.

In principle, digital design tools can help speed up the design process, but existing tools are not sophisticated enough to use beyond qualitative evaluation. In this paper, we utilize our previously discussed hybrid model to simulate how different aluminum platelet microstructures affect scattering and appearance. We use these simulations to identify specific relationships between microstructural properties and paint lightness.

This chapter is organized as follows. First, we generate full 3D microstructures and systematically vary single microstructural properties (platelet width, thickness, etc.) to quantify how such changes affect the scattering and lightness behavior of the system. Second, we import these microstructures into a hybrid ray-wave simulation and generate a complete BRDF of the microstructure under collimated illumination similar to what is used in color measurement spectrophotometers. Finally, we concluded by identifying specific relationships between lightness behavior, both in the forward and backward scattering directions, and microstructural changes in the platelet containing paint layer.

Experimental

Simulation and measurement of gonioapparent behavior of platelet arrays

To fully capture the complete microstructure of an aluminum platelet containing silver metallic paint systems, a 3D platelet array was created *in silico*. This array incorporated not only the platelets at the surface (i.e.-microfacet model) of the basecoat layer, but also the platelets contained throughout the basecoat thickness. The platelets also possess a thickness and orientation distribution based on measurements taken from physical samples in our previous study [6]. A base formulation of square platelets with widths of 15 µm and thicknesses of 0.5 µm was used, corresponding to the mean platelet dimensions in silver paint samples examined previously, as was the previously measured platelet orientation (Silver #1) [28]. Different microstructures were generated using the method described in our previous work, with platelet surface roughnesses also corresponding to those measured in that work [Paper #2 ref]. Platelet widths, thicknesses, and *PVCs* were varied to quantify how microstructural changes affect the scattering and lightness of the coating system. The specifics of each simulated microstructure are listed in **Table IV-1--Table IV-4**. The creation of these complete, 3D microstructures should allow us to identify specific correlations between microstructure and lightness. The ray trace simulations were conducted within a commercial ray optics software package (TracePro, Lambda Research Corp, Littleton, MA, USA).

To measure the gonioapparent behavior of the simulated systems in this study, a virtual goniospectrophotometer was created (**Figure IV-1)**, which consisted of a circular, collimated light source with radius of 6 mm to illuminate the system, and a spherical shell that was placed around the simulated geometry to capture all of the scattered light. The scattering and resulting BRDF data was used to quantify the amount of light reflected and the lightness of the material as a function of the illumination and observation direction.

Table IV-1: Formulation details for the simulated microstructures to quantify the effect of P_t on lightness and scattering. Factors that were changed are italicized and red. *-Refer to **Figure IV-3** for an illustration of the orientation distribution.

Orientation Distribution	**P_w (μm)**	***P_t* (μm)**	***PVC (%)***	**N_d (# per mm^3)**	**PL_t (μm)**
Standard*	15.0	*0.01*	*0.4*	~1.7M	10
Standard*	15.0	*0.10*	*4.0*	~1.7M	10
Standard*	15.0	*0.50*	*20.0*	~1.7M	10
Standard*	15.0	*1.00*	*40.0*	~1.7M	10

Table IV-2: Formulation details for thickened platelet layer samples. Samples created to increase gap size while P_w was held constant. Factors that were changed are italicized and red. *-Refer to **Figure IV-4** for an illustration of the orientation distribution.

Orientation Distribution	**P_w (μm)**	**P_t (μm)**	***PVC (%)***	**N_d (# per mm^3)**	**PL_t (μm)**
Standard*	15.0	0.5	*20*	*~1.70M*	*10*
Standard*	15.0	0.5	*13*	*~1.10M*	*15*
Standard*	15.0	0.5	*10*	*~0.85M*	*20*
Standard*	15.0	0.5	*8*	*~0.70M*	*25*
Standard*	15.0	0.5	*4*	*~0.35M*	*50*

Table IV-3: Formulation details for the simulated microstructures to quantify the effect of platelet size on scattering, lightness, and transmission. Factors that were changed are *italicized and red*. *-Refer to **Figure IV-5** for an illustration of the orientation distribution.

Orientation Distribution	P_w (µm)	P_t (µm)	*PVC* (%)	N_d (# per mm^3)	PL_t (µm)
Standard*	*2.5*	0.5	20	*~58.0M*	10
Standard*	*5.0*	0.5	20	*~15.0M*	10
Standard*	*10.0*	0.5	20	*~4.0M*	10
Standard*	*15.0*	0.5	20	*~1.7M*	10
Standard*	*20.0*	0.5	20	*~1.0M*	10

Table IV-4: Formulation details for the simulated microstructures to quantify the effect of orientation on transmission. Factors that were changed are italicized and red.

Orientation Distribution	P_w (µm)	P_t (µm)	*PVC* (%)	N_d (# per mm^3)	PL_t (µm)
Perfect	2.5	0.5	20%	~58.0M	10
Perfect	5.0	0.5	20%	~15.0M	10
Perfect	10.0	0.5	20%	~4.0M	10
Perfect	15.0	0.5	20%	~1.7M	10
Perfect	20.0	0.5	20%	~1.0M	10

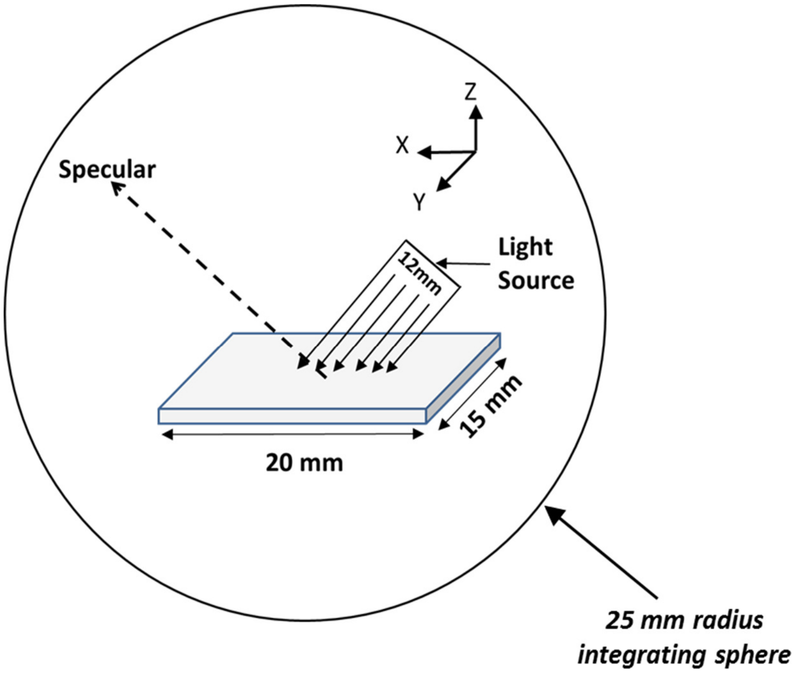

Figure IV-1: Schematic of simulation environment. Sample size is 15x20 mm, circular light source with radius of 5.5 mm located 21 mm from surface, integrating sphere of radius 25 mm surrounds the environment.

Simulation and measurement of lightness behavior of platelet arrays

A small sub-section of the BRDF was measured using a handheld spectrophotometer to quantify the color of physical samples. These spectrophotometers typically illuminate the sample from one angle (45° from normal) and then capture the scattered light at specific angles in relation to the specular angle (15°, 25°, 45°, 75°, and 110° off-specular (OS)). A diagram of this measurement is shown in **Figure IV-2**. Lightness (L^*) values were calculated for each of these angles from [7]

$$L^* = 116\,(Y/Y_n)^{1/3} - 16\,, \tag{1}$$

where Y is the measured intensity or flux of the light reflected from the sample, and Y_n is the intensity or flux of light that would be reflected at the same angle from a perfectly diffuse white reflector. This relationship is part of the CIELAB color space designed to correlate reflected light intensity to perceived color [7]. In applications with a broadband light source, Y and Y_n are one of the tristimulus values for both the sample and the diffuse white standard [8,9]. However, as simulations were conducted at a single wavelength, a simple ratio of the reflected flux was sufficient to calculate the lightness.

This handheld spectrophotometer was also virtually built within the simulation environment to capture the information from this instrument. The same circular, collimated light source with a radius of 6 mm was used to illuminate the system, and circular ports were placed at the angles noted in **Figure IV-2**. Each port was created with a 2.0 mm radius and located 36.0 mm from the center of the sample, based on dimensional measurements taken of the spectrophotometer. Each port was also shaded by a 13.0 mm long, 100% absorbing, enclosed cylinder, which prevented rays that did not exit at the prescribed angle from hitting the sensor.

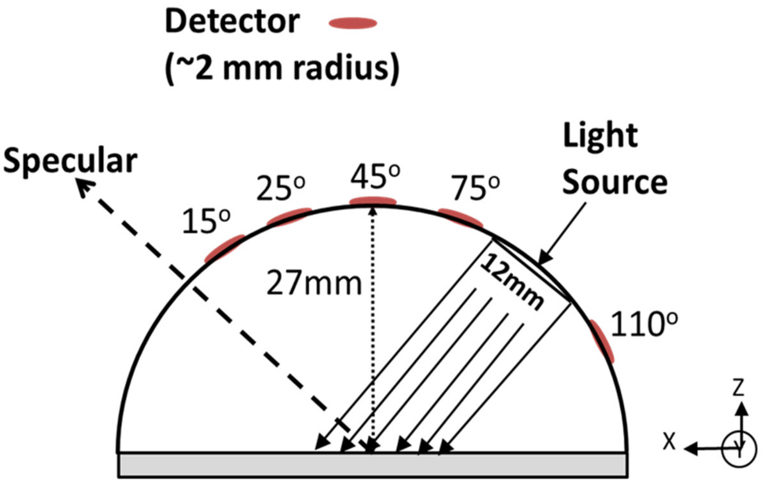

Figure IV-2: Schematic of handheld spectrophotometer measurement environment. 2 mm sensors are placed at 15°, 25°, 45°, 75°, and 110° OS in the plane of the illumination source. Collimated illumination enters from 45° from normal.

The collimated light source used to illuminate the simulated geometry cast 5M individual rays randomly distributed across the aperture towards the surface. Each ray was assigned a flux of 1 watt and a wavelength of 546 nm. The flux of each ray is not significant, as lightness calculations are performed on a relative scale. The wavelength of the light source is also not significant because aluminum platelets reflect uniformly across the visible spectrum, and no other absorptive species are present within these simulated systems. Twenty reflection events were allowed to occur for each ray before the ray was terminated. Termination was implemented to reduce computational time and because it was found that ~77% of the original power exits the system within twenty reflection events. The attenuation of power is due to absorption by the platelets and primer layer, as well as Fresnel effects [10]. Some of these attenuation events will be discussed later in this paper.

Simulated systems and appearance results

Our model that replicates the complete 3D platelet array and hybrid optics simulation environment was used to examine the relationship between platelet microstructure and appearance/lightness more thoroughly than previous studies. This was accomplished by systematically varying a single formulation property to determine its effect on the final lightness behavior of the paint system. Such a systematic examination, which is of great interest to paint formulators and designers alike, is not possible with physical samples because of confounding effects. The tool allowed us to explore how light propagates within and through the platelet structure, something not possible in standard microfacet models. Results obtained from these experiments illustrate how this tool can be used to identify which microstructural properties most greatly affect the scattering and lightness of the paint system, and also allow a designer to digitally engineer new and optimize existing paint systems.

Systematic variation of microstructure and the effect on off-specular lightness

The appearance of a metallic paint system is altered by changes to the formulation of the platelet-containing layer. Changes to the P_w, P_t, and *PVC* can all modify the microstructure, and as a result, the lightness profile. To quantify the effect of specific formulation changes on lightness, each of these platelet properties was independently varied while other properties and microstructural factors, including orientation, were held constant. The lightness behavior at the standard angles of observation—15^{o}, 25^{o}, 45^{o}, 75^{o}, and 110^{o} OS—was quantified for each of the different microstructures using the method previously listed.

Impact of P_t on microstructure and lightness

Current literature, outside of some anecdotal evidence [11], lacks detailed studies that examine the effect of P_t on the lightness and microstructure of platelet containing paint systems. In the simulations below, P_t was varied between 0.01 μm and 1.00 μm (*PVC* 0.4-40.0%), while the number density of the platelets (N_d) was held constant at ~1.7M/mm^3. Number density of the platelets was calculated using the following equation:

$$N_d = \frac{PVC}{P_w^2 * P_t} \tag{2}$$

Where *PVC*, P_w, and P_t were previously defined. Details of the experimental parameters are given in **Table IV-1** and cross sections of the microstructures are shown in **Figure IV-3A**.

The change in lightness relative to the thinnest platelet (0.01 μm) is plotted in **Figure IV-3B**. As P_t increased, the lightness increased significantly in the backscattered region, but changed little at observation angles ≤ 45° OS.

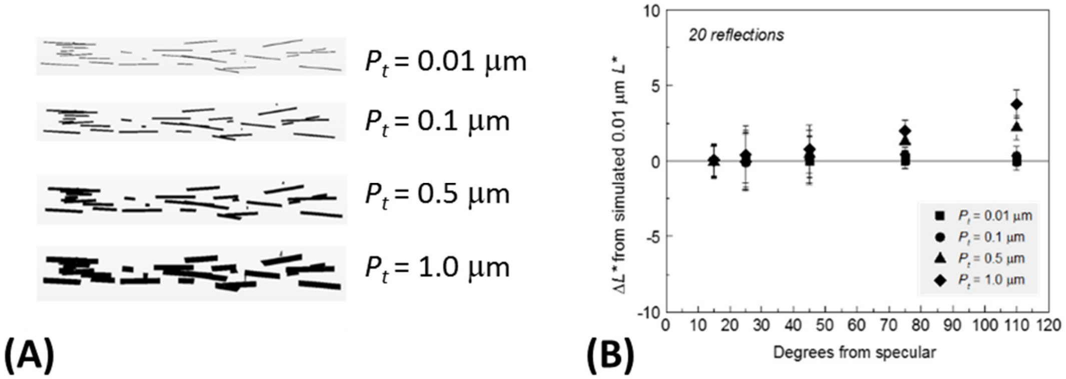

Figure IV-3: (A) Cross sectional view of simulated microstructure that examined changes to P_t. The platelet was thickened while the number of platelets placed within the simulated volume remained constant. P_w was held constant at 15 µm. (B) Change in lightness with respect to the 0.01 µm thick platelet system plotted against 15°, 25°, 45°, 75° and 110° OS observation angles. P_t only affected backscattered region (75° & 110° angles), where an increase in P_t resulted in an increase in lightness.

Impact of PVC on microstructure and lightness

The impact of *PVC* on the lightness and microstructure of platelet containing paint systems is another property that has only been mentioned briefly in the literature [12]. The *PVC* strongly impacts many coating properties, specifically the ability of the platelet layer to hide any underlying layers from incident light. To quantify this effect on the material's lightness, the *PVC* of the simulated paint system was changed by increasing PL_t from 10 to 50 µm while leaving the P_t, P_w, and total number of platelets within the system constant. PL_t variation resulted in changes to both N_d and *PVC*. Formulation details for this study are shown in **Table IV-2** and cross sections of the simulated microstructures are shown in **Figure IV-4A**.

The change in lightness relative to the highest *PVC* coating (20%) is plotted in **Figure IV-4B**. A reduction in *PVC* resulted in a significant reduction in lightness at 15^{o}, 25^{o}, and 45^{o} OS, with a lesser reduction at 75^{o} and 110^{o}. Because changes in lightness were more significant in the forward scattering direction, observers would perceive a greater lightness shift at those forward scatter angles.

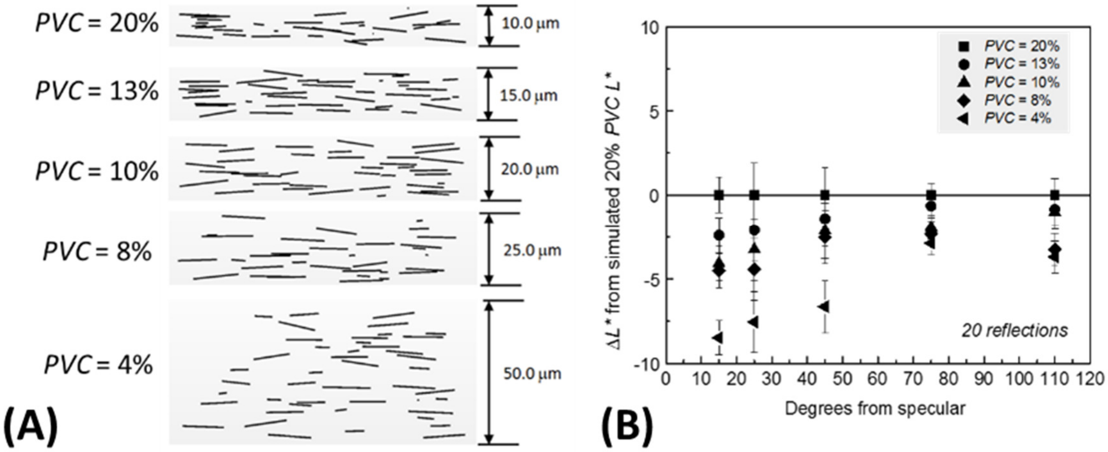

Figure IV-4: (A) Cross sectional view of simulated microstructure that examined changes to the *PVC*. The platelet layer was thickened while the number of platelets placed within the simulated volume remained constant. P_w was held constant at 15 µm. This resulted in a reduction in *PVC* without a loss of coverage. (B) Change in lightness with respect to 20% *PVC* sample plotted against 15^{o}, 25^{o}, 45^{o}, 75^{o}, and 110^{o} OS observation angles. The reduction in *PVC* had minimal statistical effect until the *PVC* was reduced by ~5x. Significant lightness changes were only observed at the 15^{o}, 25^{o}, and 45^{o} angles of observation.

Impact of P_w on Microstructure and Lightness

The relationship between P_w and lightness is the most commonly observed effect for platelet containing paint systems. Lightness has been shown to increase with platelet width [11], however, no systematic study has been performed to either quantify or understand why that is the case.

To quantify the effect of P_w on scattering, simulations were conducted where the P_w was varied between 2.5 - 20.0 μm, but the *PVC* and PL_t were held constant. This variation resulted in a significant shift in N_d. Formulation details for this study are shown in **Table IV-3** and the simulated microstructures are shown in **Figure IV-5A**.

The change in lightness relative to the system that contains 2.5 μm width platelets is shown in **Figure IV-5B**. As P_w increased, lightness increased in the forward scattering directions (15°, 25°, and 45° OS), held relatively constant at 75° OS, and decreased significantly at 110° OS, indicating that an observer would perceive both a lightening and darkening depending on their angle of observation.

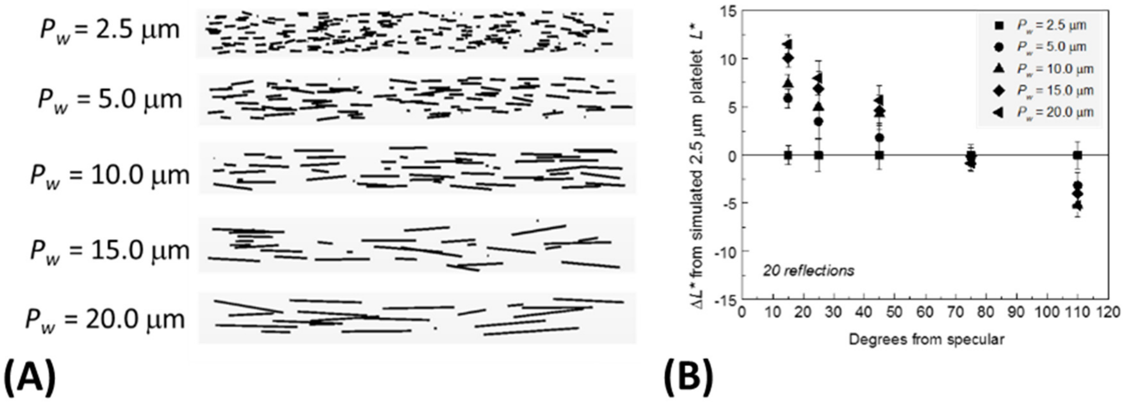

Figure IV-5: (A) Cross sectional view of simulated microstructures for P_w study. P_w ranged from 2.5 - 20.0 μm. *PVC* held constant at 20% and PL_t was held constant at 10 μm. (B) Change in lightness with respect to 2.5 μm P_w sample plotted against 15°, 25°, 45°, 75°, and 110° OS observation angles. P_w affected both forward and backward scattering behavior for different reasons. An increase in gaps as a result of reduced P_w caused a drop in lightness at 15°, 25°, and 45° OS. The increase in edge area that resulted from a reduction in P_w caused an increase in lightness at the 75° and 110° OS angles.

Transmission of light through platelet layer

In multilayered, pigmented coating systems, the opacity of a particular layer can dictate how much color of the underlying layer is transmitted to an observer. This is termed 'hiding', and is of significance when the color contrast between the two adjacent layers is especially high. Transmission of light is also important because many organic paint layers degrade when they are exposed to UV and, sometimes, visible light. The microstructure of these platelet containing paint systems plays a role in how much light is transmitted through the platelet layer.

Various microstructures were illuminated at both 45^o and 0^o from normal to determine the effect of formulation changes on the transmission of light through the platelet-containing layer. The simulated microstructures listed in **Table IV-3** were used. The orientation of platelets is also thought to affect the transmission of light within the paint system. A simulation of perfectly aligned platelets was created to quantify this effect. Formulation details for this study are shown in **Table IV-4**.

The fraction of original flux transmitted through the platelet layer is plotted as a function of P_w in **Figure IV-6**. The data suggest that not only does the P_w affect the amount of light transmitted through the entire platelet layer, but so does the incident angle and platelet orientation. The systems with a perfect alignment orientation allowed more light to pass through the basecoat layer than their standard alignment counterparts. Regardless of orientation, an increase in platelet size reduced the amount of light transmitted through the basecoat layer. In fact, at the same *PVC* the layer made with 20 μm wide platelets allowed half as much light through the platelet layer compared to the platelet layer made with 2.5 μm wide platelets.

When the angle of incidence was reduced from 45° to 0°, the dependence of transmitted flux on platelet size was equivalent, but the overall flux transmitted was less than each system's 45° incidence counterpart.

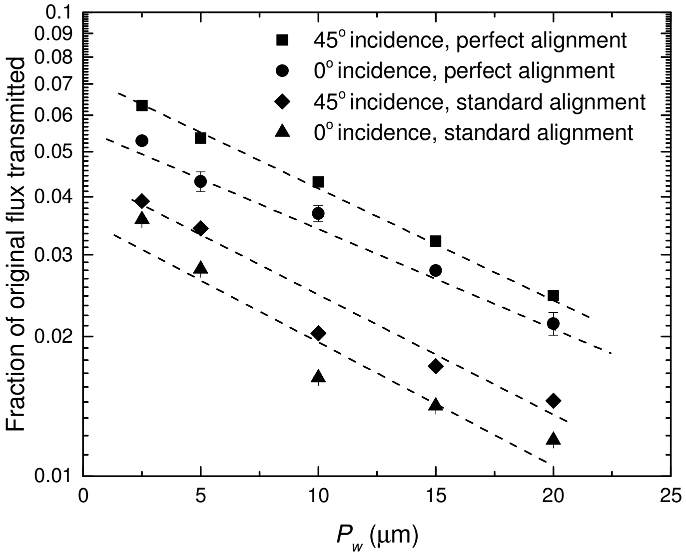

Figure IV-6: Fractional original flux transmitted through platelet layer (log) as a function of P_w. In all cases, as P_w increases, the amount of flux transmitted through the 10 μm platelet layer decreases. The 45° incident, perfect alignment system transmitted the most flux, while the 0° incident, standard alignment system transmitted the least. In all cases, a similar exponential decay was observed, as illustrated by the similar slopes observed for each plotted system. Dotted lines were added as a guide for the eye.

Discussion of simulation results and physical impact of microstructural changes

The easily controllable quantities in a coating formulation that affect the microstructure and appearance are the amount (*PVC*) and size (P_t and P_w) of the platelets in the coating. Changes in any one of these factors within other formulating constraints (hiding, solids, etc.) can sometimes lead to non-intuitive changes in the appearance of a coating due to the complex effects that these formulating variables have on the more fundamental microstructural elements of the coating: edge area and gap factor. Gap factor is a measure of the cumulative size of the gaps present between the upper surfaces of platelets, per unit length of sample [28]. The effects of the simulated formulation changes on gap factor and total edge area within the simulated volume (*EA)* are listed in **Table IV-5**. Total edge area was calculated using the following equation, where PL_t is the platelet layer thickness, PL_A is the platelet layer surface area, and *PVC* and P_w were previously defined:

$$EA = \frac{PL_t * PL_A * PVC * 4}{P_w} \tag{3}$$

The impact of changes to these fundamental microstructural features will be discussed below.

Table IV-5: P_w values used to create each unique microstructure and the gap factor value/edge area that was measured and calculated for each complete microstructure.

P_w (μm)	P_t (μm)	PVC (%)	PL_t (μm)	Gap Factor	EA (mm²)
2.5	0.50	20.0%	10.0	1.53 ± 0.05	~960
5.0	0.50	20.0%	10.0	0.89 ± 0.03	~480
10.0	0.50	20.0%	10.0	0.56 ± 0.02	~240
15.0	0.50	20.0%	10.0	0.48 ± 0.02	~160
20.0	0.50	20.0%	10.0	0.37 ± 0.01	~120
15.0	0.01	0.4%	10.0	0.48 ± 0.02	~3
15.0	0.10	4.0%	10.0	0.48 ± 0.02	~30
15.0	1.00	40.0%	10.0	0.48 ± 0.02	~300
15.0	0.50	13.0%	15.0	0.57 ± 0.02	~150
15.0	0.50	10.0%	20.0	0.79 ± 0.03	~150
15.0	0.50	8.0%	25.0	1.14 ± 0.04	~150
15.0	0.50	4.0%	50.0	1.78 ± 0.06	~150

Platelet edge effects

Paint systems that contain highly oriented metallic platelets are thought to be especially susceptible to edge effects, which are amplified for oblique illumination. We studied this behavior by changing the thickness and/or width of the platelets.

Platelet thickening increased the total edge area contained within the paint system by a proportionate amount. As was shown in **Figure IV-3**, this increased edge area only affects the measured lightness in the backscattered region (75^o and 110^o OS). No change in gap factor occurred across these systems, so it could not be a key contributor to this lightness change.

A reduction in P_w at constant *PVC* also increased the edge area contained within the total paint system volume. This, again, resulted in an increased lightness in the backscatter region, as is shown in **Figure IV-5**. However, in this case, a change in gap factor also occurred as a result of the changes to P_w. Still, it is clear from these two sets of simulations that edge area directly affects the amount of light backscattered from these paint systems.

A designer interested in modifying the amount of backscattered light must alter the edge area of the system if platelet orientation is held constant. While a ~3.8 point increase in lightness will occur for each micron added to the thickness of the platelets—assuming constant *PVC*—no change is gap factor will occur. However, a ~0.30 point reduction in lightness at 110^o OS will occur for each micron of width added to the platelets—assuming a constant *PVC*—with an added benefit of a reduction in gap factor that also occurs with increased platelet size. This would result in an increased lightness at 15^o OS—~0.66 points of lightness for every micron of platelet width added—in addition to the reduction in lightness at the 110^o OS, both of which are typically desired by color designers.

Gap factor

Gap factor has been shown to affect the scattering behavior of platelet based metallic paint systems [28], and the measured effect predominantly changed the forward scattering intensity. As *PVC* or P_w was increased while other variables were held constant, the gap factor increased. A more definitive correlation between gap factor and scattering behavior would allow color designers to specifically adjust the gap factor of the paint system to achieve a specific gonioapparent behavior. The effect of changes in gap factor on scattering and transmission behavior will be discussed below.

Gap factor vs. lightness at 15° off-specular

A plot of lightness at 15° OS (45° illumination angle) as a function of gap factor for changes to both platelet size and *PVC* is shown in **Figure IV-7**. Also shown in this plot is a quasi-gapless system that was simulated by limiting the standard 15 μm platelet formulation and microstructure to a single reflection event. This single reflection event simulated what would occur if no gaps existed in the system. Lightness of this gapless system was calculated by reducing the number of rays scattered from the diffuse white standard to that of the simulated gapless system and inputting both quantities into *Equation (1)*.

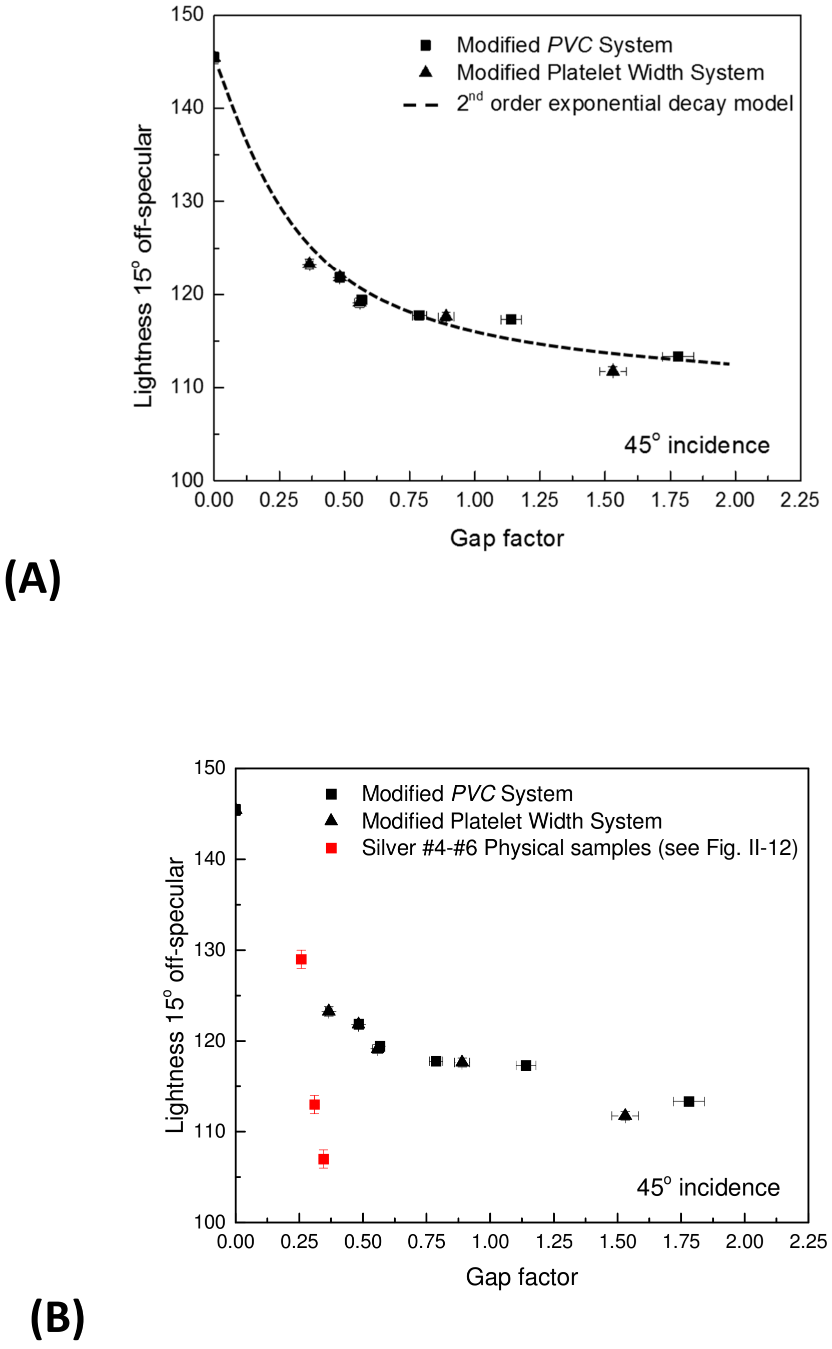

Figure IV-7: (A) Plot of gap factor vs. lightness at 15° OS for microstructures created by varying *PVC* and P_w. The gap factor's effect on lightness appears to be independent of the specific formulation change used to alter the gap factor. The lightness also appears to exponentially decay in relation to the gap factor. A 2nd order exponential decay model is also illustrated on the plot. **(B)** Plot of data shown in part (A) with gap factor/lightness data added from **Figure II-12** as a comparison. Decay rate of lightness at 15° OS relative to gap factor is larger than what was observed in simulated systems.

The data for the two systems shown in **Figure IV-7A** illustrates a few key relationships between gap factor and lightness at 15^{o} OS. First, it is evident that a specific gap factor will produce a corresponding lightness, *independent* of the particular formulation details. This lightness can be predicted by a 2nd order exponential decay model that is illustrated in **Figure IV-7**. The fitting parameters that correspond to this model are shown in **Table IV-6**.

We hypothesize that the exponential decay associated with the first term is a result of the two types of gaps that occur within the microstructure. The second exponential term is likely a lower lightness limit dependent on the orientation, platelet BRDF, and overall percent transmission of the platelet layer. Lateral gaps, or gaps along the surface of the platelet layer, are the primary way for light to enter the platelet structure and undergo multiple reflections. Assuming the platelet layer is formulated for minimal transmission, a change in the size or number of these gaps directly affects the lightness and results in an initial, rapid decay in lightness. Gaps that occur between platelets in the z-direction affect lightness as well, but can be shadowed by platelets closer to the surface, reducing their impact on lightness. This shadowing limits their ability to allow light to enter the platelet structure and undergo multiple reflections. This explains the reduction in the lightness decay rate as the gap factor reaches larger values. Due to the large number of platelets and different platelet configurations, it is impossible to use these results to correlate specific changes in lightness to specific gap types. However, future *in silico* studies will be conducted to isolate how specific gap types (lateral or z-direction) affect the gap factor-lightness decay rate.

It should be noted that the exact parameters and maximum lightness would change if the orientation distribution of the system changed. Further work is needed to determine how significant of a change would occur, but it indicates that the decay model cannot be universally used with all silver paint systems.

A comparison of the relationship between gap factor and lightness at 15^o OS under 45^o illumination for both the simulated model systems and for the physical samples of Silver #4-Silver #6 is shown in **Figure IV-7B**. While the relationship between gap factor and lightness at 15^o OS is apparent in both cases, it is clear that for the physical samples, the lightness decays more rapidly as a function of gap factor than in the simplified systems modeled in the hybrid environment. If it is assumed a physical zero-gap sample has a lightness of 145, equal to that of the simulated zero-gap sample, the lightness of the physical sample decays by approximately 40 points once a gap factor of 0.35 is reached. The hybrid simulation predicted a lightness reduction of approximately 23 points over the same gap factor range. This increased amount of decay in the physical samples indicates additional scattering and/or attenuation may occur within the physical sample that is not taken into account by the hybrid model.

One possible cause of the difference in the amount of lightness decay observed between the hybrid model and physical sample is the accuracy of the absorption value used for each ray's reflection from the aluminum platelets. This value, ~8% absorption, was reported for an ideal case of vapor deposited aluminum [13]. The aluminum platelets are processed differently and likely rougher than the vapor deposited aluminum, which may lead to an increase in absorption over the ideal case. It has been shown that roughness and structure do affect the reflectivity of metals [14,15]. This absorption is important to the gap factor/lightness relationship because gaps directly lead to multiple reflection events, and every reflection reduces the intensity of the rays that exit the system. However, changes in the absorption coefficient also affect the amount of light reflected during primary reflection events from platelet faces. When we tested this by increasing the absorption coefficient for the platelets within our hybrid model, the lightness decreased at all angles of observation, and did not improve the match between the lightness decay rate observed in the hybrid model and the physical samples. While absorption may contribute to the difference, it is not the primary cause for the decay rate variation.

A second possible cause of the difference in lightness decay rates observed between the hybrid model and physical sample is the fact that the hybrid model ignores the scattering of waves from edges and corners of the platelets. As was shown in Chapter II, the thickness of the platelets is approximately equal to the wavelength of light (500-600 nm). These edges, along with the small radii corners of the platelets, could cause additional light scattering as the light propagates through the platelet microstructure. This additional scattering would occur in the physical samples, but is unaccounted for in the hybrid model. The scattering would also be enhanced by an increase in gap factor, as more light enters the platelet microstructure and interacts with these edges and corners, but would have limited effect on a zero-gap sample or the primary reflections from platelet faces. Without the incorporation of this wave scattering into the hybrid simulation, any mathematical model would need a term added to increase the decay rate of the 2nd order exponential to account for this additional attenuation and scattering, something that will be examined in future work.

Table IV-6: 2nd order exponential decay model fitting parameters for the relationship between gap factor and lightness at 15° OS. The rate of decay decreases with angle of incidence. Each model had a goodness of fit >0.94.

2nd order exponential decay model: $y = ae^{bx} + ce^{dx}$					
Angle of Incidence	**a**	**b**	**c**	**d**	**R^2**
45°	23.43	-5.30	122.00	-0.05	0.99
30°	22.20	-4.29	116.00	-0.01	0.98
0°	11.83	-3.62	126.8	-0.01	0.94

The relationship between gap factor and lightness at 15° OS, as well as the gap factor's formulation independence held, when the angle of illumination was changed from 45° to 30° from normal. A schematic of this illumination and measurement condition is shown in **Figure IV-8A**, with the corresponding lightness shown in **Figure IV-8B**. Again, lightness at 15° OS followed a 2nd order exponential decay, but with a lower rate of lightness reduction. The parameters associated with the 30° decay model are listed in **Table IV-6**.

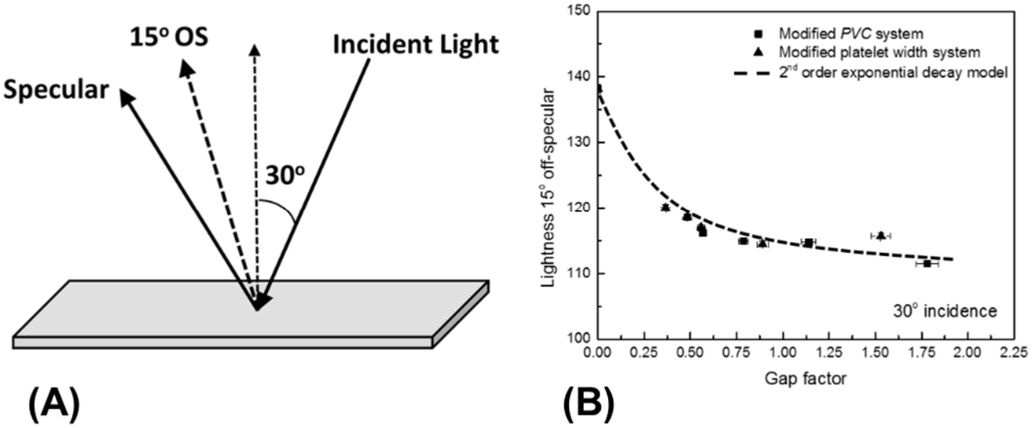

Figure IV-8: (A) Schematic of 30° illumination and 15° *OS* observation angle. (B) Plot of lightness at 15° OS as a function of gap factor. The relationship between gap factor and lightness again appears to be formulation independent. A 2nd order exponential decay in the data still exists.

When the angle of illumination was changed to 0° from normal, as shown in **Figure IV-9A**, the effect of gap factor on lightness at 15° OS was reduced further, as illustrated in **Figure IV-9B.** This was expected, as the gap factor should have minimal effect on lightness when the illumination enters the system directly normal to the surface. A small decay rate in the lightness data still exists due to the disorientation of the platelets, which can lead to light trapping and multiple reflection events. The 2nd order exponential decay model for this geometry is illustrated in **Figure IV-9**, with the fitting parameters shown in **Table IV-6.**

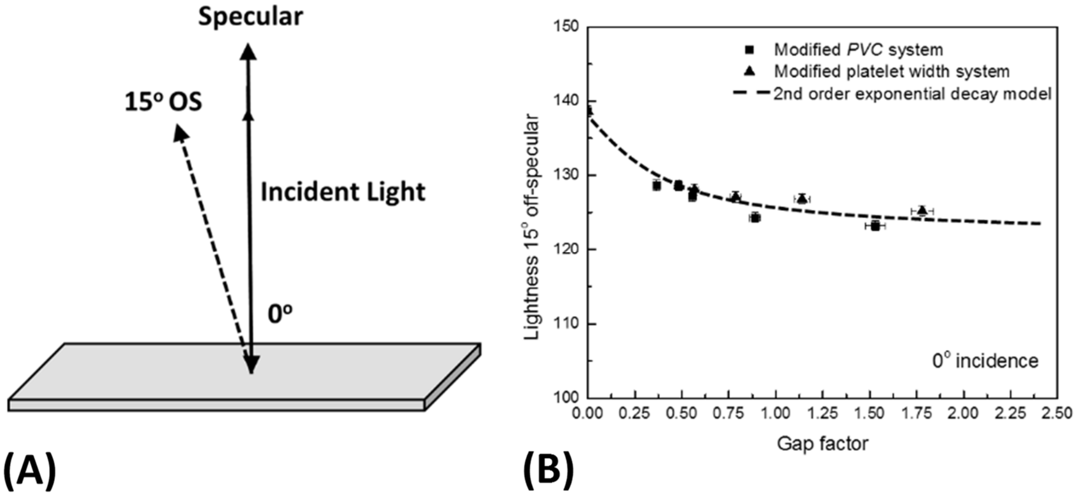

Figure IV-9: (A) Schematic of 0° illumination and 15° OS observation angle. (B) Plot of lightness at 15° OS as a function of gap factor. The relationship between gap factor and lightness again appears to be formulation independent. A 2nd order exponential decay still exists, but the initial slope of the decay model is significantly reduced compared to the 45° and 30° angle of incidence geometries.

Gap factor vs. fraction of original flux transmitted

The influence of the gap factor on the fraction of flux transmitted through the platelet layer is of interest to formulators and customers for the reasons previously outlined. To illustrate the relationship between these two quantities, the fraction of original flux transmitted as a function of gap factor for varying P_w is plotted in **Figure IV-10**. When the angle of incidence is reduced from 45° to 0°, the dependence of the transmitted flux on gap factor is reduced due to a lack of projected gap area exposed to the incoming light direction.

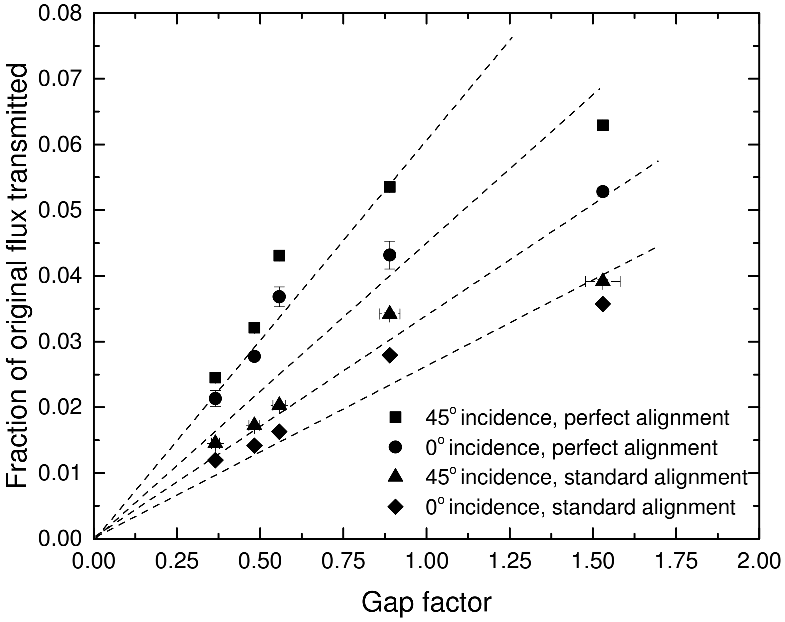

Figure IV-10: Percent original flux transmitted through the platelet layer as a function of gap factor. The introduction of gaps between the platelets increased the amount of light that penetrates through the 10 μm platelet layer. As was shown in **Figure IV-6**, the platelet alignment and incident angle of the light change the slope of the platelet size/flux transmission correlation. Clearly, light entering from 45° can more easily enter through the gaps between the platelets and progress through the platelet layer. However, the alignment of the layer also has an effect where a more perfectly aligned system also transmits more light. Dotted lines were added as a guide to the eye.

Light transmission is also significantly affected by the orientation of the platelets. The transmission through the perfectly oriented systems show a greater dependence on gap factor than the systems that exhibit some disorientation. When the platelets are disoriented, not only does the dependence on gap factor decrease, but so does the overall transmission percentage. One hypothesis for the increased transmission—and dependence on gap factor—by the perfectly oriented systems is that light trapping is enhanced when the platelets are perfectly aligned. The layers of platelets act as a wave guide and keep the light within the microstructure longer, increasing the opportunity of light to propagate through the platelet layer and transmit. The disorientation, however small, of the standard alignment system may reduce this wave guide trapping behavior. Further work is needed to identify the specific mechanism of this behavior.

Predictive modeling of unique microstructures

The results presented establish a foundation for the predictive modeling of lightness, travel (the difference between forward and backscattered lightness), and transmissive properties of silver metallic paint systems. The discovery that the dependence of lightness on gap factor is independent of the method used to modify gap factor is an important finding. This allows for the use of the 2nd order exponential decay model to predict how a system with a specific orientation will appear in the 15° OS direction. It is still important to note that the decay model can and likely will change if orientation or platelet surface roughness changes significantly.

A designer or formulator can use this predictive model to target specific lightness values for different regions of the scatter region. To reduce lightness in the backscatter region, edge area should be kept to a minimum. Gap factor affects the intensity in the forward scatter direction and should be minimized to achieve maximum lightness in the forward scatter direction. The minimization of gap factor also limits the amount of light transmitted through the platelet layer, allowing one to hide any sublayers at thinner film builds.

Interestingly, systems that utilize physical vapor deposition (PVD) platelets exhibit many of these desired microstructural characteristics. PVD platelets are very thin—30-50 nm—which significantly reduces edge area of the system. The platelets form a well oriented and closely packed structure, which minimizes the gap factor of the system. These properties reduce the platelet layer thickness needed to achieve hiding, and result in an increased lightness travel compared to traditional silver metallic systems [11].

Conclusion

The interaction of light with materials is of great interest to material, product, and color designers for a variety of reasons. Color and appearance can provide product differentiation, which is vital in a crowded and competitive marketplace. The empirical understanding and simplistic models that exist today do not allow designers to create new, unique, and most importantly, accurate renditions of hypothetical color systems. This work has identified key relationships between specific microstructural properties and their effect on scattering and lightness in idealized system. These relationships provide designers and formulators a roadmap on how to modify the platelet microstructure to achieve a specific look or appearance. While the relationships described cannot be used universally, they do provide a workflow for designers to use to conduct some of their research and development in the digital space.

The effect of platelet gaps on the scattering, propagation, and transmission behavior of light has been established through simulation. Results from our previous work on physical samples indicated platelet gaps reduce the lightness at near specular angles (15° and 25°). The results from the simulations conducted confirm this relationship. The gap factor vs. lightness at 15° OS relationship was determined for samples illuminated at 0°, 30°, and 45°. An increase in gap factor resulted in a decrease in the lightness at 15° OS. The lightness reduction was not as large as the one observed in the physical samples analyzed in Chapter II (see **Figure IV-7B** for the comparison). We hypothesize the additional lightness decay observed in the physical samples is due to wave scattering by the edges and sharp corners of the platelets within the bulk microstructure, which is not accounted for in the hybrid simulation. This additional effect must be incorporated into either directly into the simulation or as an adjustment factor into the mathematical model. Future work will dictate which modification is most feasible.

The effect of gap factor on the lightness at 15° OS was also shown to decrease as the angle of illumination approached the surface normal. These gaps were also shown to allow light into the platelet microstructure and increase the amount of light transmitted through the platelet layer.

Additional simulations were run to determine how the relationship between gap factor and lightness changes if the platelet's BRDF is made to be purely specular. It has been thought that this change in BRDF would produce the "ultimate" silver paint system with a very large lightness at 15° OS. This was shown to in fact be the case, where simulated lightness reached values >160. However, it also showed that the dependence of lightness on gap factor also increased significantly, where small changes in gap factor resulted in significant and perceivable changes in lightness. This indicates systems that utilize highly specular reflectors may be difficult to spray and manufacture consistently, as any change in processing could result in a microstructural/gap factor change. These changes would cause perceivable lightness shifts across a product, which may be visually unappealing to customers. A slight broadening of the BRDF appears to reduce the susceptibility of a paint system to this type of defect.

Edge area was shown to significantly affect the lightness in the backscattered region. An increase in edge area resulted in an increase in lightness at the 75^o and 110^o OS observation directions. The edges appeared to have minimal effect on the forward scattering behavior of the system.

A microfacet surface or single reflection model is not sufficient to predict the scattering behavior of these systems. The omission of edge and gap effects would likely result in the inaccurate prediction of scattering behavior for these platelet systems. While certain assumptions and compromises have been made, this model represents a significant step forward in the effort to accurately formulate, model, and visualize a metallic paint system without the need of physical prototyping. Some of the more significant compromises, such as the limitation of platelet scattering to purely specular events and the effect of edges and P_t of wave optics must be addressed in future works. However, this work is the first step in the creation of a model that can predict a system's BRDF utilizing all the microstructural properties of the paint system. The calculated BRDF could then be incorporated into a visualization package to render and display the digitally designed microstructure.

References

1. McCamy C (1996) Observation and measurement of the appearance of metallic materials. Part I. Macro appearance. Color Research & Application 21:292-304.
2. Kirchner E, van den Kieboom GJ, Njo L, Super R, Gottenbos R (2007). Observation of visual texture of metallic and pearlescent materials. Color Research & Application 32:256-266.
3. Klein GA, Meyrath T (2010) Industrial color physics. Springer, New York.
4. Maile FJ, Pfaff G, Reynders P (2005) Effect pigments—past, present and future. Progress in Organic Coatings 54:150-163.
5. Pfaff, G. (2001) Special Effect Pigments. High Performance Pigments (ed H. M. Smith), Wiley-VCH Verlag GmbH & Co. KGaA, Weinheim, FRG.
6. Seubert C, Nichols M, Frey J, Shtein M, and Thouless M (2016) The characterization and effects of microstructure on the appearance of platelet–polymer composite coatings. Journal of Materials Science, 51.5:2259-2273.
7. Pauli H (1976) Proposed extension of the CIE recommendation on “Uniform color spaces, color difference equations, and metric color terms”. JOSA 66:866-867.
8. Wright WD (1929) A re-determination of the trichromatic coefficients of the spectral colours. Transactions of the Optical Society 30:141-164.
9. Guild J (1932) The colorimetric properties of the spectrum. Philosophical Transactions of the Royal Society of London. Series A, Containing Papers of a Mathematical or Physical Character 1:149-187.
10. Hecht E (2002) Optics. Addison-Wesley, Reading.
11. Hezel F, Löw N, Schwarte S (2011) A paint that looks like metal. JOT-International Surface Technology 4:30-33.
12. Gunde MK, Kunaver M, Mozetic M, Pelicon P, Simcic J, Budnar M, and Bele M. (2002) Microstructure analysis of metal-effect coatings. Surface Coatings International Part B: Coatings Transactions 85, 2:115-121.
13. Hass G and Waylonis JE (1961) Optical constants and reflectance and transmittance of evaporated aluminum in the visible and ultraviolet. JOSA 51(7):719-722.
14. Sennett RS and Scott GD (1950) The structure of evaporated metal films and their optical properties. JOSA, 40(4):203-211.
15. Maradudin AA and Mills DL (1975) Scattering and absorption of electromagnetic radiation by a semi-infinite medium in the presence of surface roughness. Physical Review B, 11(4):1392.

CHAPTER V

Summary and Conclusion

Summary

Color and appearance are material properties that customers consider during the observation, evaluation, and ultimately, the purchase of an item or product. The goal of the work presented in this thesis was to obtain a more thorough understanding of the structure-property relationship between the microstructure of a layered platelet containing silver metallic paint and the angularly dependent lightness produced under illumination. The lack of an accurate, predictive computer model to conduct structure-property experiments in the digital space motivated us to create a hybrid wave-ray based model that utilized the complete 3D platelet microstructure, as well as the platelet's surface roughness. This model was then used to conduct some of the aforementioned digital studies that could not be performed in the physical space. A summarization of the relevant results found during the development and use of the hybrid model are listed below.

Chapter II detailed our efforts to measure the microstructure of silver metallic paint systems that utilized different formulation and processing conditions. We confirmed the platelet orientation of the system significantly affects the scattering behavior of the silver metallic paint system, where lightness at 15^o OS ranged between 129 and 143 for identical formulations applied differently. However, we also found and quantified for the first time that another microstructural property, gap factor, significantly affects the near-specular scattering behavior of the paint system, where a 0.09 point reduction in gap factor resulted in a 22 point increase in lightness at 15^o OS. The gap factor parameter is dependent on the platelets not only at the very surface of the platelet layer, but also those contained below the surface. To model the effect of gap factor on the scattering behavior of the system, a more complete, 3D model of the system was needed than what currently exists in the literature today [1–5].

Chapter III detailed our efforts to create a new model that relies not only on the entire 3D microstructure of the paint system, but also incorporates the nano-scale surface roughness (~50 nm) of the platelet surfaces. To simulate the 3D microstructure of the silver paint system, a platelet array was generated *in silico* using platelet width, thickness, *PVC*, and orientation data obtained from physical samples. Surface roughness of platelets extracted from wet paint was, for the first time, measured using optical profilometry. These roughness profiles were imported into a FEA simulation environment to quantify the BRDF of light reflected from the platelet face. This is likely the first time the BRDF of single platelets has been quantified, as physical reflection measurements of individual platelets is not possible at this time due to size limitations.

The final hybrid ray-wave model created in Chapter III matched the lightness behavior of physical samples at most angles of observation. Using the new model, the effect of surface roughness on the lightness behavior of a layered platelet system was examined. The σ_{RMS} was found to have the greatest impact on the shape of the BRDF and the resulting lightness of the system. Once σ_{RMS} increased to ~200 nm, the lightness at 15^o OS dropped significantly, as did the flop index. The presented data provides a foundation for the creation of a mathematical model that paint and color designers can use to tailor the lightness behavior of a silver metallic paint based on the roughness of the platelets used. We also used this new hybrid simulation tool to identify and quantify additional structure-property relationships within the silver metallic paint systems. The model was used to carry out these studies *in silico* due to the multiple microstructural changes that occur during application of different paint formulations.

Chapter IV detailed our work utilizing our hybrid simulation model to quantify the structure-property relationships between lightness and specific platelet formulation conditions such as platelet width, thickness, and *PVC*. The model allowed us to change single microstructural factors while all other aspects of the microstructure remained the same. The most significant finding of this work was that not only did we confirm gap factor significantly affects the lightness at 15^o, 25^o, and 45^o OS, but that the lightness-gap factor correlation is independent of the specific formulation change that occurs (platelet width, *PVC*, etc.). As a result, we were able to generate a 2nd order exponential decay model for the relationship between lightness at 15^o OS and gap factor for three different angles of illumination. The decay rate of this model was less than what was observed in the physical samples analyzed in Chapter II. We hypothesize that the additional scattering/attenuation of the light occurs due to platelet corners and edges within the bulk microstructure.

While this decay model cannot be used universally and has certain limitations, it is possible to generate a mathematical guidance model for formulators and designers to use for specific paint formulations where one could target a specific lightness and calculate gap factor value needed to achieve the desired look.

Path Forward

In this work, we incorporated both wave and ray based optics into a complete 3D multi-bodied scattering model. We used this model to look at only one instance of how a multi-bodied structure such as a platelet containing paint system scatters incoming radiation, in this case, visible light. Initial development of this model focused on scattering particles with relatively simple BRDFs and microstructures. This simplicity, however, is not required and now that the basic development and understanding has been established, the model can be used to explore more complex systems.

One potential application that involves complex systems for use in cosmetic applications is through the use of new manufacturing techniques to generate unique paint/coating microstructures. One specific manufacturing technique that is gaining interest in both research and industrial applications is additive manufacturing, also known as 3D printing. 3D printing applications span across a range of industries, including medical [6], energy storage [7], aerospace and automotive [8]. It is conceivable that in the near future, this manufacturing technique will allow designers and color scientists to develop detailed and specific microstructures that incorporate resins, pigments, and platelets alike, and print those structures onto a manufactured product. It may even be used to generate biomimetic structures, such as those used by animals for camouflage [9,10], or structural photonic colors, such as those seen in morpho butterflies [11,12,13,14,15]. However, the designer or researcher still needs to understand, be it visually or through numerical data, how the designed microstructure will scatter light and appear once it is on the product. Our hybrid model could be implemented within the 3D printing software to provide real-time color data to the user. The model could even be combined with a graphical rendering engine to display not only the colorimetric data, but also realistic, color accurate renderings for the user to interact with and modify as needed. Below, we will describe some potential systems that could be designed and printed using additive manufacturing and report on the lightness results obtained from simulations of the designed microstructures.

Tailored Microstructures of Aluminum Platelets

Microcups

While the color industry waits for new pigment technologies to be brought to market, there still exists a need to generate new and interesting color and appearance effects. Instead of changing the microstructure of the pigments themselves, new additive manufacturing techniques could be used to create specific orientations or microstructures. For example, standard aluminum platelets could be oriented at specific normal and azimuthal angles to either enhance the lightness travel of silver metallic colors or generate new effects not previously seen from aluminum platelet containing colors.

Here we've used our previously discussed hybrid simulation method to examine two unique microstructures and predict their appearance when exposed to both directional and diffuse lighting. The first microstructure consists of a series of faceted microcups arranged on a single layer lattice, suspended in a standard acrylic clearcoat. The microcup inclination angle, θ_{MC}, of these cups was varied to produce different lightness effects from different light sources and identify which, if any, inclination angle creates a look of interest in a particular illumination environment. A schematic of one of the microcups is shown in **Figure V-1**. Each cup has 10 facets that measure 7.5 μm in length. The facet surface was assigned either a specular BRDF or a roughened BRDF equivalent to that measured in Chapter IV for the extracted platelets. The angle of the facets can be varied between 0^o and 90^o. Here, θ_{MC} was varied at 15^o intervals between 15^o and 60^o. The cups were arranged in a single layer and placed on lattice points 17.5 μm apart in both the x- and y-directions. Each layer was illuminated with both collimated light (0^o or 45^o from normal) and diffuse light to determine if the scattering behavior varied due to illumination conditions. The results from these trials are presented below.

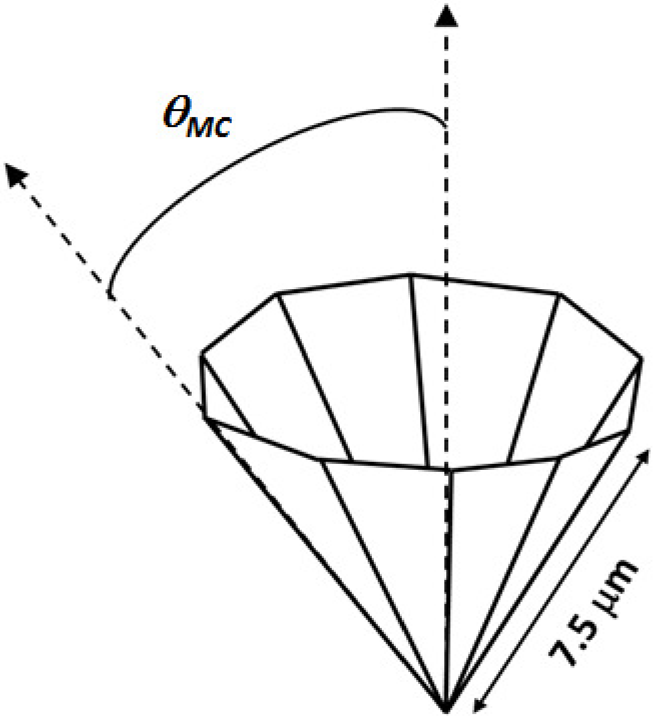

Figure V-1: Schematic of a single faceted microcup created and placed across a single layered lattice microstructure. The length of each facet is 7.5 μm in length and the angle of the facets is described as θ_{MC}. θ_{MC} was evaluated at 15, 30, 45, and 60 degrees.

Under diffuse illumination, the scattering behavior of most of the microcup structures resulted in relatively uniform lightness (~70-90) across the scattering hemisphere—see **Figure V-2** for an example scattering pattern. The only directionally unique scattering behavior occurred in the 60° microcups where a lightness minimum occurred in the center of the scatter pattern out to ~45° from normal. These results are shown in **Figure V-3A&B**. The lightness dropped to ~40-50 from ~70-90, which is significant and perceivable to a human viewer. While the minimum occurred in both surface BRDF conditions, the reduction in lightness was greater in the system that utilized the specular surface BRDF. This lightness minimum is likely due to light trapping effects brought on by the shape of the microcup and differs from what is typically observed in standard silver metallic paints. Silver metallic under diffuse illumination exhibit a relatively uniform lightness of ~85-100 across the scattering hemisphere. These microcups could be one way for designers to generate lightness travel in lighting conditions that do not exhibit large amounts of directional light, such as a cloudy day or under indoor fluorescent lights.

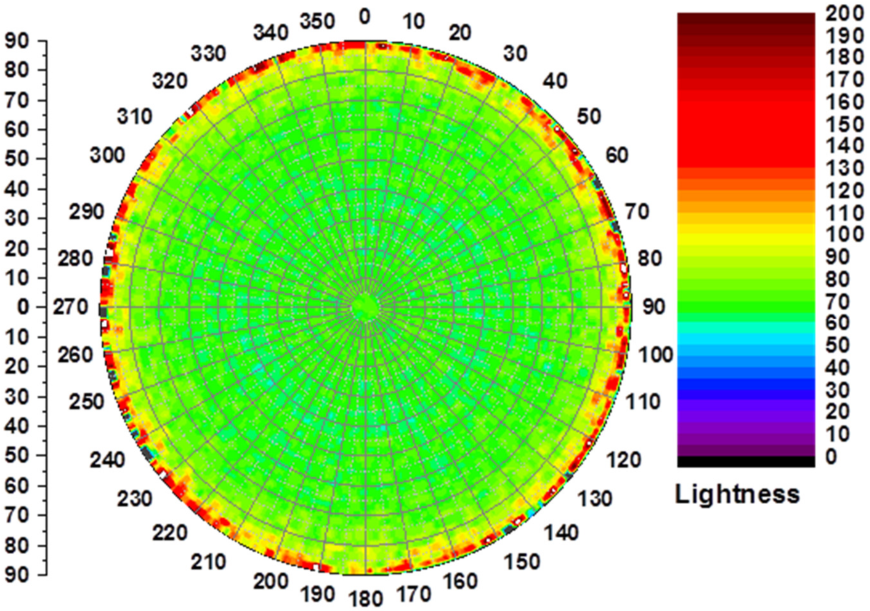

Figure V-2: Example lightness scatter pattern for the microcup structure with a θ_{MC} of 45° and a specular surface BRDF. A similar scatter pattern was observed at 30° and 15° θ_{MC} and in both the specular and roughened surface BRDF systems. Exposed to diffuse illumination.

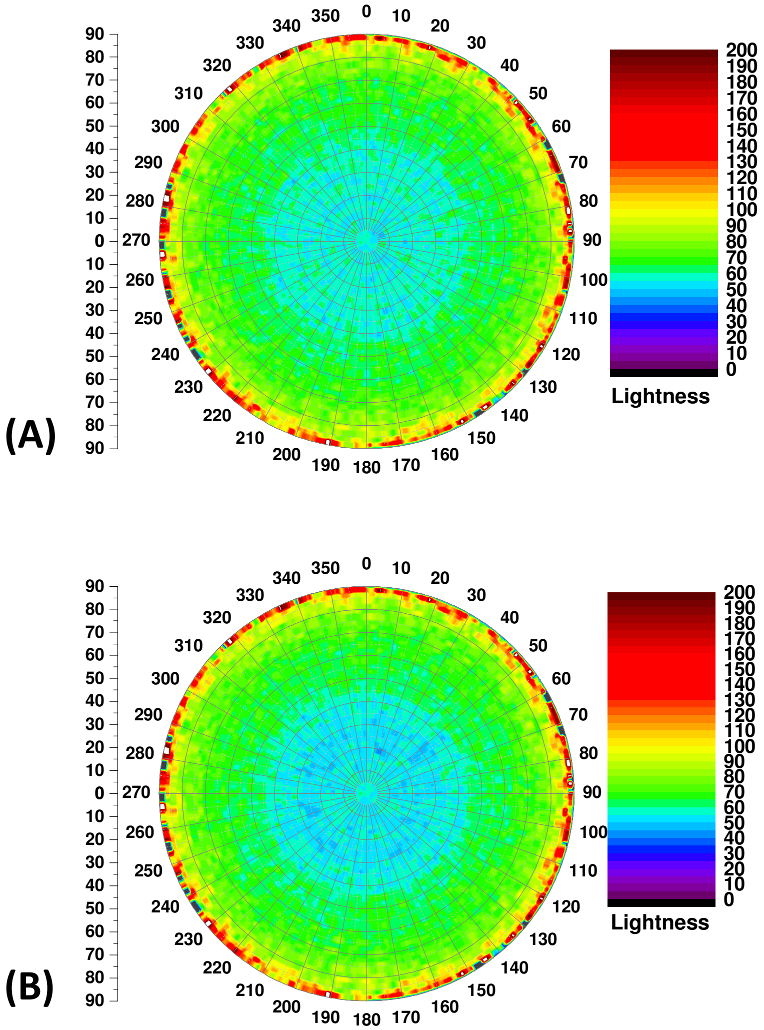

Figure V-3: Lightness scatter patterns of the 60° microcup under diffuse illumination. A roughened surface BRDF was used to create the results shown in (A), while a specular surface BRDF was used in (B). In both cases, a significant lightness minimum exists in the middle of the scatter pattern out to ~45°.

Under directional illumination, the scattering behavior of the microcup microstructure exhibited some additional behavior of interest. When the system was illuminated from the normal direction, the 15° microcup with a specular surface BRDF exhibited a focused, hyper-lightness zone (L^*>200) at ~47° (**Figure V-4**). The other θ_{MC} angles showed no such region and behaved similarly to that of a typical silver metallic paint system. Clearly, the combination of the specular surface, θ_{MC}=15°, and the IOR of the clearcoat resulted in this highly focused reflection ring. This microstructure could provide great visual interest in very specific illumination conditions if it could be controlled to the high degree shown in digital simulations.

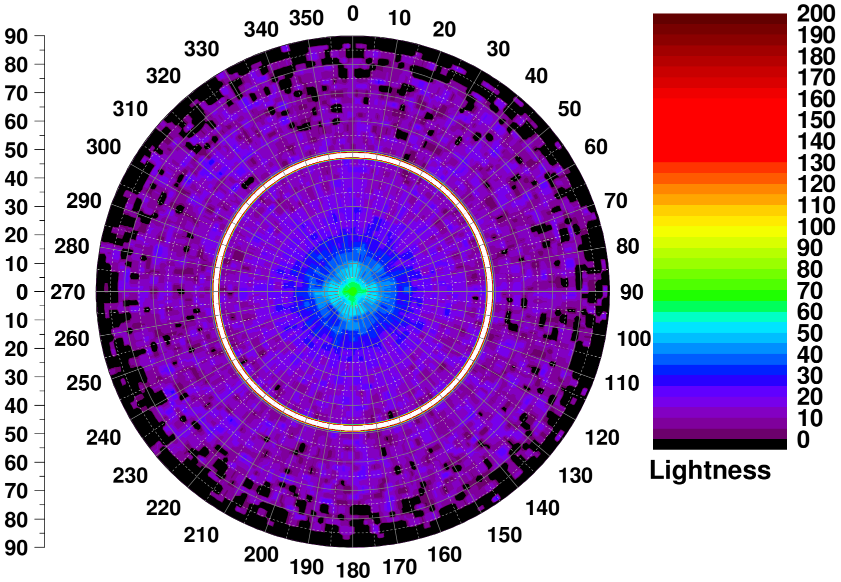

Figure V-4: Microcup microstructure with a θ_{MC} of 15° and a specular surface BRDF under directional illumination from the normal direction. A maximum lightness ring (200+) forms at ~47° from normal. Outside of this ring, the lightness is on the order of 10-20.

This highly focused reflection behavior was also observed when these same systems were illuminated at 45° from normal. Under this illumination condition, all four microcup angles exhibited regions of hyper-lightness (L^*>200), but at different locations on the scattering hemisphere. These scatter patterns are shown in **Figure V-5A-D** and are again likely the result of light trapping and focusing by the microcups. As θ_{MC} increased, the hyper-lightness zone seemed to move from the forward scatter region to the backscatter region, where a second, less intense hyper-lightness zone formed in its wake. In fact, there are numerous observation angles where a ~140 point drop in lightness could occur just by changing the observation angle by a few degrees. This indicates that these microcups could be designed to provide some very unique lightness behaviors just by changing the angle of the microcup a few degrees. Clearly, this level of orientation control is not possible today. However, the development of a highly

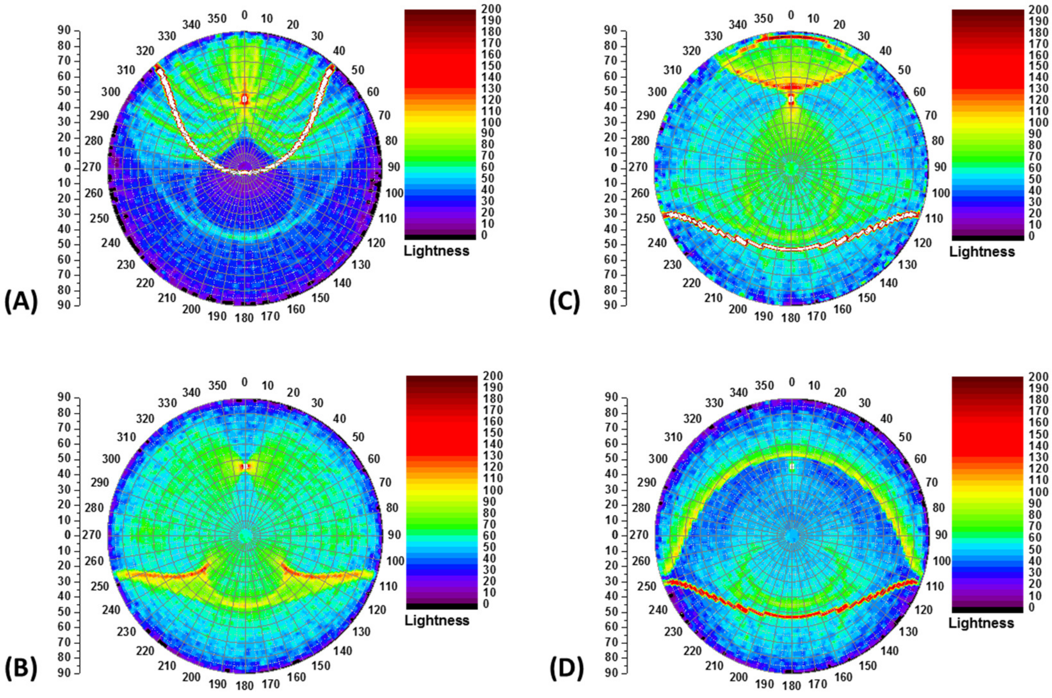

Figure V-5: Lightness scatter patterns of microcup microstructure with specular surface BRDF illuminated at 45°. θ_{MC} was set to (A) 15°, (B) 30°, (C) 45°, and (D) 60°. Each pattern exhibits a hyper-lightness zone, but the location of that zone varies due to the microstructure's geometry. The 15° microstructure exhibits the largest lightness difference between the hyper-lightness zone and the surrounding scatter pattern.

specular magnetic platelet may allow an operator to use a high powered magnet to preferentially orient the platelets and achieve some of these optical effects.

Fixed Linear Microstructure

While the microcups were a type of microstructure that created significant lightness variation under directional illumination, we created another microstructure that produced significant lightness variation under diffuse illumination. This microstructure, termed "fixed linear", is a layer of platelets arranged on a lattice with an orientation angle from normal, θ_{LINE}, and an azimuthal angle of zero. Each platelet center is separated by 10 μm in the x-direction and 15.1 μm in the y-direction. A schematic of this microstructure is shown in **Figure V-6A & B** respectively. The value of θ_{LINE} was set at the following angles to evaluate their effect on the scattering pattern of the system: 5°, 15°, 30°, 45°, 60°, and 75°. Diffuse and directional

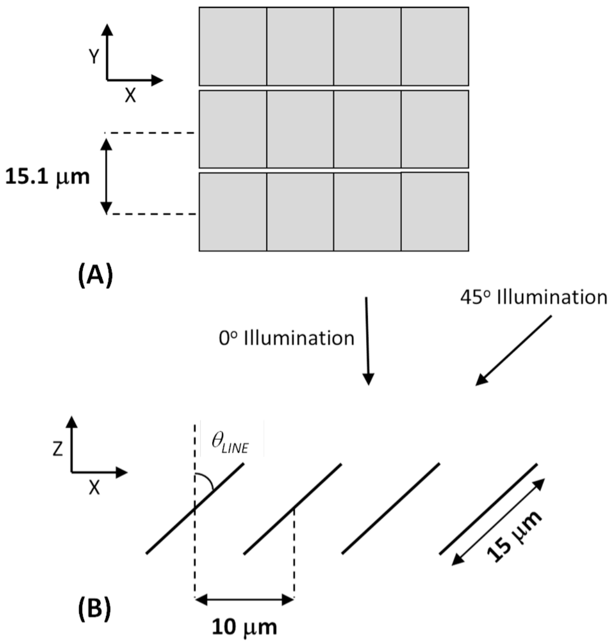

Figure V-6: Schematic of the fixed linear microstructure. Top down view is shown in (A), while a side view is shown in (B). All platelets are oriented with the same normal and azimuthal angle and placed on a single layer lattice 10 μm apart in the x-direction and 15.1 μm apart in the y-direction. θ_{LINE} represents the normal angle of the platelets.

illumination was examined, but only the diffuse illumination produced results of interest and will be discussed below.

The fixed linear microstructure with a roughened surface BRDF under diffuse illumination produced the scatter patterns shown in **Figure V-7A-F**. As θ_{LINE} was increased, a significant reduction in lightness occurred between the azimuthal angles of 90^o and 270^o—the lower portion of the scatter pattern. This reduced lightness zone grew in size until a lightness minimum, as shown in **Figure V-7F,** was formed. An increased lightness, however, still exists at the grazing observation angles. This is completely counter to what occurs in standard silver metallic paint systems under directional illumination. Again, this type of microstructure would create unique and interesting visual effects under otherwise diffuse illumination conditions.

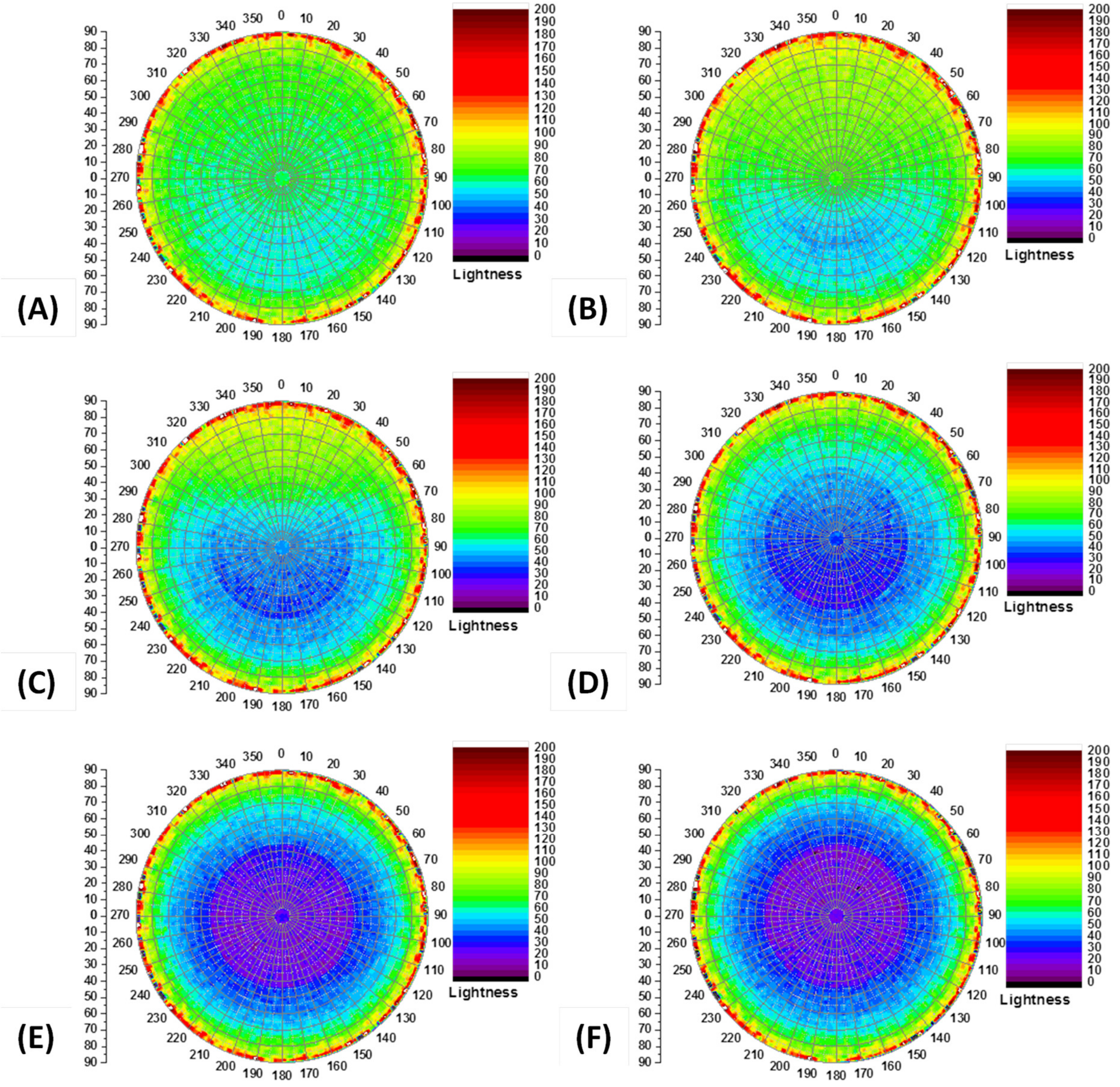

Figure V-7: Lightness scatter patterns for the fixed linear microstructure under diffuse illumination and with a rough surface BRDF. θ_{LINE} was fixed at (A) 5°, (B) 15 °, (C) 30 °, (D) 45 °, (E) 60 °, and (F) 75° from normal. A lightness minimum appears to enter the scatter pattern from the bottom and slowly encompass the entire pattern as θ_{LINE} is increased.

The unique lightness behavior was enhanced when the platelet surface BRDF was changed to specular. As illustrated in **Figure V-8A-F**, a lightness reduction began to slowly enter from the bottom of the scattering hemisphere as θ_{LINE} increased. At θ_{LINE}=45°, the scatter profile matched that of the 75° fixed linear microstructure with roughened surface BRDF. At 60° and 75°, however, a more dramatic scattering event occurred. A zero lightness zone developed at observation angles less than 45° from normal (**Figure V-8E-F**). The zone's shape differed between the two θ_{LINE} angles. It is clear that this fixed linear microstructure completely shadows parts of the scattering pattern and produces a near black appearance at specific viewing angles. All of this visual interest would occur in environments where it would be unexpected, under diffuse illumination. This microstructure could be used to differentiate a product, especially if that product is used in diffuse illumination conditions. In addition, if θ_{LINE} could be changed after product application, it could allow a designer, or even a consumer, to customize the appearance of the product and generate some very novel and unique appearances.

Both the microcup and fixed linear microstructures are two novel and unique microstructures that could be produced using additive manufacturing techniques. It remains to be seen when the speed and resolution of 3D printers will achieve the levels necessary to generate a coating or paint system that can cover a manufactured product in a robust, durable way. Our hybrid model can not only model the current, state-of-the-art capabilities of 3D printed microstructure, but can also be used to identify the required scale and resolution of proposed microstructures that cannot be produced in a physical medium.

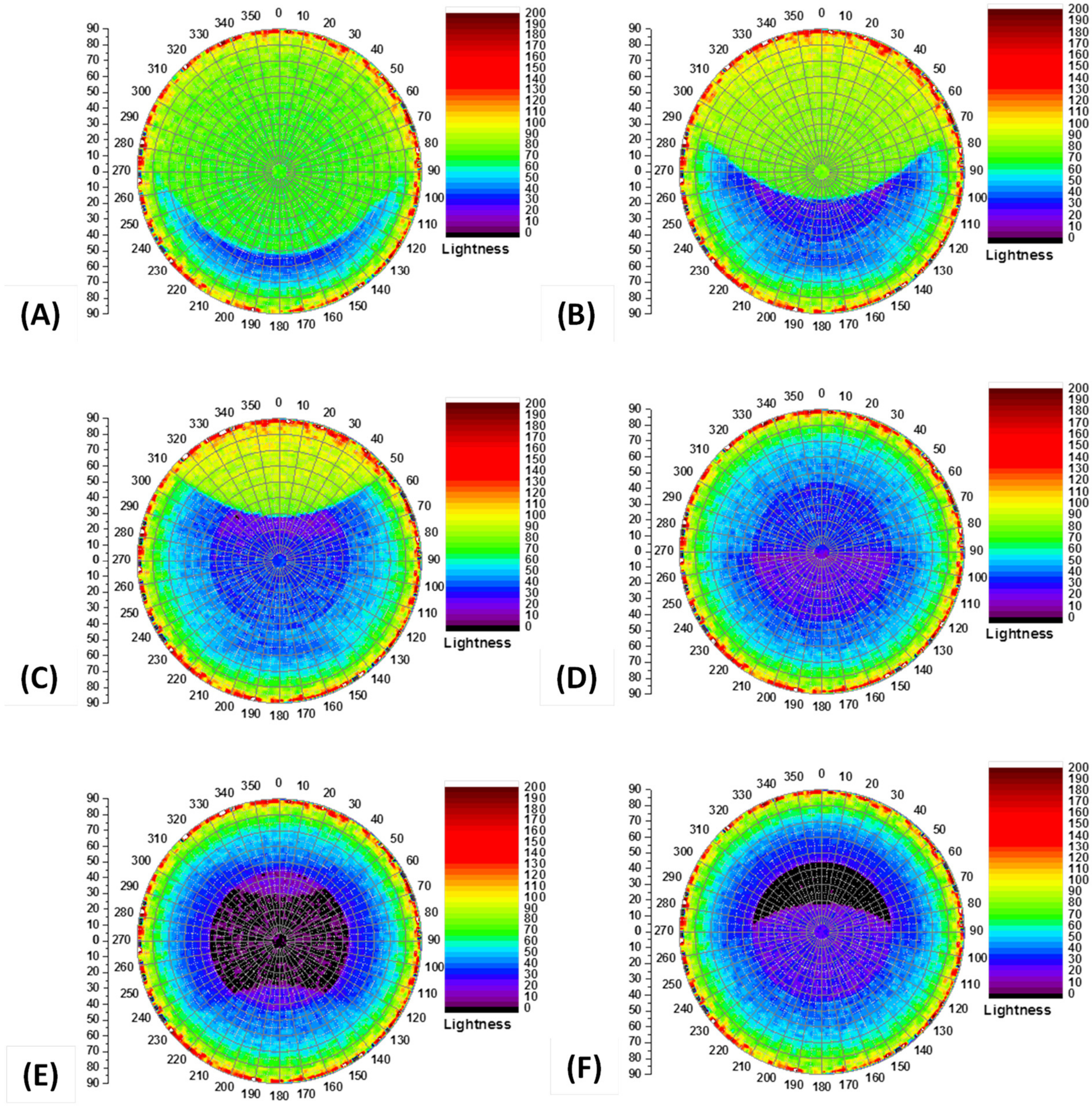

Figure V-8: Lightness scatter patterns for the fixed linear microstructure under diffuse illumination and with a specular surface BRDF. θ_{LINE} was fixed at (A) 5°, (B) 15°, (C) 30°, (D) 45°, (E) 60°, and (F) 75° from normal. A more pronounced lightness minimum appears to enter the scatter pattern from the bottom and slowly encompass the entire pattern as θ_{LINE} is increased. Also, at the 60° and 75° θ_{LINE} angles, the lightness minimum approached zero near the center of the scatter pattern.

Functional Coatings

Functional coatings are applied to surfaces not only to provide protection, but also to perform some other type of needed "function". Hydrophobic coatings are often used to prevent natural biofouling in maritime vehicles [16] and reduce icing on vehicles used in cold weather climates [17]. Self-clean coatings are also under development to either reduce or eliminate the need to physically clean a surface [18,19]. In general, these coatings are optically clear and have no visual effect on the cosmetic properties of the paint or substrate that they are applied over.

One specific area of transportation that would benefit from functional coatings are autonomous vehicles [20,21]. These vehicles rely on a variety of technologies to detect, communicate, evaluate, and execute a range of autonomous tasks. Paint that functions as the vehicles primary antenna and a coating that increases the radar visibility of the vehicle through IR reflectivity enhancement are two areas where functional coatings could benefit autonomous vehicles.

Inter-vehicle communication [22,23] relies on the use of different radiation frequencies to communicate between one or more other vehicles. At this time, antennas are mounted on the vehicle using different strategies to insure any outgoing or incoming signal can be sent or received. Work has even been conducted to identify if the exterior paint affects the performance of the embedded antenna [24]. In the future, a tailored microstructure could be generated to enable the exterior paint to function as the vehicle's primary antenna. A significant advantage of this "antenna paint" would be the 360° antenna surface available to the autonomous control system. It would also eliminate the need to package and locate physical antennas within the vehicle subsystems. Our hybrid scattering tool could be used to design and trial a paintable antenna microstructure within the digital space to determine how such microstructures absorb and scatter specific wavelengths of interest.

In addition to inter-vehicle communication, autonomous vehicles must also detect and identify objects within its immediate driving environment, regardless of the surrounding environmental conditions. Light based radar (LIDAR) utilizes IR laser light, at a wavelength of 905 nm or 1550 nm, to detect surrounding vehicles [25,26,27]. Unfortunately, most exterior paint colors and materials reflect less than 50-60% of the incident intensity at those two wavelengths, with some black colors only reflecting ~5%. This reflectivity is critical if we hope to achieve completely autonomous vehicles that can avoid collisions with other vehicles during operations.

The hybrid model presented here could be used to create a specific microstructure that is highly reflective at one or both of the 905/1550 nm wavelengths. It is already known that certain thin film stacks can be highly reflective at certain wavelengths while transparent at others [28,29,30]. Unfortunately, a full vehicle coated with a delicate, high cost thin film stack is likely not possible. However, if pigments or platelets that utilize these thin films could be created, our model could be used to evaluate microstructural arrangements of these pigments or platelets and quantify the bulk reflectivity of specific microstructures. The reflectivity and cost could be optimized through simulation, with a select group of systems produced as a physical prototype and tested in real world applications.

The method described throughout this thesis is the initial work in a larger effort to not only create a model to design and visualize a material's appearance based on the true physical interaction of light with the material and its constituents, but also expand our capabilities to model multi-bodied, three dimensional scattering structures. While this work only provides numerical results, we hope this method can be combined with a visualization package to allow designers and formulators to visualize and perceive appearance differences that result from microstructural changes to a material. To describe these colors accurately in the digital domain, models that incorporate all aspects of physics and the underlying structure of the scattering layer must be created. Such a model would allow researchers to quantify completely new appearance mechanisms based on biomimetics, photonic crystals, or carbon nanotubes. This tool could also be used to drive research into new manufacturing techniques to generate highly specialized microstructures, allowing researchers to identify and target truly unique and novel systems through digital design optimization. One day, it is possible that an entire product, from structure to components to color, will exist within a digital workspace and be built through additive manufacturing, quite possibly in the consumer's own home.

References

1. Ershov S, Kolchin K, Myszkowski K (2001) Rendering Pearlescent Appearance Based On Paint-Composition Modelling. EUROGRAPHICS 2001, 20:227-238.
2. Weidlich A, Wilkie A (2007) Arbitrarily layered micro-facet surfaces. Proceedings of the 5th international conference on Computer graphics and interactive techniques in Australia and Southeast Asia. ACM 1:171-178.
3. Seo MK, Kim KY, Kim DB, Lee KH (2011) Efficient representation of bidirectional reflectance distribution functions for metallic paints considering manufacturing parameters. Optical Engineering, 50:013603.
4. Ashikmin M, Premoze S, Shirley P (2000) A microfacet-based BRDF generator. Proceedings of the 27th annual conference on Computer graphics and interactive techniques. ACM Press/Addison-Wesley Publishing Co. 65-74.
5. Jakob W, Hasan M, Yan LQ, Lawrence J, Ramamoorth R, Marschner S (2014) Discrete stochastic microfacet models. ACM Transactions on Graphics (TOG), 33:115.
6. Rengier F, Mehndiratta A, von Tengg-Kobligk H, Zechmann CM, Unterhinninghofen R, Kauczor HU, and Giesel FL (2010) 3D printing based on imaging data: review of medical applications. International journal of computer assisted radiology and surgery, 5(4):335-341.
7. Sun K, Wei TS, Ahn BY, Seo JY, Dillon SJ, and Lewis JA (2013) 3D Printing of Interdigitated Li-Ion Microbattery Architectures. Advanced Materials, 25(33):4539-4543.
8. Gibson I, Rosen D, and Stucker B. (2014). Additive manufacturing technologies: 3D printing, rapid prototyping, and direct digital manufacturing. Springer, New York.
9. Hanlon R (2007) Cephalopod dynamic camouflage. Current Biology 17.11: R400-R404.
10. Barbosa A, Litman L, and Hanlon RT (2008) Changeable cuttlefish camouflage is influenced by horizontal and vertical aspects of the visual background. Journal of Comparative Physiology A 194.4:405-413.
11. Srinivasarao M. (1999) Nano-optics in the biological world: beetles, butterflies, birds, and moths. Chemical reviews 99(7):1935-1962.
12. Kinoshita S, Yoshioka S, and Miyazaki J. (2008) Physics of structural colors. Reports on Progress in Physics. 71(7):076401.
13. Kinoshita S and Yoshioka S. (2005) Structural colors in nature: the role of regularity and irregularity in the structure. ChemPhysChem. 6(8):1442-1459.
14. Tayeb G, Gralak B, and Enoch S. (2003) Structural colors in nature and butterfly-wing modeling. Optics and photonics news. 14(2):38-43.
15. Kinoshita S, Yoshioka S, and Kawagoe K. (2002) Mechanisms of structural colour in the Morpho butterfly: cooperation of regularity and irregularity in an iridescent scale. Proceedings of the Royal Society of London B: Biological Sciences. 269:1417-1421.
16. Atlar M and Callow M (2003) The development of foul-release coatings for seagoing vessels. Journal of Marine Design and Operations B, 4:11.
17. Cao L, Jones AK, Sikka VK, Wu J, and Gao D (2009) Anti-icing superhydrophobic coatings. Langmuir, 25(21):12444-12448.

18. Parkin IP and Palgrave RG (2005) Self-cleaning coatings. Journal of Materials Chemistry, 15(17):1689-1695.
19. Gould P (2003) Smart, clean surfaces. Materials Today, 6(11):44-48.
20. Falcone P, Borrelli F, Asgari J, Tseng HE, and Hrovat, D (2007) Predictive active steering control for autonomous vehicle systems. Control Systems Technology, IEEE Transactions on, 15(3):566-580.
21. Beard RW, Kingston D, Quigley M, Snyder D, Christiansen R, Johnson W, McLain T, and Goodrich M (2005) Autonomous vehicle technologies for small fixed-wing UAVs. Journal of Aerospace Computing, Information, and Communication 2, 1:92-108.
22. Luo J and Hubaux JP (2004) A survey of inter-vehicle communication (No. LCA-REPORT-2000-009).
23. Jawhar I, Mohamed N, and Zhang L (2010) Inter-vehicular communication systems, protocols and middleware. In Networking, Architecture and Storage (NAS), 2010 IEEE Fifth International Conference on (pp. 282-287). IEEE.
24. Pell B, Rowe W, Sulic E, Ghorbani K, John S, Gupta R, Zhang K, and Hughes B (2008) Experimental study of the effect of paint on embedded automotive antennas. In Vehicular Technology Conference, 2008. IEEE, pp. 3057-3061. IEEE.
25. Gao B and Coifman B (2006) Vehicle identification and GPS error detection from a LIDAR equipped probe vehicle. In Intelligent Transportation Systems Conference, 2006. ITSC'06. IEEE (pp. 1537-1542). IEEE.
26. Rasshofer RH and Gresser K (2005) Automotive radar and lidar systems for next generation driver assistance functions. Advances in Radio Science, 3(B.4):205-209.
27. Najmi A, Mahrane A, Estève D, Vialaret G, and Simonne JJ (1995) Pulsed LIDAR for obstacle detection in the automotive field: the measurement of reflectance range data in scene analysis. Sensors and Actuators A: physical, 47(1):497-500.
28. Baumeister P (2004) Optical coating technology (Vol. 137). Bellingham: SPIE Press, Bellingham.
29. Macleod HA (2001) Thin-film optical filters. CRC press, London.
30. Rancourt, JD (1996) Optical thin films: user handbook. SPIE Press, Bellingham.